Second-moment closure modeling of turbulent bubbly flows within the two-fluid model framework

Vom Fachbereich Maschinenbau
an der Technischen Universität Darmstadt
zur
Erlangung des Grades eines Doktor-Ingenieurs (Dr.-Ing.)
genehmigte

D i s s e r t a t i o n

vorgelegt von

Matthias Ullrich, M.Sc.

aus Frankfurt am Main

Berichterstatter:	Prof. Dr.-Ing. C. Tropea
Mitberichterstatter:	Apl. Prof. Dr.-Ing. S. Jakirlić
	Prof. Dr.-Ing. J. Janicka
Tag der Einreichung:	02.08.2016
Tag der mündlichen Prüfung:	15.11.2016

Darmstadt 2017
D17 (Diss. Darmstadt)

Hiermit versichere ich, die vorliegende Doktorarbeit unter der Betreuung von Prof. Dr.-Ing. C. Tropea und Apl. Prof. Dr.-Ing. S. Jakirlić nur mit den angegebenen Hilfsmitteln selbständig angefertigt zu haben.

Darmstadt, den 2. August 2016

Abstract

The present study is focused on the simulation of turbulent bubbly flows by utilizing the two-fluid model (TFM) in conjunction with advanced near-wall Reynolds-stress models (RSMs) within the Reynolds-averaged Navier-Stokes (RANS) framework. Such anisotropy-resolving turbulence models, employed in combination with the TFM, have been rarely used for two-phase flow computations. The presently adopted RSMs are based on the formulations initially proposed by Jakirlić and co-workers ([46], [47], [6], [70] and [71]) for incompressible single-phase flows. Two essentially different RSM versions are selected to be applied in the present work. One model version is formulated within the conventional RANS framework, whereas the second one resembles an instability-sensitized RSM variant, capable of adequately resolving the fluctuating turbulent motions in accordance with the scale-adaptive simulation (SAS) proposal by Menter and Egorov [76].

The necessary modifications of both Reynolds-stress models to be used within the TFM computational framework, also in conjunction with different model formulations accounting for the bubble-induced turbulence, require an appropriate coupling algorithm, which, independent of the geometrical complexity of the flow configurations considered, represents by itself a challenging task. The three reference flow configurations, chosen for the model validation, are the turbulent bubbly flows in a straight and suddenly-expanded vertical pipe over a range of Reynolds numbers and a square cross-sectioned bubble column. In addition, due to sake of comparative evaluation, the available corresponding single-phase flows are investigated by using both RSMs.

The presently realized numerical investigations demonstrate successful employment of both Reynolds-stress models for bubbly flow computations. In all three flow configurations the results obtained with the conventional RSM exhibit a high level of qualitative and quantitative agreement with the available reference data. The novel scale-resolving RSM reveals its high potential, representing a promising approach for further investigations.

Kurzfassung

Die vorliegende Arbeit beschäftigt sich mit der numerischen Simulation turbulenter Blasenströmungen im Rahmen der Euler-Euler Methode mittels eines wandauflösenden Reynolds-Spannungsmodells (RSMs), das auf dem Konzept der Reynolds-gemittelten Navier-Stokes Gleichung basiert. Solche, die Anisotropie der turbulenten Spannungen erfassenden, Turbulenzmodelle sind bis heute in nur wenigen Untersuchungen mit Blasenströmungen angewandt worden. Das hier verwendete RSM basiert auf den Arbeiten von Jakirlić et al. ([46], [47], [6], [70] und [71]) für inkompressible einphasige Strömungen und liegt dabei in zwei unterschiedlichen Formulierung vor. Die erste entspricht dem konventionellen Ansatz der Reynolds-gemittelten Navier-Stokes Gleichungen und die zweite einer instationären skalenauflösenden Formulierung zur Erfassung der turbulenten Fluktuationen. Letztere basiert auf dem Ansatz der Skalen-adaptiven Simulation (SAS) nach einem Vorschlag von Menter und Egorov [76].

Die Implementierung und Anpassung des RSM in die Euler-Euler Methode und die damit benötigten Anpassungen der Modelle bergen große Herausforderungen hinsichtlich der numerischen Kopplung. Zusätzlich werden Modelle zur Erfassung der blaseninduzierten Turbulenz verwendet. Drei unterschiedliche Anwendungsfälle von turbulenten Blasenströmungen dienen zur Validierung: Turbulente Blasenströmungen in einem senkrechten Rohr bei verschiedenen Reynoldszahlen, die Strömung durch eine plötzliche Querschnittserweiterung in einem senkrechten Rohr und eine Blasensäule mit quadratischem Querschnitt. Für die ersten beiden Testfälle werden die korrespondierenden einphasigen Strömungen erstmalig mit den vorliegenden Reynolds-Spannungs-modellen berechnet.

In den durchgeführten Simulationen zeigt das konventionelle RSM eine sehr gute qualitative Übereinstimmung mit den experimentellen Referenzwerten und erreicht in einem Großteil der Fälle ebenso eine quantitative Übereinstimmung. Die skalenauflösende Formulierung zeigt das vorhandene Potential solch einer neuartigen Formulierung und sollte in nachfolgenden Untersuchungen weiter analysiert werden.

Acknowledgements

This work has been carried out during my time at the Fachgebiet für Strömungslehre und Aerodynamik (SLA) of the Technische Universität Darmstadt between September 2011 and April 2015.

First of all I would like to thank Prof. Dr.-Ing. Cameron Tropea for the opportunity to do this work at his institute and especially for the financial support during the last three months. My special thanks goes to my direct supervisor Apl. Prof. Dr.-Ing. Suad Jakirlić who made all of this possible by giving me the chance to do this thesis. His easygoing kind and continuous support helped me a lot.

Great thanks go to my colleague and former master thesis supervisor Dr.-Ing. Robert Maduta who constantly supported me with with his comments, knowledge and ideas that I actually consider him as a another supervisor. His honest interest in my topic was a decisive contribution to the success of this work and encouraged me a lot over these last years.

I would like to thank my former colleagues for the funny and good times we had. From all of them, my special thanks go to my office mate Rüdiger Röhrig and my former student Benjamin Krumbein, whose master thesis was an excellent contribution to this thesis, for their support during the daily work and for the enjoyable and pleasant time in the office. Thanks go to Stephanie Lath who had to deal with the administrative work of my project. Dr. rer. nat. Hubert Marschall is thanked for his attempt to teach me at least a little bit about good old-fashioned fluid mechanics, for continuously listen to my problems and for his special sense of humor.

The proof reading by Dr.-Ing. Robert Maduta, Rüdiger Röhrig, Benjamin Krumbein and Dr.-Ing. Jakob Faber is highly acknowledged.

Last but not least, I would like to thank my family who always supported me throughout my entire life.

Contents

1 Introduction

Turbulent multiphase flows occur in a wide range of industrially relevant applications, as for instance in the chemical industry, oil industry and in nuclear engineering. One frequently encountered constellation are the gas-liquid two-phase flows, see for e.g. Ishii and Hibiki [44]. A variety of possible flow regimes exist, as e.g. separated, mixed and dispersed flows. In the field of computational fluid dynamics (CFD) these flows can be modeled in different ways, depending on the considered regime, the phenomena of interest and the acceptable computational cost. A comprehensive overview of this subject can be found in Rusche [88]. The most popular methods are the volume of fluid (VOF) method, first proposed by Hirt and Nichols [39], and the level set method, introduced by Sethian [96]. Both approaches are based on the solution of a partial differential equation describing the dynamics of an indicator function, which identifies appropriately the phases constituting the fluid system under consideration at a specific point and a certain time in the flow domain. With these methods a (more or less) clearly defined interface between two present phases, as e.g. a free surface in a gas-liquid flow, is computationally determined. A major difficulty is the fact that a highly accurate resolution of the interface, in both spatial and temporal sense, has to be guaranteed in order to obtain a correct outcome. Hence, the resolution provided by the numerical grid has to be considerably finer than the spatial extent of the investigated interface between the phases. As an example, the numerical resolution of an uprising gas bubble in a surrounding liquid phase has to be an order of magnitude smaller than the diameter of the bubble itself. Clearly, the associated computational cost for a flow configuration of practical relevance, with a potentially unlimited number of gas bubbles, are beyond the reach of the industrially affordable numerical resources.

Fortunately, from the engineering point of view, the instantaneous flow features are commonly of little interest, since the main focus lies on comparable statistically averaged quantities. The most widely used computational approach resulting in a corresponding outcome is the two-fluid model (TFM) or the Euler-Euler model, formulated by Ishii and Hibiki [44], which

is based on the idea of two inter-penetrating continua. In this approach a particular set of conditionally-averaged equations governing the mass and momentum transport is formulated for each phase separately. Accordingly, the physical rationale of the two-fluid modeling approach makes this method in general incapable of resolving the interface between the two phases, and subsequently the individual gas bubbles. Instead, it results in a statistically evaluated phase fraction field. As a final outcome of such a computational methodology, the need for an extraordinarily fine grid resolution, associated with high computational expenses, as it is the case when employing the VOF method, is omitted. On the other hand, the consequence of the afore mentioned averaging procedure is the loss of information about the structural features of the flow, being manifested due to the appearance of two different groups of unclosed terms. These terms have to be appropriately closed, i.e. the TFM approach requires relevant closure models describing the interfacial momentum transfer between the involved phases and for the turbulent stresses present in each phase. While the interfacial momentum transfer is presently modeled in line with some widely accepted modeling formulations (proposed by Tomiyama et al. [103], Legendre and Magnaudet [62], Auton [3], Zhang et al. [114] and Lahey et al. [58]), the prime objective of this work is connected with a higher-order modeling of the turbulent quantities associated with the continuous liquid phase.

Thesis objectives

The main focus thereby lies on the models based on the solution of the equations describing the evolution of the Reynolds-stress model (RSM) components within the Reynolds-averaged Navier-Stokes (RANS) computational framework. These anisotropy resolving models, employed in combination with the TFM, have been used in the past by just a few groups (as e.g., by Cokljat et al. [15], Lopez de Bertodano et al. [66] , Chahed et al. [14] and recently by Colombo and Fairweather [16]), despite their superior theoretical foundations. The largest majority of bubbly flow computations performed by employing conventional RANS models utilize the standard high Reynolds number two-equation eddy-viscosity models, based on the solutions of the transport equations of the kinetic energy of turbulence (k) and its dissipation rate (ε). These RANS models are usually extended through introduction of some additional source terms in the model equations accounting for the so-called bubble-induced turbulence. An overview

of the most relevant modeling formulations for this bubble-induced turbulence (BIT) can be found in Rzehak and Krepper [89]. The presently adopted differential Reynolds-stress models, accounting also for the near-wall turbulence, are based on the formulations proposed initially by Jakirlić and co-workers (see e.g., Jakirlic [46], Jakirlić and Hanjalić [47], Basara and Jakirlić [6] and Maduta [70]) for incompressible single-phase flows. Two essentially different versions of this RSM are selected to be applied in the present work. One model version is formulated within the conventional RANS framework, whereas the second one resembles an instability-sensitized RSM (IS-RSM) variant, capable of appropriately resolving the fluctuating turbulence. Both modeling formulations employ the inverse turbulent time scale ($\omega^h = \varepsilon^h/k$) as the length scale determining variable, see Maduta [70]. The corresponding transport equation is appropriately extended in accordance with the scale-adaptive simulation (SAS) proposal for the IS-RSM, formulated principally by Menter and Egorov [76] in conjunction with the eddy-viscosity model group. This SAS relevant model scheme, representing a novel unsteady RANS model, is capable of capturing the turbulent vortex variability, in line with some popular hybrid RANS/LES (large eddy simulation) approaches. Unlike the most hybrid approaches, modeled in terms of numerical grid spacing, the presently adopted IS-RSM represents a grid-spacing free model formulation. The IS-RSM formulation implies a selective enhancement of the production rate of the ω^h-variable modeled in terms of the von Kármán length scale comprising the second derivative of the velocity field. This von Kármán length scale represents a key element in triggering the flow to generate resolved turbulence within the SAS framework, in analogy to the grid spacing in LES and LES-relevant methods. This modification enables the fluctuating turbulent flow field to be resolved to an appropriate extent, representing the feature which is otherwise suppressed in conventional RANS computations. Both Reynolds-stress model variants have been intensively validated in numerous single-phase flow configurations by Maduta [70] and Jakirlić and Maduta [49]. Lately, Maduta et. al [71] proposed a numerical improved formulation for this scale-resolving method.

Outline of the thesis

The present study is primarily focused on the simulation of turbulent bubbly flows, i.e. finely dispersed air bubbles in water, utilizing the two-fluid model in conjunction with both conventional and instability-sensitized

Reynolds-stress models. This stands in large contrast to the typical state of the art approaches, based on the standard high Reynolds number two-equation turbulence modeling concept, relying mostly on the $k-\varepsilon$ model formulation proposed by Launder and Spalding [61]. The implementation of the presently adopted Reynolds-stress models into the TFM computational framework, also in conjunction with two selected BIT models, request an appropriate coupling, which, independent of the geometrical complexity of the flow configurations considered, represents a high-challenge task. Accordingly, the numerical algorithm has to provide a due physical accuracy within a numerical environment featured by a stable and efficient iterative procedure. A number of relevant flow configurations serving for the modeling validation are selected. Prior to the two-phase flow computations, the turbulence models predictive capabilities are analyzed by computing the available corresponding single-phase flow configurations.

The open source software OpenFOAM® [78] (version 2.2.x) based on the finite-volume method on unstructured collocated meshes, offering a variety of pre-implemented solvers and discretization schemes, represents the numerical platform of the present study. Starting point hereby is the *compressibleTwoPhaseEulerFoam* solver, whose substantial aspects are explained by Rusche [88], serving as the basic solver for the two-phase flow computations by utilizing the two-fluid model. This solver uses the pressure implicit with splitting operators (PISO) algorithm by Issa [45] as the calculation procedure for the pressure velocity coupling. The numerical rationale underlying the here realized computations are outlined in Chapter 2, whereby the basic principles of the finite-volume method including the spatial and temporal discretization techniques are explained.

Since the main focus of this work lies on turbulence modeling, Chapter 3 explains the fundamentals of the turbulence modeling with the main focus on the RANS, i.e. URANS modeling framework. Both conventional and scale-resolving near-wall Reynolds-stress models are explained in detail, as well as the widely used low Reynolds number $k-\varepsilon$ model from Launder-Sharma [60], which is additionally applied for comparative assessment in both single- and two-phase flow.

In Chapter 4, the modeling strategy used for the two-phase flow computations is presented, which includes the basic equation system describing the two-fluid model proposed initially by Ishii and Hibiki [44]. Differently

formulated interfacial momentum closure models, originating from different studies, analyzed computationally in the present work are specified. The remainder of the chapter deals with the turbulence modeling of the carrier liquid phase and its interaction with the dispersed bubbly phase within the TFM approach. A description of the common turbulence modeling strategy is included as well as the relevant modifications of the single-phase flow turbulence models (outlined in Chapter 3) with respect to application to the present two-phase flows. It relates especially to the presentation of two selected models accounting for the bubble-induced turbulence. These are the models proposed by Rzehak and Krepper [89] and Troshko and Hassan [105].

Finally, the chapters 5, 6 and 7 accommodate the results and relevant analysis of the computations of three relevant two-phase flow configurations. Careful selection of the flow cases has been performed in accordance to the inherent flow and turbulence features requiring special consideration in the computational modeling. The comprehensiveness of the mostly experimental reference investigations is also one of the selection criteria. It should be emphasized that accounting for the effects of the dispersed bubbly phase on the continuous liquid phase strongly increases the complexity of the underlying computational treatment. Accordingly, a liquid-gas two-phase flow inherently represents a very complex flow system, even if it occurs in a simple geometry, as e.g. in a straight pipe. The predictive performances of the proposed models are evaluated by computing three flow configurations of different complexity. The first flow configuration is the turbulent bubbly flow in a vertical pipe investigated experimentally by Hosokawa and Tomiyama ([40] and [41]) over a range of Reynolds numbers. A flow through a sudden expansion in a vertical pipe represents the second flow configuration, which introduces the effects of a boundary layer separation on the liquid-gas interaction. The flow domain dimensions and the operating conditions are adopted in line with the experimental work from Bel Fdhila [9]. Both computational campaigns are accompanied by additional investigations dealing with the corresponding single-phase flow counterparts, also within a corresponding Reynolds number range. The reference direct numerical simulation (DNS) database is provided by Wu et al. [112] and Khoury et al. [55] for the pipe flow and the measurements of Dellenback et al. [23] serve as the basis for the suddenly expanded pipe flow. The consequent two-phase flow computations benefited strongly from the flow structure analysis obtained by computing the single-phase flows.

Whereas the previous two flow geometries are two-dimensional in mean (it is recalled that the application of the eddy-resolving RSM requires a three-dimensional treatment) the third flow configuration represents a real three-dimensional configuration. It deals with a square cross-sectioned bubble column based on the data by Deen [20] and Zhang et al. [114].

The study concludes with a discussion in Chapter 8 regarding the results achieved, suggesting directions for further investigations.

2 Basics of computational fluid dynamics: Finite-volume method

Since this study focuses on the simulation of turbulent flows, a numerical approach has to be utilized to solve the present non-linear second order partial differential equation system. An analytic solution of these equations exists only for some special or simplified cases, such as laminar unidirectional flows, and on no account for turbulent flows. In the present chapter, s short introduction to the main numerical aspects of computational fluid dynamics (CFD) is given. The most often utilized technique in the field of CFD, is the finite-volume method (FVM). Its main purpose is to transform a set of continuous coupled differential equations into a set of discrete coupled algebraic equations and solve them afterwards. The FVM follows several steps, in detail explained by many authors like Schäfer [92] or Ferziger and Perić [27], which will be illustrated here by using the example of the differential form of a generic transport equation for a general quantity Φ

$$\underbrace{\frac{\partial \Phi}{\partial t}}_{\text{time derivative}} + \underbrace{\frac{\partial}{\partial x_j}\left(U_j \Phi\right)}_{\text{convection}} = \underbrace{f}_{\text{source terms}} + \underbrace{\frac{\partial}{\partial x_j}\left(\Gamma \frac{\partial \Phi}{\partial x_j}\right)}_{\text{diffusion}} \tag{2.1}$$

with the instantaneous velocity field U_j, the diffusion coefficient Γ and the source term f. Instead of solving this differential form, the FVM utilizes the integral form of Eq. (2.1) over a control domain V and applying the Gauss theorem, see for example Spurk [100], to transform the convective and diffusion term into surface integrals which leads to

$$\int_V \frac{\partial \Phi}{\partial t}\,\mathrm{d}V + \int_{S_V} \left(U_j \Phi - \Gamma \frac{\partial \Phi}{\partial x_j}\right) n_j \,\mathrm{d}S = \int_V f \,\mathrm{d}V \tag{2.2}$$

with S_V and n_j being the surface of the control domain and the corresponding normal vector pointing out of the domain. The key aspect of the FVM after the derivation of Eq. (2.2) is the spatial discretization of V into a finite number of non-overlapping discrete control volumes (CVs) or cells.

Through the presence of the temporal derivative term in Eq. (2.2), a temporal discretization technique has to be applied too. Both discretization procedures are explained hereinafter.

2.1 Spatial discretization

After the spatial discretization of V, every CV has an associated computational point P located in its center, where the calculated quantities are stored. All further steps leading to the discretized form of Eq. (2.2) are explained for an orthogonal two-dimensional grid as it is shown in Fig. 2.1, whereby the surfaces and the neighboring CVs of the cell with the computational node P are denoted through compass notation.

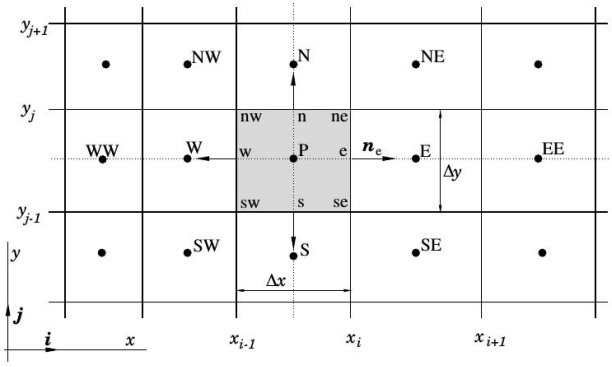

Figure 2.1: Two-dimensional solution domain taken from Ferziger and Perić [27]

Therewith the surface integrals in Eq. (2.2) are divided into the sum of the four surfaces S_c (e, w, n, s) of the CV, yielding

$$\int_{V_P} \frac{\partial \Phi}{\partial t}\,\mathrm{d}V + \sum_c \int_{S_c} \left(U_j \Phi - \Gamma \frac{\partial \Phi}{\partial x_j} \right) n_j \,\mathrm{d}S = \int_{V_P} f \,\mathrm{d}V. \tag{2.3}$$

These surface and volume integrals have to be converted through appropriate interpolation schemes to transform the continuous equation Eq. (2.3)

into a discrete equation for every CV. The volume integrals and surface integrals are thereby considered separately. The resolution of the grid and therewith the number of computational points has to be increased until no variation in the results can be observed anymore and a grid independent solution is achieved.

Volume integrals

The approximation of the source terms is carried out by utilizing the midpoint rule, thus the integral is approximated by the product of the volume of the CV and the value of f at the centerpoint P, hence f_P represents the average value in the CV. This leads to

$$\int_{V_P} f \, \mathrm{d}V \approx f_P \Delta V_P \tag{2.4}$$

with ΔV_P denoting the volume of the CV. According to Ferziger und Perić [27] Eq. (2.4) represents the easiest second-order approximation. A major advantage is the fact that all variables are available at P, meaning that no additional interpolation is required.

Surface integrals

The surface integral in Eq. (2.3) is divided into a term representing the convective and diffusive flux over the respective CV surface and is approximated by applying the midpoint rule, hence expressing the values at the face through the value at the center of the respective surface. This leads to

$$\sum_c \int_{S_c} (U_j \Phi) \, n_j \, \mathrm{d}S \approx \sum_c \left(S n_j\right)_c \left(U_j\right)_c \Phi_c = \sum_c F_c \Phi_c \tag{2.5}$$

for the convective flux, with $F_c = \left(U_j\right)_c \left(S n_j\right)_c$ representing the volume flux over the surface S_c. $\left(U_j\right)_c$ is hereby linearly interpolated onto the cell surface. The diffusive flux is approximated via

$$\sum_c \int_{S_c} \left(\Gamma \frac{\partial \Phi}{\partial x_j}\right) n_j \, \mathrm{d}S \approx \sum_c \left(\Gamma \frac{\partial \Phi}{\partial x_j} S n_j\right)_c . \tag{2.6}$$

Since no computational data is stored at the cell surfaces, these values have to be approximated by the cell center values of the neighboring CVs, through appropriate interpolation schemes. The schemes utilized in this work are briefly introduced by taking the example of the eastern face e.

Discretization of the diffusive fluxes

The most frequently used interpolation scheme for discretizing the normal derivative in the diffusion term is the central differencing scheme (CDS) which interpolates linearly between the neighboring cell centers, resulting in

$$\left(\frac{\partial \Phi}{\partial x}\right)_e \approx \frac{\Phi_E - \Phi_P}{x_E - x_P} \tag{2.7}$$

with the denominator representing the distance between the cell centers of P and E. This scheme is second order accurate in space for equidistant distances between the cell centers. For the case of non-orthogonal grids, an additional correction to Eq. (2.7) has to be applied, which is for instance explained by Jasak [50].

Discretization of the convective fluxes

A huge number of interpolation schemes has been proposed so far for discretizing the convective term. Two of them are of special interest, because they usually represent the bounds of nearly all common schemes in terms of the order of accuracy. The first one is the previously presented CDS which leads to

$$\Phi_e = \Phi_E \lambda_e + \Phi_P \left(1 - \lambda_e\right) \tag{2.8}$$

with the interpolation factor λ_e defined through

$$\lambda_e = \frac{x_e - x_P}{x_E - x_P}. \tag{2.9}$$

While being second order accurate in space, the CDS does not guarantee boundedness and can lead to numerical oscillations as it is in detailed explained by Versteeg and Malalasekera [106]. Another interpolation scheme which can guarantee this boundedness, but is only first order accurate in space is the upwind differencing scheme (UDS), which interpolates the value at the face by the neighboring upstream value. Therefore it uses the volume flux at face e to decide which value to take, yielding

$$\Phi_e \approx \begin{cases} \Phi_P & \text{if } F_e > 0 \\ \Phi_E & \text{if } F_e < 0. \end{cases} \tag{2.10}$$

A major disadvantage thereby is the introduction of a huge amount of numerical diffusion, see for example Versteeg and Malalasekera [106], which can lead to the damping of instantaneous flow structures and is therefore

especially not applicable for eddy-resolving methods, such as the large eddy simulation (LES). To combine the advantages of both schemes, a face by face blending between the value obtained with Eq. (2.8) Φ_e^{CDS} and the one obtained with Eq. (2.10) Φ_e^{UDS} can be applied aiming to guarantee boundedness while introducing as little numerical diffusion as possible. Such a blending is in general described through

$$\Phi_e = \Phi_e^{\mathrm{UDS}} + \gamma \left(\Phi_e^{\mathrm{CDS}} - \Phi_e^{\mathrm{UDS}} \right) \tag{2.11}$$

with the blending function γ ranging between zero and one. A huge number of possible formulations for γ, depending on the flow conditions at each face, can be found in the literature, see for example Jasak [50], to guarantee boundedness, while preserving a high amount of CDS as far as possible. In this study a constant value for γ at all faces of the mesh is utilized as it was proposed by Perić [79], which falls back into the limits

$$\gamma = \begin{cases} 0 = \mathrm{UDS} \\ 1 = \mathrm{CDS}. \end{cases} \tag{2.12}$$

This clearly does not guarantee boundedness for values of γ larger than zero or guarantee the prevention of high amount of numerical diffusion for values smaller than one, but often serves well for simulations where CDS cannot be applied for stability reasons.

2.2 Temporal discretization

In transient calculations the physical quantities are not only spatially but also temporally varying. Therefore it is necessary to use appropriate discretization techniques to capture the time depending behavior, which are explained by integrating the spatially discretized Eq. (2.1) over a time interval Δt from time t, with the already known values Φ_P^n, to time $t + \Delta t$, with the new unknown values Φ_P^{n+1}, yielding

$$\int_t^{t+\Delta t} \frac{\partial \Phi_P}{\partial t} V_P dt = \int_t^{t+\Delta t} \mathcal{L}\left(\Phi_P\right) dt \tag{2.13}$$

with the operator $\mathcal{L}$ containing the spatially discretized convection, diffusion and source terms. In this work only implicit methods are considered for evaluating the time depending behavior, meaning that $\mathcal{L}\left(\Phi_P\right)$ is also

expressed through values at the new unknown time level $n+1$, see e.g. Jasak [50] for a detailed explanation. The temporal derivative term is hereby discretized via two different implicit differencing schemes. The first one is the well-known implicit Euler method which is defined by

$$\frac{\partial \Phi_P}{\partial t} \approx \frac{\Phi_P^{n+1} - \Phi_P^n}{\Delta t} \tag{2.14}$$

and is first order accurate in time. A second-order accurate time scheme is the implicit backward differencing formula (BDF) whereby the temporal derivative is discretized by

$$\frac{\partial \Phi_P}{\partial t} \approx \frac{3\Phi_P^{n+1} - 4\Phi_P^n + \Phi_P^{n-1}}{2\Delta t} \tag{2.15}$$

including a previously computed value Φ_P^{n-1} and with Δt restricted to an equidistant time step. There are, of course, restrictions for the possible magnitude of Δt, in terms of physical effects and numerical requirements. A possible measure for choosing a suitable time step is the Courant (or Courant-Friedrichs-Levy (CFL)) number

$$Co = \frac{U_x \Delta t}{\Delta x} \tag{2.16}$$

here e.g. with the velocity U_x and the size of the CV Δx in x-direction. There is no strict limiting value defined for the Courant number by numerical requirements when using implicit time stepping methods. But if Co becomes too large, certain flow features cannot be resolved correctly anymore, especially those who have a smaller period of time than the utilized value of Δt. The aim here is to find a balance between time steps as large as possible, for minimizing the computational cost, and small time steps, necessary for resolving the relevant flow features. A discussion about this can be found e.g. in Bücker et al. [7].

3 Turbulence modeling in single-phase flows

The fundamental basis for the computation of turbulent flows are the non-linear Navier-Stokes equations (see e.g. Spurk [100]), which exactly describe the motion of Newtonian fluids, such as water and air, and thereby most technically relevant flows in fluid mechanics. Furthermore is the theoretical rational of the computational methodology for the two-phase flow investigations also based on these equations. For incompressible fluids, which are the only kind of fluids regarded here (this also accounts for the present two-phase flows), these equations can be written (in Cartesian coordinates) in the following form

$$\frac{\partial U_i}{\partial t} + U_j \frac{\partial U_i}{\partial x_j} = -\frac{1}{\varrho}\frac{\partial P}{\partial x_i} + \nu \frac{\partial}{\partial x_j}\left(\frac{\partial U_i}{\partial x_j} + \frac{\partial U_j}{\partial x_i}\right), \tag{3.1}$$

in conjunction with the continuity equation

$$\frac{\partial U_j}{\partial x_j} = 0 \tag{3.2}$$

with U_i, P, ϱ and ν being the instantaneous velocity, instantaneous dynamic pressure, density and the kinematic molecular viscosity, respectively. This set of coupled differential equations describes the motion of each fluid element at any point in the flow field at all times, which can be either a laminar flow or a turbulent flow. A dimensionless representative quantity to distinguish these flow regimes is the Reynolds number

$$Re = \frac{U L_t}{\nu} \tag{3.3}$$

with U and L_t being a characteristic velocity and length scale of the flow. Re can be interpreted as the ratio of inertia effects to viscous effects. Turbulent flows are characterized by higher Reynolds numbers than laminar flows and are dominated by inertia forces. Nearly all technically relevant flows in fluid mechanics are turbulent, which means that they are characterized by a stochastic, three-dimensional and unsteady behavior, whereby

their computation represents a major challenge both in terms of physical and numerical modeling. In general there is no analytical solution for such kind of flows and therefore appropriate physical models and numerical techniques, presented in the preceding chapter, have to be utilized to make the computation of these flows possible. Three major strategies to simulate turbulent flows can be distinguished, with the classification being carried out in terms of the resolved fraction of the turbulent spectra. This is shown in Fig. 3.1 with the so-called energy cascade process (see e.g. Pope [82]) which is visualized with the energy per wave number $E_\kappa(\kappa)$ being plotted over the wave number κ. In this purely qualitative log-log plot, the energy-containing range (I), the inertial subrange (II) and the dissipation range (III) are shown and the particular amount of resolved turbulent spectra (dashed lines) by the respective strategy.

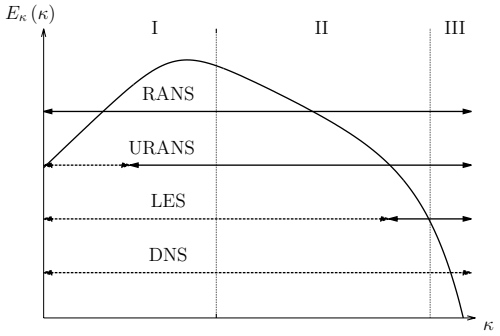

Figure 3.1: Simulation strategies for turbulent flows and the associated part of resolved (dashed lines) and modeled (solid lines) turbulence

The first strategy directly solves Eqs. 3.1 and 3.2 by a direct numerical simulation (DNS), see e.g. Pope [82], without any further assumptions or modeling steps. Unfortunately, this requires the resolution of all scales of motion in the flow field both in time and space, meaning that no part of the turbulence is captured by an additional model. This leads to high demands in terms of computational accuracy and power. Hence the usage of DNS is only feasible for a few academic test cases such as channel flows or flows at small Re numbers, while using DNS for engineering purposes will

be impossible for many more decades. Therefore alternative methods are needed to compute turbulent flows in an economically justifiable time with low computational costs for relevant engineering cases.

The large eddy simulation (LES), see e.g. Fröhlich [28], is such a method, whereby a filtering operation is applied in order to resolve the large energy containing eddies while modeling the small dissipative scales by means of a so-called sub-grid-scale (SGS) model. While the computational effort for LES is much lower than for DNS, the results are satisfying even for complex geometries. On the other hand, LES still requires unsteady computations on appropriate three-dimensional numerical grids and is therefore still a time consuming method with high computational cost and not applicable for most industrially relevant flow configurations, especially when it comes to parametric studies.

The standard strategy to compute turbulent flows nowadays is the utilization of the Reynolds-averaged Navier-Stokes (RANS) equations, whereby only statistically averaged quantities are examined instead of actually resolving the present fluctuating turbulent flow field. This is achieved by subsuming all influence of the turbulent fluctuating motions on the mean flow field within a single turbulence model and no part of the turbulent fluctuations is actually resolved as it is shown in Fig. 3.1. Turbulence models within the classical application of the RANS equation framework are always leading to steady state results which can often be done on two-dimensional grids. This heavily minimizes the computational effort in comparison to scale-resolving methods like DNS and LES. Up to now, RANS is by far the most common way to compute turbulent flows for both academic research and industrial applications. Nevertheless, in some globally unstable flows, like bluff body configurations, it is possible that the RANS equations can lead to an unsteady flow field, which starts to resolve the huge global fluctuating features of the flow. Such simulations are usually classified as the unsteady RANS (URANS) method implying a time integration of the steady RANS equations. In such simulations, the statistically averaged flow quantities are becoming unsteady itself by containing the huge periodic fluctuating motions, but still, the resolved part of the fluctuating motions is much smaller than it is the case for LES as shown in Fig. 3.1. The RANS methodology in detail is explained in the following chapter.

3.1 Reynolds-averaged Navier-Stokes framework

The theoretical rationale of the RANS equations is based on the idea that the influence of the turbulent fluctuating motions on the mean flow field can be expressed with an appropriate statistical turbulence model in order to avoid the resolution of any instantaneous turbulent motions. The derivation of the RANS equations can be found in many textbooks such as Leschziner [63], Tennekes and Lumley [101] or Wilcox [110]. These equations rely on the decomposition proposed by Reynolds [85] at which any instantaneous quantity Φ, irrespective of the rank of the tensor, can be separated into a mean part $\overline{\Phi}$ and a fluctuating part ϕ' through

$$\Phi\left(x_j, t\right) = \overline{\Phi}\left(x_j\right) + \phi'\left(x_j, t\right), \tag{3.4}$$

where the mean quantities are usually defined as time averaged quantities. Inserting this decomposition into the instantaneous quantities in Eq. (3.1) and Eq. (3.2) and averaging them afterwards leads to the averaged momentum equation (with the temporal derivative being included for URANS),

$$\frac{\partial \overline{U}_i}{\partial t} + \overline{U}_j \frac{\partial \overline{U}_i}{\partial x_j} = -\frac{1}{\varrho}\frac{\partial \overline{P}}{\partial x_i} + \nu \frac{\partial}{\partial x_j}\left(\frac{\partial \overline{U}_i}{\partial x_j} + \frac{\partial \overline{U}_j}{\partial x_i}\right) - \frac{\partial \overline{u_i' u_j'}}{\partial x_j} \tag{3.5}$$

and the averaged continuity equation

$$\frac{\partial \overline{U}_j}{\partial x_j} = 0. \tag{3.6}$$

The last term on the right hand side of Eq. (3.5) is a result of the averaging procedure of the non-linear convective term of Eq. (3.1) and is the divergence of the Reynolds-stress tensor, containing all influences of the turbulent fluctuating motions on the mean flow field. Unfortunately, this symmetric 2nd-rank Reynolds-stress tensor consists of six unknown quantities, which leaves the set of equations unclosed. This problem is referred to as the turbulence closure problem, which has led to the development of appropriate statistical turbulence models to solve this problem and close Eq. (3.5). The theoretical development of these turbulence models and their calibration through benchmark test cases has been the major issue in the engineering relevant research of turbulent flows during the past decades. Those mentioned turbulence models can be mainly classified into two different modeling strategies, which are the eddy-viscosity models (EVMs) and the second-moment closure (SMC) models.

The first approach is based on the so-called eddy-viscosity concept, originally proposed by Boussinesq [11], which uses an analogy to the Newtonian model for the viscous stresses and therefore relates the Reynolds-stress tensor linearly proportional to the mean rate of strain tensor

$$S_{ij} = \frac{1}{2}\left(\frac{\partial \overline{U}_i}{\partial x_j} + \frac{\partial \overline{U}_j}{\partial x_i}\right) \tag{3.7}$$

leading to

$$\overline{u_i' u_j'} = -2\nu_t S_{ij} + \frac{2}{3}k\delta_{ij} = -\nu_t\left(\frac{\partial \overline{U}_i}{\partial x_j} + \frac{\partial \overline{U}_j}{\partial x_i}\right) + \frac{2}{3}k\delta_{ij}. \tag{3.8}$$

This introduces the eddy viscosity ν_t, which is a purely modeled quantity, rather than being based on an exact physical quantity. While ν is a property of the fluid, the turbulence and hence ν_t is a property of the flow itself. δ_{ij} denotes the Kronecker delta. The turbulent kinetic energy k is defined by

$$k = \frac{1}{2}\overline{u_i' u_i'}. \tag{3.9}$$

A turbulence model, which is based on Eq. (3.8), is called EVM. Inserting Eq. (3.8) into Eq. (3.5) leads to

$$\frac{\partial \overline{U}_i}{\partial t} + \overline{U}_j\frac{\partial \overline{U}_i}{\partial x_j} = -\frac{1}{\varrho}\frac{\partial \overline{P}}{\partial x_i} + \frac{\partial}{\partial x_j}\left[(\nu+\nu_t)\left(\frac{\partial \overline{U}_i}{\partial x_j} + \frac{\partial \overline{U}_j}{\partial x_i}\right) - \frac{2}{3}k\delta_{ij}\right]. \tag{3.10}$$

The advantage of this approach is obvious since it simplifies the turbulence closure problem towards the modeling of the two scalar variables ν_t and k, instead of the six independent components of the Reynolds-stress tensor. On the other hand is an EVM not capable of capturing the Reynolds-stress anisotropy accurately, since this aspect is only weakly expressed through the mean velocity gradient and not directly through the turbulent quantities. This is the most important weakness of such models and usually leads to poor results for flow configurations with swirling effects or strong streamline curvature. Various models have been developed so far to compute ν_t and k. The models for ν_t are most commonly based on a dimensional analysis, using an analogy to the gas kinetic theory assuming the eddy viscosity being linear to a characteristic eddy length l and a velocity scale v leading to

$$\nu_t \propto lv. \tag{3.11}$$

This was first proposed by Prandtl [84] within the mixing length theory. A common practice in the EVM framework is to determine these quantities by the use of two-equation models, solving two additional transport equations for the determination of ν_t and k. All of these models usually associate the velocity scale with the large energy containing eddies in the energy cascade and consequentially relate them to the turbulence kinetic energy via

$$v = \sqrt{k}. \tag{3.12}$$

Therefore an equation for k has to be modeled and solved. The determination of l remains a less restricted field for discussions and proposals, having in common that l is usually related to quantities which represent the small energy dissipating eddies in the energy cascade. Several turbulent quantities have been proposed so far, whereby the most common one is the dissipation rate ε of the turbulent kinetic energy k defined by

$$\varepsilon = \nu \overline{\frac{\partial u_i'}{\partial x_k} \frac{\partial u_i'}{\partial x_k}}. \tag{3.13}$$

Thus, l can be expressed in terms of k and ε leading to

$$l = \frac{k^{3/2}}{\varepsilon} \tag{3.14}$$

and therewith ν_t can be expressed through

$$\nu_t \propto \frac{k^2}{\varepsilon}. \tag{3.15}$$

A modeled equation for ε is usually the second one in a two-equation turbulence model (besides the one for k), with the standard k-ε model by Launder and Spalding [61] being the most famous representative of this kind of turbulence models. Another common quantity which is often used to model the turbulent length scale is the inverse turbulent time scale $\omega = \varepsilon/k$ proposed by Wilcox [109] (and also used by Menter [72]). Hence using an EVM usually consists of the definition and solution of two transport equations, one for k and one for an additional length-scale supplying equation, to close the RANS equation system through Eq. (3.10).

Besides the usage of eddy-viscosity models, the second broad modeling strategy within the RANS framework is the utilization of a SMC model or also called Reynolds-stress model (RSM). This model group is based on the

attempt to determine every single component of $\overline{u_i' u_j'}$ from its own modeled transport equation and thereby capturing the anisotropy of the Reynolds-stress tensor. Detailed information about SMC models and an extensive introduction into the theoretical rationale can be found in Hanjalić and Launder [36]. The basis hereby are the exact transport equations for $\overline{u_i' u_j'}$ introducing a crucial number of additional unclosed terms, which makes the modeling effort of SMC models more complex in comparison to models based on the eddy-viscosity assumption. On the other hand, SMC models are in general regarded as the more rational approach in comparison to an EVM since the required closure is shifted from the momentum equation, no Boussinesq assumption is needed, into the equations for the turbulent quantities itself. The exact transport equation for the Reynolds-stress tensor read:

$$\begin{aligned}
\frac{\partial \overline{u_i' u_j'}}{\partial t} + \overline{U}_k \frac{\partial \overline{u_i' u_j'}}{\partial x_k} \quad = \quad & \underbrace{-\left(\overline{u_i' u_k'} \frac{\partial \overline{U}_j}{\partial x_k} + \overline{u_j' u_k'} \frac{\partial \overline{U}_i}{\partial x_k} \right)}_{P_{ij}} + \underbrace{\frac{\partial}{\partial x_k} \left(\nu \frac{\partial \overline{u_i' u_j'}}{\partial x_k} \right)}_{\mathcal{D}_{ij}^{\nu}} \\
& + \underbrace{\overline{\frac{p'}{\varrho} \left(\frac{\partial u_i'}{\partial x_j} + \frac{\partial u_j'}{\partial x_i} \right)}}_{\Phi_{ij}} - \underbrace{2\nu \overline{\frac{\partial u_i'}{\partial x_k} \frac{\partial u_j'}{\partial x_k}}}_{\varepsilon_{ij}} \\
& + \underbrace{\frac{\partial}{\partial x_k} \left(-\overline{u_i' u_j' u_k'} \right)}_{\mathcal{D}_{ij}^{t}} + \underbrace{\frac{\partial}{\partial x_k} \left(-\overline{\frac{p'}{\varrho} \left(u_i' \delta_{jk} + u_j' \delta_{ik} \right)} \right)}_{\mathcal{D}_{ij}^{p}} .
\end{aligned} \tag{3.16}$$

The first two terms on the right hand side of Eq. (3.16), namely the production P_{ij} and viscous diffusion $\mathcal{D}_{ij}^{\nu}$, are exact and need no further modeling. The fact that P_{ij} is exact represents the most superior feature of an RSM in comparison to an EVM. Unfortunately, the remaining terms on the right hand side are unclosed and need further modeling, namely the pressure redistribution Φ_{ij}, the turbulent diffusion due to velocity fluctuations $\mathcal{D}_{ij}^{t}$, the turbulent diffusion due to pressure fluctuations $\mathcal{D}_{ij}^{p}$ and the stress dissipation rate tensor ε_{ij}. This allows a more detailed modeling strategy than it is possible for the case of an EVM, but on the other hand also increases the computational effort and imposes the danger of unwanted numerical instabilities. A length-scale supplying equation, additional to the six transport equations for $\overline{u_i' u_j'}$, has to be derived and modeled too, for expressing ε_{ij}.

A major challenge in both modeling approaches is the correct capturing of the flow quantities close to solid walls. These near-wall regions are strongly influenced by viscous effects, wall blockage effects and characterized by an increased anisotropy of $\overline{u_i' u_j'}$. A dimensionless quantity to determine these areas in a flow configuration is the normalized wall distance y^+, which is defined through the normalization of the wall distance y by ν/u_τ leading to

$$y^+ = \frac{y u_\tau}{\nu}. \tag{3.17}$$

Here, the wall friction velocity is defined through

$$u_\tau = \sqrt{\frac{\tau_w}{\varrho}} \tag{3.18}$$

with the wall shear stress τ_w. y^+ offers a distinguished classification of the different areas in the flow field. An example therefore is shown in Fig. 3.2a for a plane channel flow at $Re_\tau = u_\tau \mathrm{H}_c/\nu = 395$ with H_c being the half of the channel height. The DNS reference data is taken from Kim et al. [56].

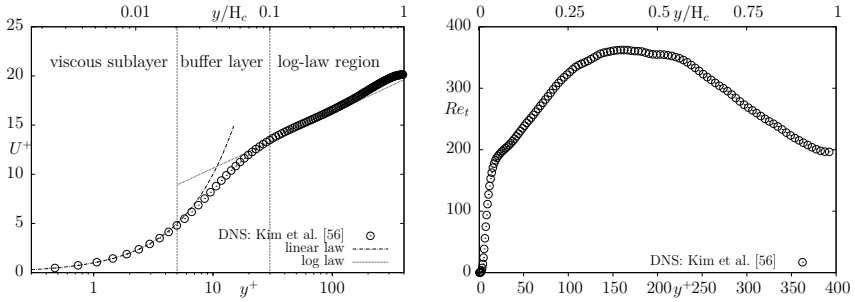

(a) Semi-log $y^+ - U^+$ plot

(b) Turbulent Reynolds number Re_t

Figure 3.2: Turbulent flow features in a plane channel flow at $Re_\tau = 395$

Three major regions can be classified. In the viscous sub-layer for $y^+ < 5$ the flow is dominated by viscous effects, while in the log-law region for $y^+ > 30$ the flow is dominated by turbulent processes. The normalized velocity $U^+ = U/u_\tau$ in both regions can be described by particular velocity laws:

$$U^+ = \begin{cases} y^+ & \text{for } y^+ < 5 \\ \frac{1}{\kappa} \ln y^+ + \mathrm{B} & \text{for } y^+ > 30 \end{cases} \tag{3.19}$$

with $\kappa = 0.41$ and $B = 5$ based on experimental observations and DNS data. In the buffer layer area, both turbulent and viscous effects overlap and a specific velocity law cannot easily be defined. The turbulent Reynolds number $Re_t = k^2/(\nu\varepsilon)$ can be interpreted as an important measure to decide whether the viscous effects can be neglected or not. The evolution of Re_t, going to zero in areas close to a solid wall, is shown for a plane channel flow in Fig. 3.2b. Providing a turbulence model that is capable of capturing the viscosity dominated effects in the immediate wall vicinity at very low Re_t is a challenging task, both in terms of physical arguments and computational effort. Therefore the majority of turbulence models bridge the flow regions below $y^+ < 30$ by using the well-known wall-functions by Launder and Spalding [61], thereby avoiding the integration up to the wall. These models are denoted as high Reynolds number models. In comparison to that, the models utilized in this work are so-called low Reynolds number models, which are specifically developed to resolve the viscous sub-layer and associated turbulent features.

3.2 Presently employed turbulence models

In the present study three specific low Reynolds number turbulence models are used for expressing the Reynolds-stress tensor in Eq. (3.5). These are the eddy-viscosity model by Launder and Sharma [60] and both Reynolds-stress models by Jakirlić and Maduta ([70] and [49]), with one being formulated in a conventional RANS model sense and one extended towards an eddy-resolving URANS model. The presentation of the latter one includes a short introduction to the fundamental aspects of URANS respectively the hybrid RANS/LES framework.

3.2.1 Launder-Sharma eddy-viscosity model

The original $k - \varepsilon$ model by Jones and Launder [51], based on the proposed equations by Hanjalić [32], is a low Reynolds number model. A high Reynolds number version of this model is the famous standard $k - \varepsilon$ by Launder and Spalding [61]. Many authors introduced their own modifications of the model by Jones and Launder [51] which differ primarily in form of the damping functions towards the low Reynolds number regions close to a solid wall. One of the most popular version is the one of Launder and Sharma [60] and is therefore utilized in this work, serving as a benchmark model to compare both RSMs against. The first step for an

appropriate determination of the near-wall regions is the enhanced computation of ν_t including a damping function f_μ to account for viscous effects. This leads to

$$\nu_t = f_\mu C_\mu \frac{k^2}{\tilde{\varepsilon}} \tag{3.20}$$

with $\tilde{\varepsilon}$ being the "quasi-homogeneous" dissipation rate defined through

$$\tilde{\varepsilon} = \varepsilon - 2\nu \frac{\partial\sqrt{k}}{\partial x_j}\frac{\partial\sqrt{k}}{\partial x_j}, \tag{3.21}$$

which has the major advantage that $\tilde{\varepsilon}$ goes to zero at solid walls, simplifying the implementation of the boundary conditions. A modeled transport equation for k

$$\frac{\partial k}{\partial t} + \overline{U}_j \frac{\partial k}{\partial x_j} = P_k - \tilde{\varepsilon} - 2\nu \frac{\partial\sqrt{k}}{\partial x_j}\frac{\partial\sqrt{k}}{\partial x_j} + \frac{\partial}{\partial x_j}\left[(\nu + \frac{\nu_t}{\sigma_k})\frac{\partial k}{\partial x_j}\right], \tag{3.22}$$

being based on the corresponding exact equation is solved to determine the velocity scale v. The empirical length-scale supplying equation reads

$$\frac{\partial \tilde{\varepsilon}}{\partial t} + \overline{U}_j \frac{\partial \tilde{\varepsilon}}{\partial x_j} = C_{\tilde{\varepsilon}1}\frac{P_k}{k}\tilde{\varepsilon} - C_{\tilde{\varepsilon}2} f_{\tilde{\varepsilon}2}\frac{\tilde{\varepsilon}}{k}\tilde{\varepsilon} + P_{\tilde{\varepsilon},3} + \frac{\partial}{\partial x_j}\left[(\nu + \frac{\nu_t}{\sigma_{\tilde{\varepsilon}}})\frac{\partial \tilde{\varepsilon}}{\partial x_j}\right] \tag{3.23}$$

and is based on similarity arguments to the modeled k equation, rather than the exact transport equation for ε. The damping functions are defined by

$$f_\mu = \exp\left[\frac{-3.4}{(1 + Re_t/50)^2}\right] \qquad \text{and} \qquad f_{\tilde{\varepsilon}} = 1 - 0.3\exp\left(-Re_t^2\right) \tag{3.24}$$

in terms of Re_t which is here defined in terms of k and $\tilde{\varepsilon}$. A major weakness of eddy-viscosity models is the fact that the production term P_k has to be modeled by using Eq. (3.8) leading to

$$P_k = -\overline{u_i' u_j'}\frac{\partial \overline{U}_i}{\partial x_j} = \left[\nu_t\left(\frac{\partial \overline{U}_i}{\partial x_j} + \frac{\partial \overline{U}_j}{\partial x_i}\right) - \frac{2}{3}k\delta_{ij}\right]\frac{\partial \overline{U}_i}{\partial x_j} \tag{3.25}$$

instead of being exact as it is the case for SMC models. The near-wall production term $P_{\tilde{\varepsilon},3}$ in Eq. (3.23) represents

$$P_{\tilde{\varepsilon},3} = 2\nu\nu_t \frac{\partial^2 \overline{U}_j}{\partial x_k \partial x_n}\frac{\partial^2 \overline{U}_j}{\partial x_k \partial x_n} \tag{3.26}$$

and was introduced into the equation to be able to reproduce the correct peak value of k in the buffer-layer. The model constants have the following values:

Table 3.1: Coefficients of the Launder-Sharma [60] $k-\varepsilon$ model

C_μ	$C_{\tilde{\varepsilon},1}$	$C_{\tilde{\varepsilon},2}$	σ_k	$\sigma_{\tilde{\varepsilon}}$
0.09	1.44	1.92	1	1.3

3.2.2 Jakirlić-Maduta Reynolds-stress model

In this study the differential near-wall Reynolds-stress model by Jakirlić, Hanjalić and Maduta ([46], [47], [49] and [70]) is used to model the turbulent transport equations within the SMC framework. This model represents an extension to the well-known Reynolds-stress model by Gibson and Launder [30], which can be identified from the asymptotic solution of the here used model in regions far away from solid walls at high Re_t numbers. The unclosed terms in equation Eq. (3.16) are modeled in a term-by-term manner.

Pressure redistribution Φ_{ij}

The pressure redistribution term Φ_{ij} is subdivided into a term representing the slow part, the rapid part and a part for the wall blocking. These terms are modeled according to Jakirlić [46] whereby appropriate low Reynolds number extensions of the model proposed by Gibson and Launder [30] towards near-wall effects are taken into account.

Diffusion terms $\mathcal{D}^t_{ij}$ and $\mathcal{D}^p_{ij}$

The diffusion due to turbulence $\mathcal{D}^t_{ij}$ and pressure fluctuations $\mathcal{D}^p_{ij}$ are usually combined in a single model expression. While Jakirlić and Hanjalić ([46], [47]) utilized the generalized gradient diffusion hypothesis (GGDH) by Daly and Harlow [17] to model these terms, Maduta [70] simplified this expression by using the simple gradient diffusion hypothesis (SGDH) by Shir [97] leading to

$$\mathcal{D}^t_{ij} + \mathcal{D}^p_{ij} = \frac{\partial}{\partial x_k}\left(\frac{\nu_t}{\sigma}\frac{\partial \overline{u'_i u'_j}}{\partial x_k}\right). \tag{3.27}$$

The eddy viscosity ν_t is hereby modeled according to Basara and Jakirlić [6] and should account for both the Reynolds-stress anisotropy and the viscous

effects close to a solid wall and is expressed by

$$\nu_t = 0.144A \underbrace{\sqrt{k}}_{v} \underbrace{\max\left[10\left(\frac{\nu^3}{k\omega^h}\right)^{1/4}; \frac{k^{1/2}}{\omega^h}\right]}_{l}. \tag{3.28}$$

Eq. (3.28) includes a length scale switch between the classical formulation of the turbulent length scale as it is used in Eq. (3.14), here defined with the homogeneous inverse time scale ω^h, and a lower bound formulated in terms of the Komolgorov length scale $l_k = (\nu^3/(k\omega^h))^{1/4}$ accounting for viscous effects. The stress anisotropy is considered by using the two-componentality parameter A of the Reynolds-stress anisotropy tensor introduced by Lumley [68].

Stress dissipation rate tensor ε_{ij}

Modeling the dissipation process, representing the sink term in Eq. (3.16), is more complex for an SMC model than it is for an EVM, since here the dissipation tensor ε_{ij} with six independent components has to be modeled instead of the scalar dissipation rate. Jakirlić and Hanjalić [47] expressed ε_{ij} in form of the homogeneous dissipation concept

$$\varepsilon_{ij} = \varepsilon_{ij}^h + \frac{1}{2}\frac{\partial}{\partial x_k}\left(\nu\frac{\partial\overline{u_i'u_j'}}{\partial x_k}\right) \tag{3.29}$$

to fulfill the correct near-wall behavior of each normalized component of ε_{ij} and thereby avoiding the usage of any wall topography parameters, such as wall-normal unit vectors. The homogeneous part of the dissipation rate tensor ε_{ij}^h is modeled through

$$\varepsilon_{ij}^h = \varepsilon^h\left[(1-f_s)\frac{2}{3}\delta_{ij} + \frac{\overline{u_i'u_j'}}{k}f_s\right] \tag{3.30}$$

following Hanjalić and Launder [35], providing an extension to the classical isotropic approach for high Reynolds number flows by Rotta [87] towards an anisotropic formulation for low Reynolds number flows. The blending function

$$f_s = 1 - \sqrt{A}E^2 \tag{3.31}$$

ensures a smooth transition from small scale anisotropic to isotropic turbulence. E being the two-componentality parameter of ε_{ij}^h in analogy defined

to A. The homogeneous part of the kinetic energy dissipation rate ε^h is defined by

$$\varepsilon^h = \varepsilon - \frac{1}{2}\nu\frac{\partial^2 k}{\partial x_k \partial x_k}. \tag{3.32}$$

Applying these models to Eq. (3.16) leads to the modeled transport equation

$$\begin{aligned}\frac{\partial\overline{u_i'u_j'}}{\partial t} + \overline{U}_k\frac{\partial\overline{u_i'u_j'}}{\partial x_k} &= -\left(\overline{u_i'u_k'}\frac{\partial\overline{U}_j}{\partial x_k} + \overline{u_j'u_k'}\frac{\partial\overline{U}_i}{\partial x_k}\right) + \Phi_{ij} - \varepsilon_{ij}^h \\ &\quad + \frac{\partial}{\partial x_k}\left[\left(\frac{1}{2}\nu + \frac{\nu_t}{\sigma}\right)\frac{\partial\overline{u_i'u_j'}}{\partial x_k}\right]\end{aligned} \tag{3.33}$$

with the Prandtl-Schmidt number σ set to 1.1. An additional length-scale supplying equation has to be determined to calculate ε_{ij}^h via Eq. (3.30) in order to close the equation system.

Length-scale supplying equation ω^h

In contrast to the length-scale supplying equations used in eddy-viscosity models, usually expressed in strict analogy to the modeled k-equation with dimensional consistencies, the present RSM follows the term-by-term modeling by Jakirlić [46] of the exact transport equation for ε. Jakirlić and Hanjalić [47] reformulated this transport equation into one for ε^h and Maduta [70] continued this work towards an equation for the homogeneous part of the inverse turbulent time scale $\omega^h = \varepsilon^h/k$ by deriving a corresponding transport equation using the relationship

$$\frac{D\omega^h}{Dt} = \frac{1}{k}\frac{D\varepsilon^h}{Dt} - \frac{\varepsilon^h}{k^2}\frac{Dk}{Dt} \tag{3.34}$$

with a simplified version of the modeled ε^h equation, see Jakirlić and Maduta [49]. This finally leads to

$$\begin{aligned}\frac{\partial\omega^h}{\partial t} + \overline{U}_k\frac{\partial\omega^h}{\partial x_k} &= \frac{\partial}{\partial x_k}\left[\left(\frac{1}{2}\nu + \frac{\nu_t}{\sigma}\right)\frac{\partial\omega^h}{\partial x_k}\right] - C_{\omega,1}\frac{\omega^h}{k}P_k \\ &\quad - C_{\omega,2}\omega^h\omega^h + \frac{2}{k}\left(C_{cr,1}\frac{1}{2}\nu + C_{cr_2}\frac{\nu_t}{\sigma}\right)\frac{\partial\omega^h}{\partial x_k}\frac{\partial k}{\partial x_k} \\ &\quad + \frac{1}{k}P_{\omega,3}\end{aligned} \tag{3.35}$$

with $P_k = -\overline{u_i' u_k'} \partial \overline{U}_i / \partial x_k$ being the exact production of k and the gradient production term $P_{\omega,3}$. The previously adopted simplification through the SGDH prevented the origination of additional terms in Eq. (3.35). Jakirlić and Hanjalić [47] expressed $P_{\varepsilon,3}$ in their ε^h equation in terms of both mean rate of strain and the second derivative of the velocity field. While this approach leads to overall good agreement with reference DNS data for the plane channel flow, it is also a source of high numerical instability and questionable computational effort. Therefore Maduta [70] simplified the modeled $P_{\omega,3}$ in analogy to the model proposed by Launder and Sharma [60] in Eq. (3.26) towards

$$P_{\omega,3} = 2C_{\omega,3} \nu \nu_t \frac{\partial^2 \overline{U}_j}{\partial x_k \partial x_n} \frac{\partial^2 \overline{U}_j}{\partial x_k \partial x_n}. \tag{3.36}$$

The newly introduced fourth term on the right hand side of Eq. (3.35) is the cross derivative term, being a product of the derivation of Eq. (3.35) through Eq. (3.34). Therefore the modeling constants $C_{cr,1}$ and $C_{cr,2}$ had to be re-calibrated by Maduta [70]. The viscosity affected part of the term is adjusted by using the asymptotic near-wall behavior of ω^h, being approximated through the Taylor microscale wall boundary condition, introduced by Jakirlić and Jovanović [48]. This leads to

$$\omega^h_{\text{wall}} = \frac{\varepsilon^h_{\text{wall}}}{k} = \nu \frac{1}{y^2}. \tag{3.37}$$

Thus a boundary layer form of Eq. (3.35), considering only the viscous affected terms, could be derived. Finally this leads to a value of $C_{cr,1} = 0.55$. To calibrate $C_{cr,2}$ a mixing layer experiment by Spencer [99] was used by Maduta [70] (as suggested by Wilcox [111]), leading to $C_{cr,2} = 0.275$. Table 3.2 registers every coefficient in the present SMC model.

Table 3.2: Coefficients of the Jakirlić-Maduta RSM

$C_{\omega,1}$	$C_{\omega,2}$	$C_{\omega,3}$	σ	$C_{cr,1}$	$C_{cr,2}$
0.44	0.8	1.0	1.1	0.55	0.275

The whole model description can be found in Appendix A. This $\overline{u_i' u_j'} - \omega^h$ model has been intensively validated in numerous single-phase flow configurations by Maduta [70].

3.2.3 Eddy-resolving Reynolds-stress model

The classical steady state RANS models perform well for most test cases with wall bounded non-separating flows, while starting to be less reliable in cases where large separating zones or swirling effects are present, whereby an RSM is usually regarded to be able to handle these flow cases better than an EVM. But still, the RANS model framework seems to reach its rational limitation, which is somehow obvious, since an unsteady three-dimensional physical phenomenon such as a turbulent flow can only be described until a certain degree by a mostly steady state approach with $\partial\overline{\Phi}/\partial t = 0$ as it is the case for the RANS framework. LES, of course, could be an appropriate method for computing flow cases in which classical RANS models fail. But as previously mentioned in Chapter 3.1, LES is far beyond from being able to be used in industrially relevant test cases due to the vastly (increased) computational effort in comparison to the RANS models. Hence, a comprehensible step to improve the computation of turbulent flows is to bridge the gap between LES and RANS by combining the advantages of both methodologies, as e.g. discussed and reviewed by Spalart [98].

The first convenient approach thereby is the so-called unsteady RANS (URANS) framework, whereby classical (and steady) RANS models are applied without any structural changes. URANS is often regarded as the more rational approach for some globally unstable configurations, such as flows over bluff bodies (which always come along with large separating zones), than classical RANS computations. In such cases, the previously presented RANS equation system, with its particular turbulence model, is becoming unstable and thereby starting to resolve the low frequency (often called periodic) motions $\phi''(x_j, t)$ of the flow field. This behavior is more common for RSMs than for EVMs. As a direct consequence, the mean flow quantities $\overline{\Phi}(x_j, t)$ are becoming time dependent itself by containing these huge periodic motions $\phi''(x_j, t)$. The latter motions, however, do not contain any spectral content of the "real" turbulent fluctuating quantities $\phi'(x_j, t)$, which are still captured by the utilized RANS model. Therefore $\overline{\Phi}(x_j, t)$ is still a mean value, even if it is unsteady now. This behavior alters the classical decomposition in Eq. (3.4) towards

$$\Phi(x_j, t) = \overline{\Phi}(x_j, t) + \phi'(x_j, t) = \langle\Phi\rangle(x_j) + \phi''(x_j, t) + \phi'(x_j, t). \quad (3.38)$$

Such URANS simulations require an additional time averaging procedure denoted by <>, which is furthermore explained by Fig. 3.3.

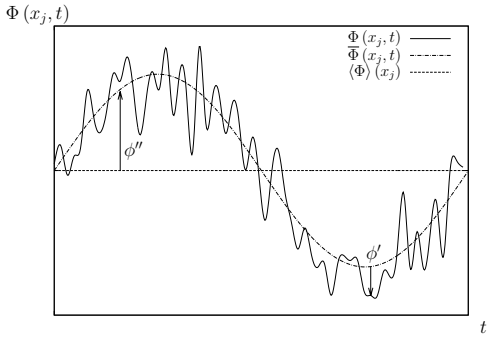

Figure 3.3: Decomposition for an URANS simulation

Therewith desired comparable statistical values $\langle\Phi\rangle(x_j)$ can be obtained. The time averaged sum of the fluctuating stresses $\langle u_i u_j\rangle$ are thereby stemming from a resolved $\langle u_i'' u_j''\rangle$ and a modeled $\left\langle\overline{u_i' u_j'}\right\rangle$ component, computed via

$$\langle u_i u_j\rangle = \langle u_i'' u_j''\rangle + \left\langle\overline{u_i' u_j'}\right\rangle = \langle(\overline{U}_j\overline{U}_i)\rangle - \langle\overline{U}_i\rangle\langle\overline{U}_j\rangle + \left\langle\overline{u_i' u_j'}\right\rangle. \quad (3.39)$$

It has to be stated that according to Leschziner [63] (among others), the URANS procedure does not guarantee that a well defined steady state RANS model, irrespective of being an EVM or an RSM, will lead to accurate results, when used in an unsteady computation. This uncertainty should be kept in mind.

As indicated by Fig. 3.1, the modeled part in URANS is much bigger than the resolved and under no circumstances nearly as small as in an LES. This has led many authors to the development of models, which are resolving more of the fluctuating turbulent spectra compared to URANS simulations, while on the other side modeling more than just the small dissipative scales, as it is the case for an SGS model in a conventional LES. Realizing this numerical coupling between these essentially different methodologies is one of the most discussed key points in the further development of the so-called hybrid RANS/LES framework. Several alternatives have been proposed so far, towards a method combining both advantages in terms of an adequate resolving of the turbulent structures and reduced computational costs in comparison to a standard LES. So if a RANS equation model is used as the

baseline modeling expression, an appropriate modification has to be developed, that reduces ϕ' (in comparison to URANS) and enables the "real" turbulent fluctuating motions to be directly included in $\overline{\Phi}(x_j, t)$. Within this respect, a review of the most common models can be found, among others, in Fröhlich and von Terzi [29] and a discussion about the physical aspects of the different methodologies in Spalart [98].

One of these methodologies is the scale-adaptive simulation (SAS) concept developed by Menter and Egorov ([76],[73],[75],[74]), with the main objective of an appropriate modification of the scale supplying equation within a classical RANS model. Its theoretical rationale is based on Rotta [87], who proposed a two-equation model, which consists of a k equation for providing the classical velocity scale and a novel one for kL as the length supplying equation, including an integral length scale of turbulence L. The latter equation is thereby not modeled in an analogy to the k equation, as it is usually done for an EVM, but in a term-by-term manner based on the two-point correlation method. The main distinguished feature of this kL equation, in comparison to other scale supplying equations, is the appearance of a second production term involving a length scale. Unfortunately the original proposed model by Rotta [87] for this term, involving the third derivative of the mean velocity, possessed some unfavorable features, like not being able to fulfill the logarithmic law, that made the use of this model inadequate in the past. Menter and Egorov resolved this problem by expressing this additional production term in the kL equation in terms of the second derivative of the mean velocity leading to

$$P_{kL,II} = -\tilde{\xi}_2 \frac{kL}{k} P_k \left(\frac{L}{L_{\mathrm{vK}}} \right)^2 . \tag{3.40}$$

The production P_k is thereby modeled according to Eq. (3.25) and a model constant $\tilde{\xi}_2$ is calibrated. The newly introduced von Kármán length scale L_{vK} contains the ratio between the first and second derivative of the mean velocity field

$$L_{\mathrm{vK}} = \kappa \frac{U'}{U''} \tag{3.41}$$

with the first derivative being specified as an invariant of the mean strain tensor S_{ij} (Eq. (3.7)) resulting in $U' = S = \sqrt{2 S_{ij} S_{ij}}$ and the second derivative being defined through

$$U'' = \sqrt{\frac{\partial^2 \overline{U}_i}{\partial x_k \partial x_k} \frac{\partial^2 \overline{U}_i}{\partial x_j \partial x_j}}. \tag{3.42}$$

L_{vK} is often referred to as being able of capturing the vortex size variability and thus enabling the development of the turbulent vortex structures. This is mainly due to the fact that L_{vK} decreases in an instantaneous velocity field in comparison to a time-averaged one (see Davidson [18] for further explanation), which results in an increased value of $P_{kL,II}$ in unstable areas such as separation zones. This leads to a decreased value of

$$\nu_t \propto \frac{kL}{\sqrt{k}} \tag{3.43}$$

since $P_{kL,II}$ acts as a second sink term. The development of turbulent structures can thereby be enabled, since the reduction of ν_t is responsible for the fact that this EVM loses its highly dissipative nature. In a next step Menter and Egorov [75] utilized this idea to extend the classical eddy-viscosity $k-\omega$ shear stress transport (SST) model by Menter [72], towards a "true" unsteady RANS model, denoting it as SST-SAS. A transformed version of $P_{kL,II}$ named P_{SAS} is added into the length-scale supplying ω-equation of the original SST model yielding

$$\left(\frac{D\omega}{Dt}\right)_{\text{SST-SAS}} = \left(\frac{D\omega}{Dt}\right)_{\text{SST}} + P_{\mathrm{SAS}} \tag{3.44}$$

with

$$P_{\mathrm{SAS}} = \max\left[\tilde{\xi}_2 S^2 \left(\frac{L_{\mathrm{SST}}}{L_{\mathrm{vK}}}\right)^2 - C_{\mathrm{SAS}}\frac{k}{\sigma_\Phi}\max\left(\frac{1}{\omega^2}\frac{\partial\omega}{\partial x_j}\frac{\partial\omega}{\partial x_j}, \frac{1}{k^2}\frac{\partial k}{\partial x_j}\frac{\partial k}{\partial x_j}\right), 0\right]. \tag{3.45}$$

This term contains two *max* functions. The outer one ensures that the terms stays always positive, guaranteeing the character of a production term. The inner one partly consists of derivatives due to the transformation from kL to ω and an additional k-derivative term added to preserve the performance of the classical SST model in boundary layer flows. The turbulent length scale from the SST model is hereby defined by

$$L_{\mathrm{SST}} = \frac{\sqrt{k}}{\omega C_\mu^{1/4}}. \tag{3.46}$$

With this newly formulated model, Egorov et al. [26] simulated various complex flows and showed the great potential of the SAS method.

This motivated Jakirlić and Maduta [49] and [70] to develop an appropriate version of P_{SAS} for extending the length-scale supplying ω^h-equation of their baseline RSM to enable the development of the turbulent vortex structures. In analogy to Eq. (3.44) this extension is derived through

$$\left(\frac{D\omega^h}{Dt}\right)_{\text{IS-RSM}} = \left(\frac{D\omega^h}{Dt}\right)_{\text{Eq.(3.35)}} + P^*_{\mathrm{SAS}} \tag{3.47}$$

to obtain the length-scale supplying equation of an instability-sensitized Reynolds-stress model (IS-RSM). The major modeling challenge thereby is to derive P^*_{SAS} in an appropriate modified form of $P_{kL,II}$, valid for working in an SMC model framework. To gain this term, Maduta [70] followed the transformation rule given by Davidson [18]

$$\frac{D\omega}{Dt} = \frac{3}{2}\frac{\sqrt{k}}{kL}\frac{Dk}{Dt} - \frac{k^{(3/2)}}{(kL)^2}\frac{DkL}{Dt} \tag{3.48}$$

to transform the kL equation from Menter and Egorov [76] into an equation for ω. This resulting equation, consists of terms having an equivalent in Eq. (3.35), for which Maduta [70] kept the modeling expressions presented in Chapter 3.2.2, and three newly introduced terms:

$$\frac{D\omega}{Dt} = \ ... \ + \frac{\omega}{k}P_k\tilde{\xi}_2\left(\frac{L_{\mathrm{SST}}}{L_{\mathrm{vK}}}\right)^n - 2.0\nu_t\frac{1}{\omega}\frac{\partial\omega}{\partial x_j}\frac{\partial\omega}{\partial x_j} - \frac{3}{2}\nu_t\frac{\omega}{k^2}\frac{\partial k}{\partial x_j}\frac{\partial k}{\partial x_j}. \tag{3.49}$$

The production term P_k is thereby expressed in the classical EVM expression, $P_k = \nu_t S^2$, rather than the available exact form, to stay close to the original proposed SST-SAS model, with $\nu_t = C_\mu k/\omega$. The exponent n in Eq. (3.49), in the original SST-SAS model set to two, is here set to 1/2, to prevent a high overshoot leading to a complete destruction of the modeled quantities. The value 1/2 also flattens the effect of P^*_{SAS}, since the term is increased in areas with length scale ratios smaller than one, while being reduced in areas with length scale ratios larger then one. This finally leads to the reformulated version of P^*_{SAS}, with keeping the *max* functions and replacing ω by ω^h, adjusted appropriately to the underlying RSM:

$$P^*_{\mathrm{SAS}} = \ C_{\mathrm{RSM},1}\max\left[2.3713\kappa S^2\left(\frac{L_{\mathrm{SST}}}{L_{\mathrm{vK}}}\right)^{\frac{1}{2}} - C_{\mathrm{RSM},2}T_2, 0\right], \tag{3.50}$$

$$T_2 = \ 3k\max\left(\frac{1}{\omega^h\omega^h}\frac{\partial\omega^h}{\partial x_j}\frac{\partial\omega^h}{\partial x_j}, \frac{1}{k^2}\frac{\partial k}{\partial x_j}\frac{\partial k}{\partial x_j}\right) \tag{3.51}$$

The coefficient values have been determined by a series of model validations, see Jakirlić and Maduta [49], yielding to $C_{\mathrm{RSM},1} = 0.004$ and $C_{\mathrm{RSM},2} = 8$.

Compared to the SST-SAS model, the IS-RSM showed the potential to resolve turbulent structures even for globally stable flow configurations like pipe flows, without using any artificially imposed turbulent fluctuations. Another main distinguishing feature of the IS-RSM is the fact, that the production term in the transport equation for the Reynolds-stress tensor is exact for RANS as well as for a scale-resolving method like LES. In contrast to this P_k in the k-equation of the SST-SAS model is expressed in a typical EVM formulation.

Recently Maduta et al. [71] proposed an improved version of the previously described IS-RSM in terms of enhanced numerical robustness. The original proposed model exhibits strong numerical instabilities, especially when using high order numerical schemes, through the large number of strongly coupled transport equations of the baseline RSM. Another problematic aspect of an SMC model is the coupling between the mean momentum and turbulent equations, hence the numerical treatment of the Reynolds-stress tensor in Eq. (3.5). An EVM does not exhibit this problem since $\overline{u_i'u_j'}$ is modeled through Eq. (3.8) and can therefore be mainly included into the diffusion term. A discussion about the problematic coupling between the momentum equation and the Reynolds-stress tensor can be found in Basara [5]. Maduta et al. [71] proposed to use a blending mechanism between a direct inclusion of $\overline{u_i'u_j'}$ into Eq. (3.5) and a certain amount of $\overline{u_i'u_j'}$ including via Eq. (3.8) resulting in

$$\overline{u_i'u_j'} = 0.8 * \underbrace{\overline{u_i'u_j'}}_{\text{RSM}} - 0.2 * \underbrace{\left[\nu_t \left(\frac{\partial \overline{U}_i}{\partial x_j} + \frac{\partial \overline{U}_j}{\partial x_i}\right) - \frac{2}{3} k \delta_{ij}\right]}_{\text{EVM}}. \tag{3.52}$$

In this work a blending of 80% stemming directly from $\overline{u_i'u_j'}$ and 20% from the eddy-viscosity assumption are chosen, with ν_t being defined through Eq. (3.28). By using this numerical stabilization the newly formulated sensitized model is named improved IS-RSM (IIS-RSM). This modification is only applied to the eddy-resolving mode of the present RSM, whereby the modeled turbulent quantities, such as $\overline{u_i'u_j'}$ and k, are significantly reduced, through partly resolving the fluctuating velocity field. Therefore the resulting impact of Eq. (3.52) on the statistically averaged quantities is supposed to be negligible, since the modification only prevents the model from becoming numerically unstable during the time dependent calculations. This modification is not adopted for the baseline RSM operating in a classical RANS sense. The whole model description can be found in Appendix B.

4 The two-fluid model framework for two-phase flow computations

The two-fluid model (TFM), or Euler-Euler model, represent the theoretical framework for the investigated two-phase flows in this study. In the TFM each phase is considered as a continuous medium represented by a set of macroscopic averaged conservation equations defined in an Eulerian description. These equations are valid in the whole flow domain, with both phases interpenetrating each other. Many authors, like Ishii and Hibiki [44] and Kataoka and Serizawa [54], have derived the respective equation system. The vast majority of these authors utilize a conditional averaging technique which introduces an indicator function

$$I_\psi(x_i,t) = \begin{cases} 1, & \text{if phase } \psi \text{ present at } (x_i,t) \\ 0, & \text{otherwise} \end{cases} \tag{4.1}$$

with ψ denoting the respective phase. In the present work, the selection of the phases is restricted to a gas phase $\psi \equiv \mathrm{G}$ and a liquid phase $\psi \equiv \mathrm{L}$. The local instantaneous conservation equations for each phase, Eqs. (3.1) and (3.2), are then multiplied by I_ψ and averaged to obtain the desired equations. By using this conditional averaging technique, it is ensured that the impact of one particular phase only acts in regions which contain this phase. The definition of the averaging operator is a widely discussed topic. While authors like Ishii and Hibiki [44] proposed a time averaging, other authors like Kataoka and Serizawa [54] suggested an ensemble averaging technique. The latter one was also used by Hill [38] and Rusche [88] and since it is the most general definition of an averaging operator it is adopted here. Nevertheless, all of these procedures lead to the same equation system, only differing in the meaning of the averaged quantities. One important variable in the two-fluid model equations is the phase fraction of phase ψ which is defined by

$$\alpha_\psi = \overline{I_\psi(x_i,t)} \tag{4.2}$$

with $\Sigma\alpha_\psi = 1$. It can be interpreted as the probability that phase ψ is present at a certain point in space and time. Analogue to the decomposition applied for single-phase turbulent flows, by using the Reynolds

decomposition Eq. (3.4), the conditionally weighted decomposition leads to

$$\Phi = \overline{\Phi}^{\psi} + \phi'^{\psi} \tag{4.3}$$

with the conditional-averaged flow quantity defined as

$$\overline{\Phi}^{\psi} = \frac{\overline{I_{\psi}\Phi}}{\overline{I_{\psi}}} = \frac{\overline{I_{\psi}\Phi}}{\alpha_{\psi}} \tag{4.4}$$

and a fluctuating part ϕ'^{ψ}. A density weighting is not required, since all phases considered here are regarded as incompressible. As mentioned before, slightly different versions of the resulting two-fluid model exist in the literature. Here the following form, see Rusche [88] or Hosokawa and Tomiyama [40], is used for an adiabatic flow without phase change and both phases are regarded as incompressible. The continuity equation is given by

$$\frac{\partial \alpha_{\psi}}{\partial t} + \frac{\partial \overline{U}_j^{\psi} \alpha_{\psi}}{\partial x_j} = 0 \tag{4.5}$$

and the momentum equation by

$$\begin{aligned} &\frac{\partial(\alpha_{\psi}\overline{U}_i^{\psi})}{\partial t} + \frac{\partial(\alpha_{\psi}\overline{U}_j^{\psi}\overline{U}_i^{\psi})}{\partial x_j} = -\frac{\alpha_{\psi}}{\rho_{\psi}}\frac{\partial \overline{P}}{\partial x_i} + \alpha_{\psi} g_i \\ &+ \frac{\partial}{\partial x_j}\left[\alpha_{\psi}\nu_{\psi}\left(\frac{\partial \overline{U}_i^{\psi}}{\partial x_j} + \frac{\partial \overline{U}_j^{\psi}}{\partial x_i}\right)\right] + \frac{M_i^{\psi}}{\rho_{\psi}} - \frac{\partial \alpha_{\psi}\overline{u_i'^{\psi}u_j'^{\psi}}^{\psi}}{\partial x_j}. \end{aligned} \tag{4.6}$$

The conditionally averaged velocity, viscosity, density and gravitational vector are denoted by $\overline{U}_i^{\psi}$, ν_{ψ}, ρ_{ψ} and g_i, respectively. Therefore, the two-fluid model persists of a consecutive set of transport equations for both phases valid in the whole flow domain, irrespective of the presence of the phase at any point in the flow field. In the here utilized form of the two-fluid model, the pressure $\overline{P}$ is commonly supposed to be shared by both phases. Throughout the averaging procedure, the two-fluid model in general loses the ability to resolve the interfacial structures between the participating phases. Thus, additional unclosed terms are necessarily introduced in the momentum equations due to the loss of information about the instantaneous local flow conditions. These unclosed terms are the interfacial momentum transfer term M_i^{ψ} and the Reynolds-stress tensor $\overline{u_i'^{\psi}u_j'^{\psi}}^{\psi}$ considering the effect of the turbulent fluctuating motions in both phases. The utilized closure models for these terms are separately presented below, including a brief introduction into the main modeling challenges.

4.1 Modeling of the interfacial momentum transfer

The interfacial momentum transfer term M_i^{ψ} describes the constitutive relations between the present phases, hence the total force acting from the continuous phase on the dispersed phase and vice versa. The major modeling challenge thereby is due to the fact that a generally applicable modeling strategy regardless of the flow type or regime does not exist so far. This is because of the unlimited number of possible flow regimes such as slug flows, separated flows or dispersed flows and the variety of possible material combinations between the involved phases, such as gas-liquid, liquid-liquid and solid-liquid. In this study only gas-liquid flows are considered and furthermore it is assumed that the gas phase is in general the finely dispersed phase and the liquid phase the continuous one, reducing the number of possible applicable models for M_i^{ψ}. The total interfacial momentum transfer is usually decomposed into several components with various combinations, which should account for different physical interactions between both phases, see e.g. Ishii and Hibiki [44]. These interfacial force models encountered here are the most popular ones for describing dispersed bubbly flows and compromise the drag force $M_{\mathrm{d},i}^{\mathrm{L}}$, the lift force $M_{\mathrm{l},i}^{\mathrm{L}}$, the virtual mass force $M_{\mathrm{vm},i}^{\mathrm{L}}$ and the turbulent dispersion force $M_{\mathrm{td},i}^{\mathrm{L}}$. Hence M_i^{ψ} is decomposed into

$$M_i^{\mathrm{L}} = -M_i^{\mathrm{G}} = M_{\mathrm{d},i}^{\mathrm{L}} + M_{\mathrm{l},i}^{\mathrm{L}} + M_{\mathrm{vm},i}^{\mathrm{L}} + M_{\mathrm{td},i}^{\mathrm{L}} \tag{4.7}$$

whereby the total interfacial momentum transfer term vanishes $\Sigma M_i^{\psi} = 0$, implying that $M_i^{\mathrm{L}} = -M_i^{\mathrm{G}}$. Including M_i^{ψ} in both momentum equations is also known as two-way coupling. Finding appropriate models for these forces has been and still is one of the key-issues in the further development of the two-fluid model. A review and a detailed introduction into the modeling of the drag and lift force can be found in Rusche [88] and Hibiki and Ishii [37] showing the vast variety of possible modeling expressions. All models for M_i^{ψ} used in this work can be found in the available literature and should be valid for finely dispersed bubbly flows in clean water. Another popular model is the wall lubrication force based on the work of Antal et al. [2] which is supposed to be responsible for pushing the dispersed bubbles away from the wall. Since this force model is originally developed for laminar flows, its validity for turbulent flows is highly questionable and considerably more complex to implement than the other employed forces. Thus it is neglected here. The diameter of the gas phase d_{G}, hence the

size of the bubble, in each case is considered as a constant, following a monodispersed approach here. If not stated otherwise, the gas phase G is equivalent to the dispersed phase. The particular models for Eq. (4.7) are presented below.

Drag force

The relative motion between a moving body and the surrounding fluid results in a force acting against that motion and is called drag force. This force is regarded as the most important interfacial force, see e.g. Ishii and Hibiki [44], since it is responsible for the distribution of the relative velocity between both phases and is considered in all flow configurations. Its standard formulation within the two-fluid model is given by

$$M_{\mathrm{d},i}^{\mathrm{L}} = C_{\mathrm{d}} \frac{3}{4} \alpha_{\mathrm{G}} \frac{\rho_{\mathrm{L}}}{d_{\mathrm{G}}} \sqrt{\overline{U}_k^r \overline{U}_k^r}\, \overline{U}_i^r \tag{4.8}$$

with the dimensionless drag coefficient C_{d} and the relative velocity $\overline{U}_i^r = \overline{U}_i^{\mathrm{G}} - \overline{U}_i^{\mathrm{L}}$ between the phases. C_{d} is thereby computed through empirical correlations, based on experimental data sets and DNS investigations. A diversity of possible models for C_{d} can be found in the literature, depending on the flow regime, the material properties of the present phases and the values of α_{G}. Two important typical dimensionless modeling parameters are the bubble Reynolds number

$$Re_{\mathrm{B}} = \frac{\sqrt{\overline{U}_k^r \overline{U}_k^r}\, d_{\mathrm{G}}}{\nu_{\mathrm{L}}} \tag{4.9}$$

and the dimensionless Eötvös number

$$Eo = \frac{g(\rho_{\mathrm{L}} - \rho_{\mathrm{G}}) d_{\mathrm{G}}^2}{\sigma_{\mathrm{GL}}} \tag{4.10}$$

with σ_{GL} being the surface tension between dispersed and continuous phase and g the magnitude of the gravitational vector. Tomiyama et al. [103] used these dimensionless quantities to develop an empirical expression being valid over a wide range of flow types and thereby combining several previously proposed correlations, including the one proposed by Schiller-Naumann [93], into

$$C_{\mathrm{d}} = \max\left[\min\left(\frac{16}{Re_{\mathrm{B}}}(1 + Re_{\mathrm{B}}^{0.687}), \frac{48}{Re_{\mathrm{B}}}\right), \frac{8}{3}\frac{Eo}{Eo+4}\right]. \tag{4.11}$$

The advantage of this correlation is its easy implementation and stable behavior over a wide range of possible flow configurations and is therefore utilized in this work. The correlations for C_d are usually determined for a single bubble in a continuous medium, hence for a low value of α_G in the two-fluid model framework. However, if α_G increases, the presence of these higher values has an influence on C_d. This phenomenon is known as the swarm effect. A lot of possible modifications of C_d have been proposed so far, which should be able to fall back into the description for C_d if the phase fraction becomes small. One correlation accounting for swarm effects is the one proposed by Tomiyama et al. [102], which is defined through

$$\frac{C_\mathrm{dS}}{C_\mathrm{d}} = \alpha_\mathrm{L}^{-0.5} \tag{4.12}$$

with C_dS denoting the consideration of a swarm effect. This simply introduces a factor depending on the phase fraction of the continuous phase into the correlation and is one of the easiest models to account for swarm effects. A more complex correlation and an extension to Eq. (4.12), taking into account the presence of a liquid velocity gradient to increase the drag force acting on the dispersed bubble, is the one developed by Legendre and Magnaudet [62]

$$\frac{C_\mathrm{dS}}{C_\mathrm{d}} = (1 + 0.55Sr^2) \cdot \alpha_\mathrm{L}^{-0.5}. \tag{4.13}$$

In the above expression, the non dimensional shear rate Sr is expressed through

$$Sr = \frac{Sd_\mathrm{G}}{\sqrt{\overline{U}_k^r \overline{U}_k^r}} \tag{4.14}$$

with taking into account the magnitude of the liquid velocity gradient S. This correlation was originally developed for a simple shear flow by Legendre and Magnaudet [62], whereby the definition of S is obvious. A valid definition for S in turbulent flows does not exist in general. Therefore the same definition for S as it is used in Chapter 3.2.3 for the von Kármán length scale is utilized. This is done by defining S_{ij} in terms of the velocity of the liquid phase $\overline{U}_i^\mathrm{L}$. The correlation by Legendre and Magnaudet [62] is used here if the consideration of a swarm effect on the drag force is necessary. Through the presence of the liquid velocity gradient within Eq. (4.13), this is not only regarded as a swarm correlation, but also as a low Reynolds number correction in the areas close to a solid wall.

Lift force

The lift force is regarded as the most important force which acts in the lateral direction of the dispersed gas phase movement. It is held mainly responsible for the radial distribution of α_{G} in flow configuration such as bubbly pipe flows. Several expressions for the lift force can be found in the literature, the most common one thereby is defined by Auton [3] who proposed to model the lift force through

$$M_{\mathrm{l},i}^{\mathrm{L}} = \alpha_{\mathrm{G}} C_{\mathrm{l}} \rho_{\mathrm{L}} \epsilon_{imj} \overline{U}^{r}_{m} \epsilon_{jnk} \frac{\partial \overline{U}_{k}^{\mathrm{L}}}{\partial x_n} \tag{4.15}$$

with C_{l} being the dimensionless lift force coefficient. The determination of C_{l} is still an open field of research, combining analytic, numerical and experimental investigations. Hibiki and Ishii [37] showed in an extensive literature research the wide range of proposed models for C_{l}, their respective influencing factors and major assumptions. Thereby, it is obvious that a common correlation being generally valid for the generic test cases investigated here does not exist. Even worse, the usage of most correlations describing C_{l} is highly questionable since the majority of these correlations is derived for simple laminar shear flows and not for turbulent flows, which are of course more relevant since turbulent flows occur in nearly all industrially relevant test cases. However since there is a lack of reliable correlations for turbulent flows, the correlations summarized in Hibiki and Ishii [37] are the only available ones. The simplest choice for C_{l} is to choose a fixed value, whereby a huge range of proposed and utilized values can be found in the literature. The most often referred value is $C_{\mathrm{l}} = 0.5$ as it was proposed by Auton [3] for a spherical bubble placed in a weak shear flow of an inviscid fluid. Lower values can be found for the usage within a turbulent flow, like $C_{\mathrm{l}} = 0.25$ by Hill [38]. Bertodano et al. used different values, $C_{\mathrm{l}} = 0.05$ in [66] and $C_{\mathrm{l}} = 0.1$ in [65] for matching their computed α_{G}-distribution with the respective experimental reference data. Clearly one demand for a suitable lift force model would be a correlation that can provide such an adjusted value by itself. This would also include the consideration of swarm effects on C_{l}, for which the available modeling principles are very rare according to Rusche [88]. Nevertheless, different fixed values for C_{l} are adopted here, to obtain the desired distributions of α_{G} in an acceptable agreement with the experimental reference data. Because of the present liquid velocity gradient in Eq. (4.15) severe numerical difficulties can be expected in the near wall areas where this value reaches its maximum. To guarantee numerical stability, an exponential blending function

$e^{-1/\Gamma}$ originally proposed for a wall compound treatment by Popovac and Hanjalić [83] is utilized. This function is configured to switch of the lift force in areas with $y^+ < 1$. The lift force is actually supposed to tend towards zero in this area anyway because of the vanishing relative velocities in the vicinity of the wall.

Virtual mass force

The virtual mass force is modeled as

$$M^{\mathrm{L}}_{\mathrm{vm},i} = \alpha_{\mathrm{G}} C_{\mathrm{vm}} \rho_{\mathrm{L}} \left(\frac{D\overline{U}^{\mathrm{L}}_i}{Dt} - \frac{D\overline{U}^{\mathrm{G}}_i}{Dt} \right) \tag{4.16}$$

with the coefficient C_{vm} taking the value of 0.5, which has also been used by Zhang et al. [114]. The substantial derivative D/Dt relates to the respective phase ψ.

Turbulent dispersion force

The turbulent dispersion force is another frequently employed interfacial force which mainly acts in the lateral direction of the dispersed bubble movement. According to Ishii and Hibiki [44] this force stems from the turbulent fluctuations within the continuous liquid phase. Many different forms of this force can be found in the respective literature. Among these, the form proposed by Lahey et al. [58] which reads

$$M^{\mathrm{L}}_{\mathrm{td},i} = C_{\mathrm{td}} \rho_{\mathrm{L}} k^{\mathrm{L}} \frac{\partial \alpha_{\mathrm{G}}}{\partial x_i} \tag{4.17}$$

is the simplest possible expression with a dimensionless coefficient C_{td} introduced in order to calibrate the model. This expression includes the turbulent kinetic energy of the continuous liquid phase k^{L}. According to Lahey and Drew [57] a wide range of suggested and utilized fixed values for C_{td}, which usually ranges between 0.1 and 1.0, can be found in the literature, without one claiming to be valid in general. A more complex possibility for expressing C_{td} and hence presumably valid over a broader range of flow configurations is to define the coefficient depending on the local mean flow properties as it was done for example by Burns [12]. Since such complex correlations do not necessarily lead to higher valuable results, fixed values for C_{td} are used here for simplicity reasons.

Closure summary

Summarizing the previously described modeling strategy, the interfacial momentum transfer term can be summed up via

$$
\begin{aligned}
M_i^{\mathrm{L}} &= \underbrace{\alpha_{\mathrm{G}} \frac{3}{4} C_{\mathrm{dS}} \frac{\rho_{\mathrm{L}}}{d_{\mathrm{G}}} \sqrt{\overline{U}_k^r \overline{U}_k^r}\, \overline{U}_i^r}_{M_{\mathrm{d},i}^{\mathrm{L}}} \\
&+ \underbrace{\alpha_{\mathrm{G}} C_{\mathrm{l}} \rho_{\mathrm{L}} \left(\epsilon_{ijk} \epsilon_{kmn} \overline{U}_j^r \frac{\partial \overline{U}_n^{\mathrm{L}}}{\partial x_m} \right)}_{M_{\mathrm{l},i}^{\mathrm{L}}} \\
&+ \underbrace{\alpha_{\mathrm{G}} C_{\mathrm{vm}} \rho_{\mathrm{L}} \left(\frac{D\overline{U}_i^{\mathrm{L}}}{Dt} - \frac{D\overline{U}_i^{\mathrm{G}}}{Dt} \right)}_{M_{\mathrm{vm},i}^{\mathrm{L}}} \\
&+ \underbrace{C_{\mathrm{td}} \rho_{\mathrm{L}} k^{\mathrm{L}} \frac{\partial \alpha_{\mathrm{G}}}{\partial x_i}}_{M_{\mathrm{td},i}^{\mathrm{L}}} . \qquad (4.18)
\end{aligned}
$$

This formulation leads to physical and numerical problems in cases where phase inversions, meaning that the originally dispersed phase becomes the continuous phase, or phase separations occur, since Eq. (4.18) assumes that the gas phase is the dispersed phase. Weller [108] proposed a simple model to extend Eq. (4.18) towards a formulation of the interfacial momentum transfer term which is valid over the full range of possible phase fraction values. The underlying idea thereby is to formulate a complete expression as it is described via Eq. (4.18) for the case of a continuous liquid phase ($\psi = \mathrm{L}$) and a dispersed gas phase ($\psi = \mathrm{G}$) and combine these expressions together into a single one. This is accomplished with the introduction of appropriate blending functions f_{G} and $f_{\mathrm{L}} = 1 - f_{\mathrm{G}}$ which should ensure a smooth transition between both expressions. This closure strategy was

also used by Rusche [88] and leads to

$$
\begin{aligned}
M_i^{\mathrm{L}} \quad = \quad & \underbrace{\alpha_{\mathrm{G}}\alpha_{\mathrm{L}}\ \frac{3}{4}\ \left(f_{\mathrm{G}}C_{\mathrm{dS,G}}\frac{\rho_{\mathrm{L}}}{d_{\mathrm{G}}} + f_{\mathrm{L}}C_{\mathrm{d,L}}\frac{\rho_{\mathrm{G}}}{d_{\mathrm{L}}}\right)\ \sqrt{\overline{U}_k^r\overline{U}_k^r}\ \overline{U}_i^r}_{M_{\mathrm{d},i}^{\mathrm{L}}} \\
& + \underbrace{\alpha_{\mathrm{G}}\alpha_{\mathrm{L}}\ f_{\mathrm{G}}C_{\mathrm{l,G}}\rho_{\mathrm{L}}\left(\epsilon_{ijk}\epsilon_{kmn}\overline{U}_j^r\frac{\partial\overline{U}_n^{\mathrm{L}}}{\partial x_m}\right)}_{M_{\mathrm{l},i}^{\mathrm{L}}} \\
& + \underbrace{\alpha_{\mathrm{G}}\alpha_{\mathrm{L}}\ f_{\mathrm{L}}C_{\mathrm{l,L}}\rho_{\mathrm{G}}\left(\epsilon_{ijk}\epsilon_{kmn}\overline{U}_j^r\frac{\partial\overline{U}_n^{\mathrm{G}}}{\partial x_m}\right)}_{M_{\mathrm{l},i}^{\mathrm{L}}} \\
& + \underbrace{\alpha_{\mathrm{G}}\alpha_{\mathrm{L}}\ \left(f_{\mathrm{G}}C_{\mathrm{vm,G}}\ \rho_{\mathrm{L}} + f_{\mathrm{L}}C_{\mathrm{vm,L}}\ \rho_{\mathrm{G}}\right)\ \left(\frac{D\overline{U}_i^{\mathrm{L}}}{Dt} - \frac{D\overline{U}_i^{\mathrm{G}}}{Dt}\right)}_{M_{\mathrm{vm},i}^{\mathrm{L}}}.
\end{aligned}
\tag{4.19}
$$

Here the blending functions are simply expressed by $f_{\mathrm{G}} = \alpha_{\mathrm{L}}$ and $f_{\mathrm{L}} = \alpha_{\mathrm{G}}$. The dimensionless coefficients in Eq. (4.19) possess a second subscript which indicates the particular dispersed phase used to express the coefficient. In cases where phase separation occurs, the turbulent dispersion force has to be neglected, since Eq. (4.17) is proportional to the phase fraction gradient. This can cause severe numerical instabilities, when being applied in flows with free surfaces, since the volume fraction suddenly changes from 0 to 1 or vice versa. Hence this force cannot be incorporated when using Eq. (4.19). Eq. (4.18) respectively Eq. (4.19) concludes the modeling of the interfacial momentum transfer and the next chapter focuses on the remaining unclosed Reynolds-stress tensor $\overline{u_i'^{\psi}u_j'^{\psi}}^{\psi}$.

4.2 Turbulence modeling in the two-fluid model

The modeling of turbulence in a two-phase flow represents a widely open and actual subject within the field of CFD. Thus before explaining in detail the current modeling strategy for $\overline{u_i'^{\psi} u_j'^{\psi}}^{\psi}$ in Eq. (4.6), an introduction to the present scientific challenges is given. Most of these difficulties stem from the fact that a two-phase flow can appear in several forms in terms of flow regime, the present fluids and the flow conditions such as the different velocities of both phases or different bubble sizes which all affect the resulting turbulent motions. An attempt to find a suitable description also depends on the utilized model for describing the two-phase flow. Hence the available models are formulated differently for VOF or the TFM. The following attempts are of course focused on the latter one. In the case of liquid-gas flows, the main focus lies on the turbulent fluctuations in the continuous liquid phase, while the ones in the dispersed gas-phase are usually neglected. A possible starting point for analyzing the turbulence in such a multiphase flow is the attempt of deriving exact transport equation for the turbulent quantities within the continuous liquid phase, which are mainly k^{L}, $\overline{u_i'^{\mathrm{L}} u_j'^{\mathrm{L}}}^{\mathrm{L}}$ and ε^{L}. Such an approach follows a similar path to the derivation of the unclosed RANS equations described in Chapter 3.1 for incompressible single-phase flows. In the TFM this is combined with a conditional averaging technique analogue to the one used for the derivation of the continuity and momentum equations presented before. The derivation of these exact transport equations has been done by several authors in the past such as Hill [38], Katoaka et al.([53] and [54]) and Alabejgovic et al. [1]. The resulting terms in these equations originate from two different physical sources and are usually classified as single-phase flow turbulence (sometimes shear induced turbulence) and bubble-induced turbulence (or pseudo turbulence).

Thereby are the single-phase flow turbulence terms characterized by a direct equivalent in the unclosed transport equations for the turbulent quantities in incompressible single-phase flows, such as the ones in Eq. (3.16), and are related to the turbulence that arises from the deformation of the mean velocities, which is the only source of turbulence in a single-phase flow. These unclosed terms are usually including α_{L}. The second group of terms are the ones having no similar counterpart in the corresponding single-phase flow equations and are supposed to be directly related to the presence of the dispersed gas phase. According to Kataoka et al. [53] they originate from

the surface tension and the drag force between the involved phases. They can cause an additional production or dissipation of turbulence and are unfortunately also unclosed. These terms are usually called interfacial terms and the generated turbulence is called bubble-induced turbulence (BIT) and has to be modeled by appropriate closure models. Lately Hosokawa and Tomiyama [42] showed that this bubble-induced turbulence can even turn an original single-phase laminar pipe flow into a turbulent one. The crucial point thereby is that the resulting turbulence is not just a simple sum of both physical sources, see Kataoka and Serizawa [54], instead it is characterized by complex physical phenomena, which are far beyond from being completely understood at the moment.

Another challenge arises from the fact that the set of unclosed transport equations derived by the previously referred authors differ substantially as it is stated by Hill [38]. For the transport equations for k^{L} and $\overline{u_i'^{\mathrm{L}} u_j'^{\mathrm{L}}}^{\mathrm{L}}$ these differences occur for the interfacial source terms regarding the direct influence of the dispersed phase on the turbulence of the liquid phase. This clearly complicates the development of reliable models for describing the bubble-induced turbulence, since it is unclear which of the proposed unclosed equations can be used as a starting point for a further term-by-term modeling. The source of these differences could originate from different definitions of certain flow quantities, which are here and there not rigorously defined. Additional to this challenge, the derived equations for ε^{L} differ considerably, regarding not only the interfacial source terms, but also in number and form of the appearing unclosed single-phase like terms. Hill [38] noted that it is not possible to even limit the differences since the given information about the derivation is insufficiently documented and therefore he derived his own equation for ε^{L}, which then differs again from the already existing ones.

Assuming that a consistent form of the exact transport equations can finally be established, the necessary modeling of the unclosed terms represents an enormous challenge, which can be classified into two different main aspects. The first one is the required modified modeling of the single-phase like terms since the presence of the second phase influences the physical behavior of those and has to be captured by an appropriate modified closure model. A good example for this is the very popular bubble-induced viscosity model by Sato et al. [91], who proposed an additional contribution to the turbulent viscosity due to the presence of the dispersed phase.

This model has been used by several authors like Rzehak and Krepper [89] or Hosokawa and Tomiyama [40] to compute various different two-phase flow applications. Another would be the appreciable experimental investigation done by Lance et al. [59], which led to a modified model of the redistribution term Φ_{ij} in the transport equation of $\overline{u_i'^{\mathrm{L}} u_j'^{\mathrm{L}}}^{\mathrm{L}}$. A review of such models can be found in Ilić [43]. A major problem thereby arises from the fact that these modifications can depend on several influencing factors being present in a two-phase flow, such as the value of α_{G}, the size of d_{G} or the relative velocity between both phases. These factors can all lead to variations of the basic physical behavior known from single-phase flows. A more detailed insight into these processes could be gained by DNS. One important work in this direction was done by Ilić [43] whereby uprising gas bubbles in a half infinite channel were investigated to perform a term-by-term analysis of the transport equation of the turbulent kinetic energy of the liquid phase k^{L}. Such investigations could lead to a more physically reasoned term-by-term modification of the present turbulence models for two-phase flows. All these modifications should fulfill the requirement that the utilized models have to fall back into the formulation for incompressible single-phase turbulent flows if the dispersed gas phase is not present.

The other main aspect in the field of two-phase flow turbulence focuses on the development of appropriate BIT models for describing the interfacial source terms in the turbulent transport equations. This has been done by several authors like Troshko and Hassan [105], Rzehak and Krepper [89], Politano et al. [81] and Pfleger and Becker [80]. All these authors used similar expressions for modeling the source term in the transport equation for k^{L}, differing only in the usage of a scaling factor. Additional to that, these authors developed several models for the source terms in the ε^{L} respectively ω^{L} equation, which substantially differ in the way a bubble influenced time-scale is defined. A majority of those were reviewed by Ilić [43] and tested term-by-term against a database obtained with DNS, whereby most of the above mentioned models were not capable to reproduce the behavior of the original unclosed interfacial source terms in an acceptable manner. Nevertheless these type of models represent the state of the art modeling approach for capturing the presence of the dispersed gas phase and its influence on the turbulence in the continuous liquid phase.

Caused by all these circumstances, the standard approach for modeling the turbulence in the continuous liquid phase typically consists of the uti-

lization of a high Reynolds number EVM, most often the standard $k-\varepsilon$ model, combined with a BIT model. Thereby the original Boussinesq hypothesis [11], see Eq. (3.8), is modified for expressing the Reynolds-stress tensor of the continuous liquid phase by

$$\overline{u_i'^{\mathrm{L}} u_j'^{\mathrm{L}}}^{\mathrm{L}} = -\nu_t \left(\frac{\partial \overline{U}_i^{\mathrm{L}}}{\partial x_j} + \frac{\partial \overline{U}_j^{\mathrm{L}}}{\partial x_i} \right) + \frac{2}{3} k^{\mathrm{L}} \delta_{ij}. \tag{4.20}$$

Accordingly, the use of this correlation in a two-phase flow is linked with some uncertainties, since it is unclear how the presence of the dispersed gas phase changes the validity of Eq. (4.20). A more rational approach would be, as it is in single-phase flows, the utilization of an SMC model and avoiding the use of Eq. (4.20). This has not become a standard approach so far, but nevertheless it has been done by a few authors, like Cokljat et al. [15], Lopez de Bertodano et al. [66], Chahed et al. [14] and Colombo and Fairweather [16]. Both approaches are followed here, to analyze the performance and the differences between these two classical RANS modeling strategies. The specific RANS models therefore are the Reynolds-stress model by Jakirlić and Maduta and the eddy-viscosity model by Launder-Sharma, which are both appropriately adjusted for the usage within the TFM. Both models are also extended by two different BIT models, which are on the one hand the model by Troshko and Hassan [105] and on the other the model by Rzehak and Krepper [89]. A completely novel approach for expressing $\overline{u_i'^{\mathrm{L}} u_j'^{\mathrm{L}}}^{\mathrm{L}}$ is the application of the IS-RSM respectively the IIS-RSM. The turbulence models and the utilized BIT models are in detail explained below.

4.2.1 Baseline turbulence models

The here utilized turbulence models within the TFM are directly modified from their original proposed form presented in Chapter 3. While these models represent a state of the art modeling approach in incompressible single-phase flows, all of them represent an enhancement for the present two-phase flow computations in comparison to the previously discussed standard approach. This is mainly caused by the fact that these models are indeed low Reynolds number models. The RSM by Jakirlić and Maduta has not been used in two-phase flow computations so far. Its application

represents a much more detailed approach for computing $\overline{u_i'^{\mathrm{L}} u_j'^{\mathrm{L}}}^{\mathrm{L}}$ and ω^{L} as in any other known investigation with SMC models in the TFM framework.

The single-phase like terms in the present models are only modified by incorporating α_{L}, while a direct term-by-term modification is omitted, which is mainly justified with the previously mentioned weak modeling database. One important modification is captured by the altered liquid velocity gradient between single- and two-phase flows, which is caused by the drag force due to its influence on the velocity distribution. As a consequence of this, the production terms are changed by the presence of the dispersed phase. Fortunately, the main production term in an RSM is still exact. These modifications also fulfill the requirement that the two-phase flow equations fall back to the single-phase one, if the dispersed phase is not present. From now on the superscript at the turbulent quantities indicating the liquid phase are omitted for readability reasons, hence $\overline{u_i'^{\mathrm{L}} u_j'^{\mathrm{L}}}^{\mathrm{L}} = \overline{u_i' u_j'}$, $k^{\mathrm{L}} = \overline{u_i'^{\mathrm{L}} u_i'^{\mathrm{L}}}^{\mathrm{L}} = k$, $\varepsilon^{\mathrm{L}} = \varepsilon$ and $\omega^{h\mathrm{L}} = \omega^h$. For the Launder-Sharma low Reynolds number $k-\varepsilon$ model, see Chapter 3.2.1, the outcome of this modeling strategy is

$$\begin{aligned}\frac{\partial \alpha_{\mathrm{L}} k}{\partial t} + \frac{\partial \alpha_{\mathrm{L}} \overline{U}_j^{\mathrm{L}} k}{\partial x_j} &= -\alpha_{\mathrm{L}}\tilde{\varepsilon} - 2\alpha_{\mathrm{L}}\nu_{\mathrm{L}}\frac{\partial\sqrt{k}}{\partial x_j}\frac{\partial\sqrt{k}}{\partial x_j} + \frac{\partial}{\partial x_j}\left[\alpha_{\mathrm{L}}(\nu_{\mathrm{L}} + \frac{\nu_t}{\sigma_k})\frac{\partial k}{\partial x_j}\right] \\ &\quad + \alpha_{\mathrm{L}} P_k + S_k, \end{aligned} \tag{4.21}$$

and

$$\begin{aligned}\frac{\partial \alpha_{\mathrm{L}} \tilde{\varepsilon}}{\partial t} + \frac{\partial \alpha_{\mathrm{L}} \overline{U}_j^{\mathrm{L}} \tilde{\varepsilon}}{\partial x_j} &= -\alpha_{\mathrm{L}} C_{\tilde{\varepsilon}2} f_{\tilde{\varepsilon}2}\frac{\tilde{\varepsilon}}{k}\tilde{\varepsilon} + \alpha_{\mathrm{L}} P_{\tilde{\varepsilon},3} + \frac{\partial}{\partial x_j}\left[\alpha_{\mathrm{L}}(\nu_{\mathrm{L}} + \frac{\nu_t}{\sigma_{\tilde{\varepsilon}}})\frac{\partial \tilde{\varepsilon}}{\partial x_j}\right] \\ &\quad + \alpha_{\mathrm{L}} C_{\tilde{\varepsilon}1}\frac{P_k}{k}\tilde{\varepsilon} + S_\varepsilon. \end{aligned} \tag{4.22}$$

Hereby the source terms are caused by the presence of the dispersed gas phase denoted with S_k and S_ε, which have to be specified through the selected BIT models. For usage of the Jakirlić-Maduta RSM, see Chapter 3.2.2, the turbulent stresses are computed from the following modeled

transport equation

$$\begin{aligned}\frac{\partial \alpha_{\mathrm{L}} \overline{u_i' u_j'}}{\partial t} + \frac{\partial \alpha_{\mathrm{L}} \overline{U}_k^{\mathrm{L}} \overline{u_i' u_j'}}{\partial x_k} &= -\alpha_{\mathrm{L}} \left(\overline{u_i' u_k'} \frac{\partial \overline{U}_j^{\mathrm{L}}}{\partial x_k} + \overline{u_j' u_k'} \frac{\partial \overline{U}_i^{\mathrm{L}}}{\partial x_k} \right) + \alpha_{\mathrm{L}} \Phi_{ij} \\ &\quad + \frac{\partial}{\partial x_k} \left[\alpha_{\mathrm{L}} \left(\frac{1}{2} \nu_{\mathrm{L}} + \frac{\nu_t}{\sigma} \right) \frac{\partial \overline{u_i' u_j'}}{\partial x_k} \right] - \alpha_{\mathrm{L}} \varepsilon_{ij}^h \\ &\quad + S_{R,ij} \end{aligned} \tag{4.23}$$

while ω^h is given by

$$\begin{aligned}\frac{\partial \alpha_{\mathrm{L}} \omega^h}{\partial t} + \frac{\partial \alpha_{\mathrm{L}} \overline{U}_k^{\mathrm{L}} \omega^h}{\partial x_k} &= \frac{\partial}{\partial x_k} \left[\alpha_{\mathrm{L}} \left(\frac{1}{2} \nu_{\mathrm{L}} + \frac{\nu_t}{\sigma} \right) \frac{\partial \omega^h}{\partial x_k} \right] - \alpha_{\mathrm{L}} C_{\omega,1} \frac{\omega^h}{k} P_k \\ &\quad + \alpha_{\mathrm{L}} \frac{2}{k} \left(C_{cr,1} \frac{1}{2} \nu_{\mathrm{L}} + C_{cr_2} \frac{\nu_t}{\sigma} \right) \frac{\partial \omega^h}{\partial x_k} \frac{\partial k}{\partial x_k} \\ &\quad - \alpha_{\mathrm{L}} C_{\omega,2} \omega^h \omega^h + \alpha_{\mathrm{L}} \frac{1}{k} P_{\omega,3} + S_{\omega}. \end{aligned} \tag{4.24}$$

The source terms originating from the bubble-induced turbulence are denoted with $S_{R,ij}$ and S_{ω}. The production terms in the model equations are calculated with $\overline{U}_i^{\mathrm{L}}$ and keep their general form used for single-phase computations. This also applies for every blending function within the models.

Another main aspect of this work is the integration of the IS-RSM respectively the IIS-RSM into the TFM for capturing the turbulent quantities within the liquid phase. This represents a novel approach and the first attempt for simulating dispersed gas-liquid flows, with this specific hybrid RANS/LES scale-resolving method. Thereby no models for describing the bubble-induced turbulence are considered, since the main purpose of using an eddy-resolving method is to reduce the modeled part of the turbulent quantities and hence the influence of these modeled quantities. The idea is now, that the modification of the turbulence in the liquid phase due to the dispersed bubbles are captured within the momentum equations itself. This is due to the modified interfacial forces, caused by the now unsteady velocity fields. As an example, the previously steady state drag force is now unsteady itself (due to the unsteady velocity field), which affects the turbulent motions directly in the momentum equation. It has to be analyzed if these modifications are sufficient for capturing the changes between a single-phase flow and its corresponding two-phase flow. The IS-RSM respectively the IIS-RSM is modified through the change within the

ω^h-equation leading to

$$\left(\frac{D\alpha_{\mathrm{L}}\omega^h}{Dt}\right)_{\text{IS-RSM}} = \left(\frac{D\alpha_{\mathrm{L}}\omega^h}{Dt}\right)_{\text{eq.(4.24)}} + \alpha_{\mathrm{L}} P^*_{\mathrm{SAS}} \tag{4.25}$$

with the adapted P^*_{SAS} term, using the quantities of the liquid phase.

4.2.2 Bubble-induced turbulence modeling

Various different BIT models can be found in the literature. According to Rzehak and Krepper [89] a common assumption for modeling the source term in the k-equation is to relate it to the presence of the drag force assuming that all energy lost by the bubbles due to the drag force is converted into turbulence in the wake of the bubbles. This usually leads to

$$S_k \propto M^{\mathrm{L}}_{\mathrm{d},i} \overline{U}^r_i. \tag{4.26}$$

In contrast, the formulations for the source terms in the particular scale-supplying equations are essentially different. A specific bubble time-scale τ_{B} is defined to obtain S_ε respectively S_ω from S_k, by adopting the same approach as in the heuristic modeling of the source terms in the scale-supplying RANS equations, mentioned in Chapter 3.1. This leads to

$$S_\varepsilon = C_{\varepsilon\mathrm{B}} \frac{S_k}{\tau_{\mathrm{B}}}. \tag{4.27}$$

introducing a modeling constant $C_{\varepsilon\mathrm{B}}$. As stated and discussed by Rzehak and Krepper [89] four different time-scales can be formed in two-phase flows, giving a wide range of available modeling expressions for τ_{B}. The selected BIT models here are developed by Troshko and Hassen [105], which is one of the most popular models, and by Rzehak und Krepper [89] representing a currently developed model. These models are utilized to make an evaluation concerning the capability of this popular approach of considering the influence of the dispersed gas phase on the turbulent fluctuations in the continuous liquid phase. Possible swarm effects or low Reynolds number modifications are not considered here.

The expressions given in Eqs. (4.26) and (4.27) can be used without any further adoption for the two-phase flow computations with the Launder-Sharma $k-\varepsilon$ model, whereas for the integration into the Jakirlić-Maduta RSM several assumptions and modifications have to be taken into account.

First, the source term S_k has to be linked with the source term $S_{R,ij}$ in Eq. (4.23) which is realized by splitting up this source term among the normal components of the Reynolds-stresses which leads to

$$S_{R,ij} = \frac{2}{3} S_k \delta_{ij}. \tag{4.28}$$

This comes along with the assumption that the production of turbulence through the interfacial terms is isotropic. This represents an analogy to the model proposed by Rotta [87] for the connection between the dissipation rate ε and the dissipation tensor ε_{ij} for high Reynolds number single-phase turbulent flows. A very similar strategy to the here utilized approach was done by Lopez de Bertodano et al. ([66] and [65]), who used a similar form of Eq. (4.28) differing only in terms of the proportion of the normal components. The transformation of the source term S_ε towards an appropriate source term for the ω^h-equation can be done by a transformation rule proposed by Rzehak and Krepper [89], which leads to

$$S_\omega = \frac{1}{C_\mu k} S_\varepsilon - \frac{\omega^h}{k} S_k, \tag{4.29}$$

whereas the reason for introducing C_μ remains unclear, since this equation stands in contrast to Eq. (3.34). To keep the transformations consistent, the latter one is used as the standard rule if not otherwise stated.

Model by Troshko and Hassan

The model proposed by Troshko and Hassan [105] uses the above presented relation between drag force and the interfacial production of turbulent kinetic energy through the dispersed gas phase S_k which finally leads to

$$S_k = \alpha_\mathrm{L} M^\mathrm{L}_{\mathrm{d},i} \overline{U}^r_i, \tag{4.30}$$

whereby $M^\mathrm{L}_{\mathrm{d},i}$ is defined through Eq. (4.8). This model was originally developed for the usage within a standard high Reynolds $k-\varepsilon$ model for which a model for the source term S_ε was proposed. Therefore Troshko and Hassan [105] utilized the proposed pseudo turbulent dissipation frequency by Lopez de Bertodano [67] which leads to

$$S_\varepsilon = C_3 \, \frac{3 C_\mathrm{d} \sqrt{\overline{U}^r_k \overline{U}^r_k}}{2 C_\mathrm{vm} d_\mathrm{G}} \, S_k \tag{4.31}$$

with the modeling constant C_3 taking the value 0.45. Hence in this expression, the bubble time-scale is proportional to $d_\mathrm{G} / \sqrt{\overline{U}^r_k \overline{U}^r_k}$.

Model by Rzehak and Krepper

The model proposed by Rzehak and Krepper [89] reads

$$S_k = M^{\mathrm{L}}_{\mathrm{d},i} \overline{U}^r_i, \tag{4.32}$$

whereby the only difference to Eq. (4.32) is the missing factor α_{L}. The modeling of S_ε is based on a newly defined bubble time-scale $\tau_{\mathrm{B}} = d_{\mathrm{G}}/\sqrt{k}$ which leads to

$$S_\varepsilon = C_{\varepsilon\mathrm{B}} \frac{\sqrt{k}}{d_{\mathrm{G}}} S_k. \tag{4.33}$$

This expression includes the not yet specified constant coefficient $C_{\varepsilon\mathrm{B}}$. Rzehak and Krepper [89] suggested $C_{\varepsilon\mathrm{B}} = 1$, but also showed cases where a value of two leads to a better agreement with the reference data.

5 Flow configuration I: Turbulent flows in a vertical pipe

In this chapter, the first flow configuration for the validation of the utilized turbulence models is presented. A set of two corresponding upward turbulent single- and two-phase flows in a vertical pipe is investigated. Hereby is the gravitational vector acting against the axial flow direction with $g_z = -9.81$ m/s. Water has been chosen as the continuous liquid phase and air bubbles as the finely dispersed one. Each of the respective flow configuration sets is characterized by an identical bulk Reynolds number $Re_{\mathrm{D}} = J_{\mathrm{L}}\mathrm{D}/\nu_{\mathrm{L}}$, based on the superficial bulk velocity of the continuous liquid phase J_{L} and the pipe diameter D. The realized computations are validated by the experimental data taken from Hosokawa and Tomiyama ([40] and [41]), providing statistically averaged data for $\overline{U}_i^{\mathrm{L}}$, α_{G}, $\overline{U}_z^r$ and the Reynolds-stress tensor of the liquid phase.

Such turbulent bubbly pipe flows have been investigated by several authors in the TFM framework, mostly by using high Reynolds number eddy-viscosity models for the computation of the turbulence in the continuous liquid phase. For the present experimental flow conditions, this has been done by Hosokawa and Tomiyama [40] and by Rzehak and Krepper [89] to validate several modeling aspects within the TFM. While the former group used the classical high Reynolds number standard $k-\varepsilon$ model by Launder and Spalding [61] as their baseline model, the latter one used the $k-\omega$ SST model by Menter [72]. In both cases, different versions of BIT models, similar to the ones presented in Chapter 4.2, were considered.

Computations of bubbly pipe flows with SMC models are hard to find in the available literature, since such investigations are clearly in the minority. The works of Lopez de Bertodano et al. [66] and Colombo and Fairweather [16], who also analyzed the present experimental reference data, represent one of the few known publications using a differential RSM. In both cases, high Reynolds number models with wall-functions are utilized. Hence, using a low Reynolds number SMC such as the model by Jakirlić

and Maduta in its classical RANS sense represents a major modeling enhancement to these investigations. This also accounts for the $k-\varepsilon$ model by Launder and Sharma for the group of eddy-viscosity models.

The chosen reference experiments have been done at atmospheric pressure and room temperature (here assumed to be 20 °C). This defines the material properties of both phases and leads to $Re_{\mathrm{D}} = 12500$ and 25000, with the experimental conditions listed in tab. 5.1.

Table 5.1: Pipe flow test cases by Hosokawa and Tomiyama ([40] and [41])

Re_{D}	J_{L}	J_{G}	$\alpha_{\mathrm{G}}^{\mathrm{ave}}$	d_{G}
12500	0.5 m/s	0.018 m/s	2.31 %	3.21 mm
25000	1.0 m/s	0.036 m/s	3.30 %	3.66 mm

Here J_{G} and $\alpha_{\mathrm{G}}^{\mathrm{ave}}$ denote the superficial bulk velocity and the cross sectioned averaged phase fraction of the dispersed gas phase. For the two-phase flow with the higher Re_{D} number a classical wall peak behavior for the α_{G} distribution is present, while the flow with the lower one accumulates most of α_{G} in the center of the pipe. A key benefit of this experimental reference data is that every single component of the Reynolds-stress tensor is measured for both single-phase flows as well as for their two-phase flow counterparts. This represents a valuable aspect for a detailed validation of the utilized turbulence models, since a logical approach would demand to first analyze the performance of the present turbulence models in single-phase flows, before calculating the corresponding two-phase flows. Otherwise it is difficult to determine which characteristics or deficiencies of the two-phase flow results actually stem from the presence of the gas phase or are just shortcomings of the turbulence model itself.

To carry out the single-phase flow simulations, the gas phase is not initialized. The presented results are written in cylindrical coordinates, with z being the axial, r the radial and φ the circumferential direction. In fully developed pipe flows, the time averaged flow quantities are homogeneous in axial and circumferential direction, which is used for a spatial averaging over z and φ to obtain the statistical values in the scale-resolving simulations. Such results are denoted with $\langle\Phi\rangle$ throughout the chapter. For the computation in the classical RANS equation framework, no time averaging is needed, since steady results are directly achieved meaning that $\langle\Phi\rangle = \overline{\Phi}$.

5.1 Single-phase flow computations

The novel aspect for single-phase pipe flow computations is that such configurations have not been validated in the works of Jakirlić and Maduta ([49] and [70]) for neither the $\overline{u_i'u_j'}-\omega^h$ RSM nor the IS-RSM respectively the IIS-RSM so far. This gap should be closed with the present work. These single-phase flow computations are additionally validated with the DNS reference data from Khoury et al. [55] at $Re_\mathrm{D}=11700$ ($Re_\tau=361$) and Wu et al. [112] at $Re_\mathrm{D}=24580$ ($Re_\tau=685$), whereby the small difference in Re_D in comparison to the experiments can be neglected. Re_τ is here based on the pipe diameter D. This DNS data also provides references in inner scaling like $\overline{U}_z^+=\left\langle\overline{U}_z^\mathrm{L}\right\rangle/u_\tau$ and $u_i^+=\sqrt{\langle u_i^2\rangle}/u_\tau$. Unfortunately, u_τ (defined by Eq. (3.18)) is not reported for the experiments , which means that this data cannot be included into the results with an inner scaling. All achieved numerical results are of course normalized with their own resulting wall friction velocity.

For the computations within the classical RANS framework, the model by Jakirlić and Maduta (denoted with RSM) and the $k-\varepsilon$ model by Launder and Sharma (denoted with EVM) are used in combination with a two dimensional axis-symmetric solution domain with one cell in the axial flow direction. Since these are steady state computations, the desired averaged flow values are directly obtained and the turbulent quantities only consist of the modeled part $\left(\langle u_iu_j\rangle=\overline{u_i'u_j'}\right)$. Periodic boundary conditions, coupling the in- and outlet of the domain, allow for fully developed flow conditions. An appropriate pressure gradient corresponding to the target bulk Reynolds number is therefore imposed. In radial direction, the grid consist of 100 hexahedral cells with a grid refinement towards the solid wall, resulting in $(\mathrm{R}-r)^+<1$ for the first grid point. $(\mathrm{R}-r)^+$ is the equivalent to y^+ in a pipe flow with the radius R. A finer grid resolution shows no change in the results, which means that a grid independent solution for the present RANS computations has been achieved.

The numerical setup for the scale-resolving simulations includes fully three dimensional grids in order to allow the development of fluctuating turbulent motions. This heavily increases the required computational power in comparison to the corresponding classical RANS computations. To construct these numerical meshes, a so-called o-grid arrangement in the center of the pipe is utilized, with the length of the pipe in the axial direction

set to 2.5 D. Such as for the RANS computations, the in- and outlet of the pipe are coupled via a periodic boundary condition. An important issue in eddy-resolving simulations is the appropriate grid resolution and its influence on the desired time averaged flow quantities. In contrast to classical steady RANS computations, whereby a finer grid resolution sooner or later tends towards a grid independent solution, an increased spatial discretization for scale-resolving method leads to a different instantaneous solution itself since it allows the development of finer turbulent structures and thereby to resolve more parts of the turbulent spectra. Fortunately, the desired statistical flow quantities are usually tending to converge against a solution as long as the number of cells are in the same order. It is now a demanding task to find the smallest amount of cells to obtain sufficiently accurate statistical results, whereby the definition of sufficiently accurate results clearly depends on the test case and the view of the beholder. The meshes here contain a uniformly distributed number of cells in the streamwise N_z and circumferential N_φ flow direction, while the cells over the diameter of the pipe N_r are refined in radial direction towards the solid walls. Only hexahedral cells are used here. Extensive grid studies lead to the cell numbers shown in tab. 5.2, which represent the minimum number of cells to obtain sufficiently accurate results.

Table 5.2: Grid details for the scale-resolving simulations

Re_D	$N_z \times N_\varphi \times N_r$	Δz^+	$\Delta\varphi^+$	Δr^+	cell count
12500	$75 \times 200 \times 110$	24	11	$1 - 11$	700000
25000	$150 \times 320 \times 140$	22	13	$1.8 - 13$	2640000

Normalized cell sizes ($\Delta x_i^+ = \Delta x_i u_\tau^\mathrm{DNS}/\nu_\mathrm{L}$) are compared with available data from the literature. This is to state if these cell numbers are actually in an acceptable range in terms of computational cost especially in comparison to LES. Unfortunately, there seems to be less available LES reference data for pipe than for channel flows, with the work of Eggels [25] being a mentionable exception. A comparison shows that the here utilized dimensionless grid resolution is considerably finer than the one used by Eggels [25] for an LES. Another one can be made with LES data in a channel flow, as it is analyzed (or reviewed) by de Villiers [19] and Fröhlich [28] for a wide range of dimensionless resolutions. Keeping in mind that channel and pipe flows differ considerably in several aspects, these values can nevertheless be used for a rough comparison. While some resolutions are considerably coarse than the values in tab. 5.2, a few authors are also utilizing finer

grids. This leads to the conclusion that the numerical meshes used in this study are in an acceptable range for scale-resolving methods with the IS-RSM respectively the IIS-RSM.

Another aspect in an eddy-resolving simulation is the fact that it has to be executed in an unsteady manner, whereby the time discretization here is done by utilizing the second order BDF (Eq. (2.15)) with an adaptive time stepping method ensuring that the maximum Co number is always below 0.8. Smaller time steps lead to no change in the averaged quantities, while larger time steps (especially with $Co > 1$) lead to a higher possibility of diverging simulations.

A valuable property of the IS-RSM respectively the IIS-RSM, is the ability of allowing the simulation to develop turbulent fluctuations from uniform initial flow conditions until a fully developed turbulent flow is achieved. This can be done without imposing any artificially turbulent fluctuations in contrast to such simulations via LES or the original proposed SST-SAS model by Menter and Egorov [76]. A period of 160 flow-through times is given to achieve these conditions, until the desired flow quantities of interest are averaged for another 160 flow-through times. Simulations with longer time periods showed no further changes in the averaged results. In Fig. 5.1 the instantaneous streamwise velocity field $\overline{U}_z$ for both Reynolds numbers is shown. It can easily be seen that the turbulent structures are considerably finer for $Re_\mathrm{D} = 25000$.

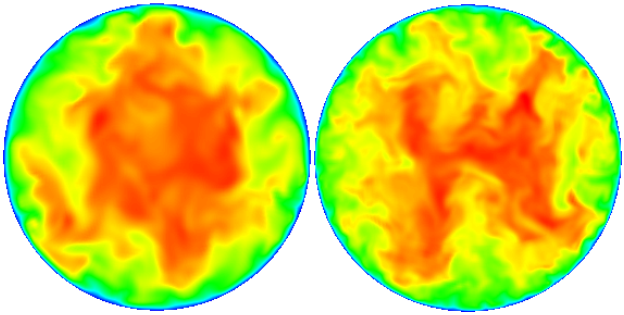

(a) $Re_\mathrm{D} = 12500$ (b) $Re_\mathrm{D} = 25000$

Figure 5.1: Snapshots of the instantaneous axial velocity field $\overline{U}_z$ at two different Reynolds numbers. Red color denotes high velocity.

An important feature associated with the spatial grid resolution in eddy-resolving simulations is the discretization of the convective term in the momentum equation. In the previous works of Jakirlić and Maduta ([49] and [70]) the hybrid scheme presented in Eq. (2.12) is utilized with the value of the blending factor set to $\gamma = 0.95$ (hence 95% CDS and 5% UDS). For the simulation of a turbulent channel flow $Re_\tau = 395$ with the present IS-RSM, this procedure has led to an overall good agreement with the reference DNS data by Kim et al. [56]. Unfortunately, as it is shown in Fig. 5.2, this approach is not leading to satisfying results for the simulation of the turbulent pipe flow at $Re_\mathrm{D} = 11700$ ($Re_\tau = 361$) for both the semi-log $(\mathrm{R}-r)^+$ - $\overline{U}_z^+$ distribution as well as for the normalized turbulent intensities u_i^+. An increase of the blending factor towards $\gamma = 0.98$ does not leading to improved results with the IS-RSM at all.

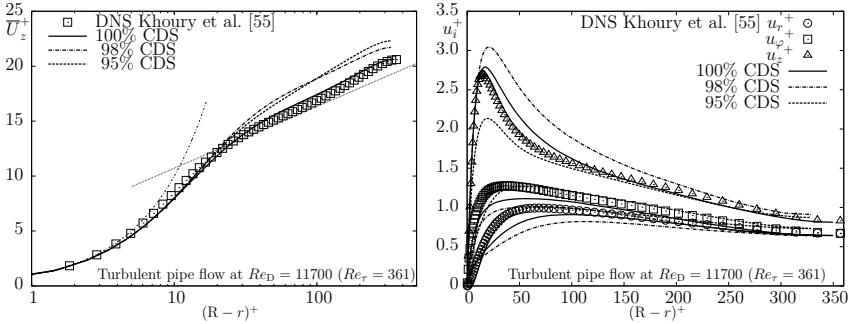

(a) Semi-log $(\mathrm{R}-r)^+$ - $\overline{U}_z^+$ plot

(b) Normalized turbulent intensities

Figure 5.2: Influence of the discretization scheme for the convective term in the momentum equation for the scale-resolving simulations at $Re_\mathrm{D} = 11700$

Apparently, the present blending between UDS and CDS is supposed to introduce a significant amount of numerical diffusion into the pipe flow simulations, which impacts the results in an unacceptable manner. The reason why this behavior is present in pipe and not in channel flow simulations could be the fact that pipe flows have only one periodic boundary condition (in- and outlet) instead of two as it is in channel flows (the sides being a periodic couple too), which generates an additional instability into the simulation eliminating the most amount of numerical diffusion. A possible solution to overcome this issue here, is the usage of pure CDS instead

of a hybrid scheme. Unfortunately, a major issue thereby is the arise of undesired numerical instabilities when exceeding the value $\gamma > 0.98$, leading to diverging simulations for the original proposed IS-RSM. Therefore the lately proposed IIS-RSM by Maduta et al. [71] is utilized to carry out these simulations, since this enhanced modeling formulation allows the usage of CDS. As it is shown in Fig. 5.2 this leads to an overall good agreement with the reference data. As an outcome, all results shown hereafter for the scale-resolving method are obtained with the IIS-RSM and with pure CDS for the discretization of the convective term in the momentum equation.

In Fig. 5.3 the distribution of $\overline{U}_z^+$ over $(\mathrm{R}-r)^+$ is shown, with an overall good prediction for all models. An offset of $\overline{U}_z^+ = 10$ for the results at $Re_\mathrm{D} = 24580$ has been introduced for clarity purpose. The linear law of the wall for $(\mathrm{R}-r)^+ < 5$ is properly calculated by both RANS models, while stronger deviations between the computed results and the DNS data occur in the area of the logarithmic law (see Eq. (3.19)).

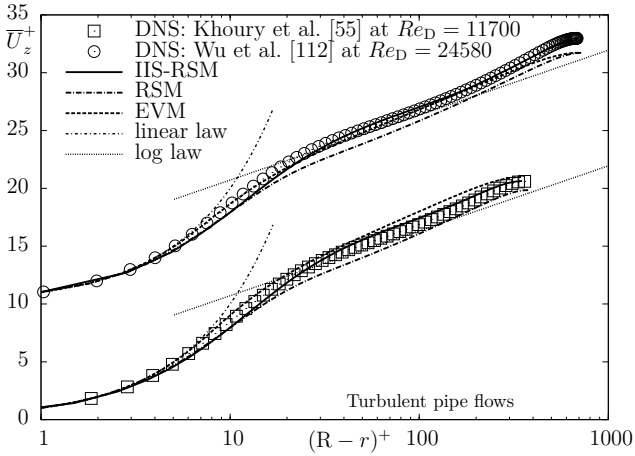

Figure 5.3: Semi-log $(\mathrm{R}-r)^+$ - $\overline{U}_z^+$ plot for pipe flows at different Reynolds numbers. An offset of $\overline{U}_z^+ = 10$ for the results at $Re_\mathrm{D} = 24580$ has been introduced for clarity purpose.

In the case of the RSM this deviation stems from a slightly overestimated u_τ, which is around five percent higher in both cases in comparison to the

reference data. A scaling with u_τ taken from the DNS data would lead to a perfect agreement. The overall best results are achieved with the IIS-RSM, being in a very good agreement with the reference data over the whole flow domain. As stated before, the wall friction velocity was not published by Hosokawa and Tomiyama [40] and [41] and therefore the experimental data could not be included.

The turbulent quantity which directly influences the $\overline{U}_z^+$ progression over the z-component of the RANS equation is the normalized turbulent shear stress $\langle u_r u_z \rangle^+ = \langle u_r u_z \rangle / u_\tau^2$ shown in Fig. 5.4. It is clear that the correct physical behavior is achieved, hence an overestimation of $\langle u_r u_z \rangle^+$ leads to an underestimation of $\overline{U}_z^+$ and vice versa. For the EVM, the shear stress is expressed via $\overline{u_r' u_z'} = -\nu_t \frac{\partial \overline{U}_z^{\mathrm{L}}}{\partial r}$ with ν_t defined by Eq. (3.20).

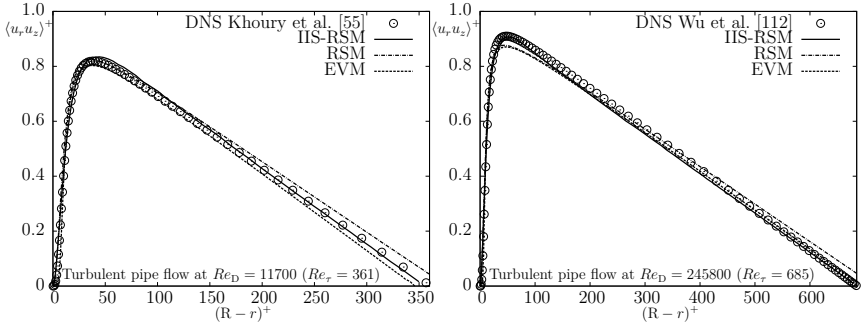

(a) $Re_\mathrm{D} = 11700$ (b) $Re_\mathrm{D} = 24580$

Figure 5.4: Computation of the normalized turbulent shear stress by using both RANS models and the IIS-RSM for the single-phase flow in a vertical pipe at two different Reynolds numbers

The statistically averaged turbulent intensities $\langle u_i \rangle = \sqrt{\langle u_i^2 \rangle}$ obtained with the RSM and the IIS-RSM are normalized with the respective J_L, to also include the experimental data into Fig. 5.5. For the EVM, all three intensities would result in $\langle u_i \rangle = \sqrt{2/3k}$ due to Eq. (3.8) and are therefore not included. As seen in Fig. 5.5, the results are in an qualitatively good agreement with the reference data, exhibiting a few quantitative deviations. For the RSM, the strongest deviation occurs in the region around the symmetry axis, whereby the turbulent intensities are over predicted. This behavior is

frequently addressed to be caused by the Shir [97] turbulent diffusion model within the SGDH. It is well-known that this model formulation is not invariant with respect to the coordinate system transformation, as for e.g. stated by Hanjalić [33]. The IIS-RSM is capable of determining the correct behavior in the center of the pipe for both Reynolds numbers. Overall, the agreement between the calculated and the reference $\langle u_z \rangle$ is the best of the three intensities for both Reynolds-stress models. It should be noticed that there are small differences between the experimental and the DNS data for $\langle u_z \rangle$ at $Re_\mathrm{D} = 25000$.

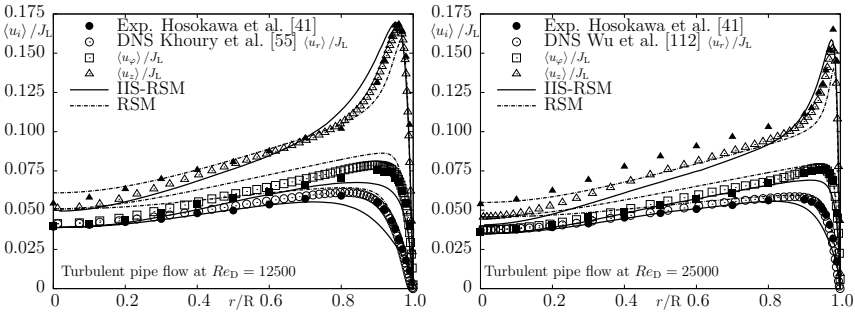

(a) $Re_\mathrm{D} = 12500$ (b) $Re_\mathrm{D} = 25000$

Figure 5.5: Computation of the normalized turbulent intensities by using the RSM and the IIS-RSM for the single-phase flow in a vertical pipe at two different Reynolds numbers

To also analyze the performance of the EVM, the normalized turbulent kinetic energy $\langle k \rangle / J_\mathrm{L}^2 = 1/2 \langle u_j u_j \rangle / J_\mathrm{L}^2$ is shown in Fig. 5.6. The EVM exhibits a strong deviation from the reference data in the areas close to the wall and is not capable of capturing the wall peak behavior, which is a well known deficiency of such classical eddy-viscosity models. In comparison to that, the RSM gives a better agreement with respect to the near-wall peak, but produces nearly the same deviation in the core region of the flow as the EVM. As it is the case for the turbulent intensities, the best results are achieved by using the IIS-RSM, leading to an overall good assessment with the reference data.

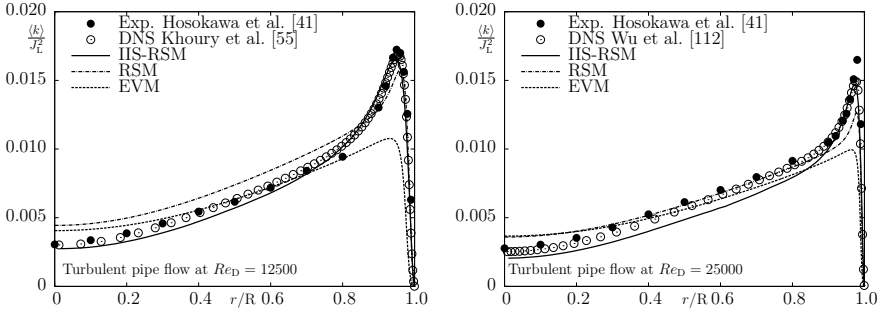

(a) $Re_D = 12500$ (b) $Re_D = 25000$

Figure 5.6: Computation of the normalized kinetic energy by using both RANS models and the IIS-RSM for the single-phase flow in a vertical pipe at two different Reynolds numbers

A desired aspect in the simulation of turbulent flows via hybrid RANS/LES methods is that a certain amount of the turbulent fluctuations still stem from the modeled turbulence, expressed by the underlying RANS model. Otherwise the question would arise, why an LES is not used, since the amount of modeled fluctuations would be small enough to be expressed by a less complex and computational expensive model. A possible measure therefore is to analyze how much of $k^+ = \langle k \rangle / u_\tau^2 = (\langle k \rangle_{\mathrm{mod}} + \langle k \rangle_{\mathrm{res}})/u_\tau^2$ actually stems from the modeled part $\langle k \rangle_{\mathrm{mod}} = 1/2 \left\langle \overline{u_j' u_j'} \right\rangle$ in comparison to the resolved one $\langle k \rangle_{\mathrm{res}} = 1/2 \left\langle u_j'' u_j'' \right\rangle$. As it is shown in Fig. 5.7 the IIS-RSM leaves no amount of modeled turbulence in the areas away from the wall. But close to the solid wall, $\langle k \rangle_{\mathrm{mod}}$ reaches around 25% of $\langle k \rangle$. Since Pope [82] recommends (as a rough estimate), that in a well resolved LES the modeled amount of turbulence should under no circumstances exceed more than 20%, the meshes here can be classified as an appropriate choice for this hybrid RANS/LES technique.

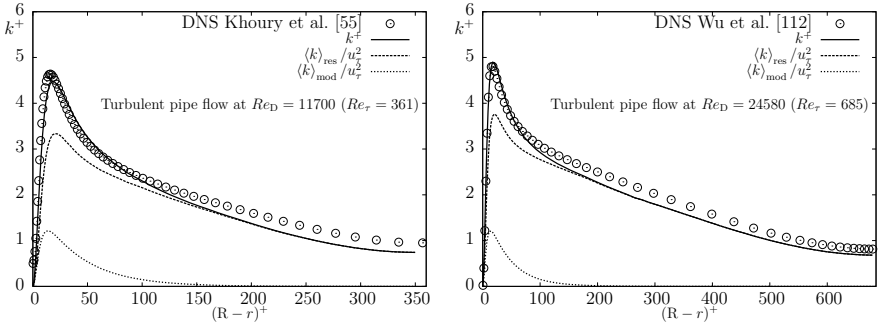

(a) $Re_D = 11700$ (b) $Re_D = 24580$

Figure 5.7: Comparison between the modeled and resolved part of k^+ obtained with the IIS-RSM for the single-phase flow in a vertical pipe at two different Reynolds numbers

The above results show that all of the here utilized models are capable of reproducing the reference data in an overall good agreement. Clearly, the IIS-RSM leads to superior results, but at the expense of heavily increased computational cost. The enhancement of the original proposed IS-RSM towards the IIS-RSM by Maduta et al. [71] in terms of numerical robustness represents an essential key point in the further usage of this scale-resolving method, since CDS can be used instead of a hybrid discretization scheme.

5.2 Two-phase flow computations

In the following section the corresponding two-phase pipe flow calculations are presented, since the utilized turbulence models have proven their potential in the previously presented single-phase flows. Thereby are the RANS computations presented first and separated from the subsequent following eddy-resolving simulations.

The present two-phase flow RANS computations are executed on the identical two dimensional axis-symmetric grids already used for the corresponding single-phase flow computations, whereby the TFM is capable of dealing with the distinct mesh refinement towards the solid wall. Using periodic boundary conditions in such a bubbly pipe flow possesses some uncertainties. An appropriate pressure gradient is set up to ensure a mixture flow velocity defined by $U^{\mathrm{ave}} = J_{\mathrm{G}}\alpha_{\mathrm{G}}^{\mathrm{ave}} + J_{\mathrm{L}}\left(1-\alpha_{\mathrm{G}}^{\mathrm{ave}}\right)$, which does not automatically guarantee the correct flow rate for every present phase. This is only achieved if the applied drag force model is capable of determining the relative velocity between both phases in an acceptable range. For the presently considered computations the utilized drag force models by Tomiyama et al. [103] (Eq. (4.11)) in combination with the swarm effect correlation by Legendre and Magnaudet [62] (Eq. (4.13)) lead to the desired experimental flow rates for each phase in an acceptable deviation range. The cross section averaged liquid phase velocity does not deviate more than one percent, while the one for the gas phase does not vary more than five percent from the experimental values in tab. 5.1. Similar difficulties were also reported by Rzehak and Krepper [89]. The interfacial momentum transfer term is included via Eq. (4.18), since for the RANS computations no phase inversion occurs.

One of the main goals in bubbly pipe flow computations is to predict the radial distribution of α_{G} correctly. Unfortunately, this a demanding task since a significant number of interacting influencing factors determine this distribution. The continuity Eqs. (4.5) allow no conclusion for the present fully developed steady state pipe flows, since both simplify towards $0 = 0$. Instead, a deeper insight can be gained by simplifying the momentum Eq. (4.6) for both phases in cylindrical coordinates. Under present assumptions ($\partial/\partial t = \partial/\partial\varphi = \partial/\partial z$ (except for $\overline{P}$) $= \overline{U}_r^{\phi} = \overline{U}_{\varphi}^{\phi} = 0$) this results in

$$0 = -\frac{\alpha_\mathrm{L}}{\rho_\mathrm{L}}\frac{\partial \overline{P}}{\partial r} - \frac{d\alpha_\mathrm{L}\overline{u_r' u_r'}}{dr} + \frac{\alpha_\mathrm{L}}{r}\left(\overline{u_\varphi' u_\varphi'} - \overline{u_r' u_r'}\right) - \frac{M_r^\mathrm{L}}{\rho_\mathrm{L}} \tag{5.1}$$

for the liquid phase and

$$0 = -\frac{\alpha_\mathrm{G}}{\rho_\mathrm{G}}\frac{\partial \overline{P}}{\partial r} - \frac{d\alpha_\mathrm{G}\overline{u_r'^\mathrm{G} u_r'^\mathrm{G}}^\mathrm{G}}{dr} + \frac{\alpha_\mathrm{G}}{r}\left(\overline{u_\varphi'^\mathrm{G} u_\varphi'^\mathrm{G}}^\mathrm{G} - \overline{u_r'^\mathrm{G} u_r'^\mathrm{G}}^\mathrm{G}\right) - \frac{M_r^\mathrm{G}}{\rho_\mathrm{G}} \tag{5.2}$$

for the gas phase. Clearly, these equations are only valid for RANS computations and not for eddy-resolving simulations. Following the procedure by Drew and Lahey [24] by eliminating the pressure gradient and using $M_i^\mathrm{G} = -M_i^\mathrm{L}$ both equations can be combined to

$$\begin{aligned}
&\left(\alpha_\mathrm{G}\overline{u_r' u_r'} + \frac{\rho_\mathrm{G}}{\rho_\mathrm{L}}\left(1-\alpha_\mathrm{G}\right)\overline{u_r'^\mathrm{G} u_r'^\mathrm{G}}^\mathrm{G}\right)\frac{d\alpha_\mathrm{G}}{dr} = \\
&+\alpha_\mathrm{G}\left(1-\alpha_\mathrm{G}\right)\left[\frac{d\overline{u_r' u_r'}}{dr} - \frac{\overline{u_\varphi' u_\varphi'} - \overline{u_r' u_r'}}{r}\right] \\
&-\alpha_\mathrm{G}\left(1-\alpha_\mathrm{G}\right)\frac{\rho_\mathrm{G}}{\rho_\mathrm{L}}\left[\frac{d\overline{u_r'^\mathrm{G} u_r'^\mathrm{G}}^\mathrm{G}}{dr} - \frac{\overline{u_\varphi'^\mathrm{G} u_\varphi'^\mathrm{G}}^\mathrm{G} - \overline{u_r'^\mathrm{G} u_r'^\mathrm{G}}^\mathrm{G}}{r}\right] \\
&-\frac{M_r^\mathrm{L}}{\rho_\mathrm{L}}.
\end{aligned} \tag{5.3}$$

This equation contains the three main influencing factors for the radial distribution of α_G on the right hand side, which are the turbulence in the continuous liquid phase, the turbulence in the dispersed gas phase and the interfacial forces in radial direction. By comparing the turbulent stresses, it is obvious that the terms including the turbulence of the gas phase are always multiplied with the factor $\rho_\mathrm{G}/\rho_\mathrm{L}$, which for the present material combination of air-liquid usually is in the order of 10^{-3}. This immediately clarifies why the turbulence in the gas phase can be neglected, in comparison to the one in the liquid phase, which simplifies Eq. (5.3) towards

$$\begin{aligned}
\alpha_\mathrm{G}\frac{d\alpha_\mathrm{G}}{dr} \quad &= \frac{\alpha_\mathrm{G}\left(1-\alpha_\mathrm{G}\right)}{\overline{u_r' u_r'}}\left[\frac{d\overline{u_r' u_r'}}{dr} - \frac{\overline{u_\varphi' u_\varphi'} - \overline{u_r' u_r'}}{r}\right] \\
&\quad - \frac{C_\mathrm{td} k}{\overline{u_r' u_r'}}\frac{d\alpha_\mathrm{G}}{dr} - \frac{\alpha_\mathrm{G} C_\mathrm{l}\overline{U}_z^r}{\overline{u_r' u_r'}}\frac{d\overline{U}_z^\mathrm{L}}{dr}
\end{aligned} \tag{5.4}$$

having already inserted the lift (4.15) and the turbulent dispersion (4.17) force, which are the forces acting in radial direction. The procedure to neglect the turbulence in the gas-phase has also been done by Hosokawa and Tomiyama [40] and Rzehak and Krepper [89] for the present bubbly pipe flows. Eq. (5.4) demonstrates the complex modeling challenge for computing the radial distribution of α_G. It is easy to imagine how even more complicated this subject becomes if the wall lubrication force is also considered. Besides being theoretically questionable, Hosokawa and Tomiyama [40] showed that this force has only a minor impact on the results of the present test cases, which justifies the decision to neglect this force here. On the other hand Rzehak et al. [90] showed that this force of course can have an impact in other bubbly pipe flow configurations.

Another aspect which is usually not addressed is that the correct influence of the turbulent stresses on α_G can only be described by an SMC model, as stated by Lopez de Bertodano et al. [66], since an eddy-viscosity model is not capable of capturing the anisotropy effects of the Reynolds-stress tensor. This becomes clear if Eq. (5.4) is simplified by including the Boussinesq hypothesis [11] (Eq. (4.20)) towards

$$\alpha_G \frac{d\alpha_G}{dr} = \frac{\alpha_G\left(1-\alpha_G\right)}{k}\frac{dk}{dr} - \frac{3}{2}C_\mathrm{td}\frac{d\alpha_\mathrm{G}}{dr} - \frac{3}{2}\frac{\alpha_\mathrm{G}C_\mathrm{l}\overline{U}_z^r}{k}\frac{d\overline{U}_z^\mathrm{L}}{dr} \tag{5.5}$$

which significantly changes the impact of the turbulence in the first term on the right hand side. The influence of this term can be further illustrated with the help of the radial component of the RANS equations in a single-phase pipe flow, which reads

$$\frac{1}{\rho_\mathrm{L}}\frac{\partial\overline{P}}{\partial r} = -\underbrace{\frac{d\overline{u_r'u_r'}}{dr} + \frac{\left(\overline{u_\varphi'u_\varphi'} - \overline{u_r'u_r'}\right)}{r}}_{\mathrm{RSM}} \approx \underbrace{-\frac{2}{3}\frac{dk}{dr}}_{\mathrm{EVM}}. \tag{5.6}$$

While an RSM represents an exact description, an eddy-viscosity model significantly changes the way the radial pressure gradient is determined in single-phase pipe flows. For the here utilized models, the resulting radial pressure distribution is shown in Fig. 5.8. Clearly, the RSM as well as the IIS-RSM (being not covered by Eq. (5.6)) give qualitatively and quantitatively better results than it is the case for the EVM, which considerably differs from the experimental data. Hence, if the pressure gradient in a single-phase flow is not correctly captured, it cannot be expected that it is

in a two-phase flow, if even k would be in a perfect agreement with the reference data. It is visible that the resulting pressure distributions for both the RSM as well as the IIS-RSM are not in a very good agreement with the reference data, which can be explained by the turbulent intensities in Fig. 5.5. For the EVM it can be at least stated that the model predicts the increasing pressure towards the solid wall.

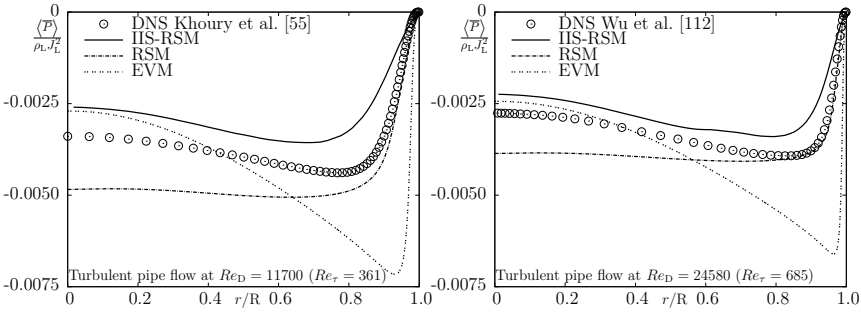

(a) $Re_D = 11700$ (b) $Re_D = 24580$

Figure 5.8: Computation of the normalized radial pressure distribution by using both RANS models and the IIS-RSM for the single-phase flow in a vertical pipe at two different Reynolds numbers

The increase of $\overline{P}$ towards the wall appears in areas that are only captured by low Reynolds number models. It is possible that the increased pressure is actually adopting the role that the wall lubrication force is supposed to play in high Reynolds number computations, by avoiding the bubbles to reach the wall. Nevertheless, one conclusion of this topic is that even if the turbulent quantities would be exactly determined by a suitable turbulence model, the choice of the C_l and C_{td} still would have to vary between an SMC model and an eddy-viscosity model to balance the different formulations in Eq. (5.4) and Eq. (5.5). Furthermore, these equations show the complexity of computing the α_G distribution, which depends on the baseline turbulence model with a possible extension by a BIT model and the models for the interfacial forces. The lift force, influenced by the drag force via $\overline{U}_z^r$, is thereby pressing the gas phase towards the wall, while the turbulent dispersion force aims to achieve an uniform α_G distribution. Only the virtual mass force has no influence, since the acceleration term is zero under fully developed pipe flow conditions. These influencing factors and

their interactions have been investigated in several studies, whereby none of these investigations has proposed a selection of models, yielding an overall good performance over a wide range of turbulent bubbly pipe flow test cases. This is also indicated by the wide range of existing interfacial force models (already discussed within Chapter 4.1).

Clearly, an evaluation of the performance of the present baseline turbulence and BIT models can only be done if the radial distribution of α_G is at least captured within the right order of magnitude in comparison to the experimental reference data. Otherwise a divergent α_G distribution would heavily influence these models through a false input parameter. As a consequence, the coefficients C_l and C_{td} are adjusted for every single computation to ensure a more or less accurate distribution of α_G. This is of course an unsatisfactory situation, since this approach requires knowledge about the experimental results in advance. But clearly, the development of generally applicable interfacial force models for the present test cases is beyond the scope of this work and since the present investigations are focused on the performance of the turbulence models, this represents the most promising approach. For the BIT models, the correct distribution of α_G is even more important, since $M^L_{d,i}$ acts as major modeling parameter in Eq. (4.26). A strong deviation of α_G would not allow any judgment about the capability of capturing the modulation of the turbulence in the continuous liquid phase caused by the presence of the dispersed bubbles.

Performance of the baseline models

In a first step, the performance of the baseline RANS models, again denoted with RSM and EVM, are analyzed, with special focus on the modulation between the single- and the two-phase flow quantities. At this stage no BIT models are incorporated into the respective turbulent equations. For these computations, the values shown in tab. 5.3 for C_l and C_{td} are utilized.

Table 5.3: Coefficients for the utilized interfacial forces C_l and C_{td}

	EVM		RSM	
Re_D	C_l	C_{td}	C_l	C_{td}
12500	0	2.0	0	1.0
25000	0.15	1.0	0.28	1.0

These particular values are not completely chosen arbitrarily since e.g. $C_\mathrm{l} = 0.28$ would have been achieved by the correlation from Tomiyama et al. [104], while for C_td only the value of two seems to be uncommon compared to the range between 0.1 and 1.0 given by Lahey and Drew [57]. The resulting α_G distributions are shown in Fig. 5.9 and it is evident that the chosen interfacial forces are leading to the qualitatively correct behavior. For the lower Reynolds number, α_G shows an accumulation in the center of the pipe, while for the higher number the wall peak behavior is achieved. The EVM is thereby much more aggressive in forcing the gas phase against the wall, which is justified by the utilized interfacial coefficient values in tab. 5.3. Setting $C_\mathrm{l} = 0.28$ for the EVM at $Re_\mathrm{D} = 25000$, as it is the case for the RSM, would lead to a distinct overprediction of the wall peak. Also would $C_\mathrm{td} = 1$ for the EVM at $Re_\mathrm{D} = 12500$ lead to a wall peak behavior. For both models C_l is thereby set to zero, to avoid the latter behavior.

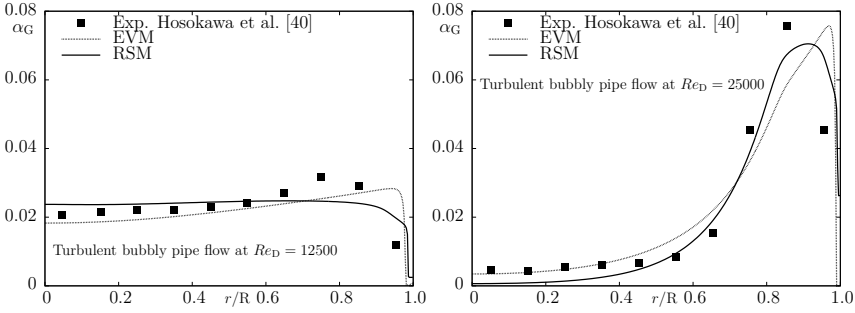

(a) $Re_\mathrm{D} = 12500$ (b) $Re_\mathrm{D} = 25000$

Figure 5.9: Computation of the gas volume fraction by using both baseline RANS models for the bubbly flow in a vertical pipe at two different Reynolds numbers

These different behaviors between the EVM and the RSM can mainly be explained by Eq. (5.4) and Eq. (5.5), since the term representing the influence of the turbulence (and hence the radial pressure gradient) in the liquid phase on α_G is essentially different. Another difference between both models can be seen in Fig. 5.10 for the resulting k distribution. For $Re_\mathrm{D} = 12500$ the resulting k distribution for the EVM is lower in comparison to the one for the RSM, which results in a weaker determination of the turbulent dispersion force. This has to be compensated through increasing C_td. Both

models are not capable of actually capturing the strongly increased values of k for $Re_{\mathrm{D}} = 12500$ in comparison to the corresponding single-phase flow. The EVM actually decreases the k distribution. For $Re_{\mathrm{D}} = 25000$ both models show this behavior. Under no circumstances is the increased peak value between the single- and the two-phase flow captured.

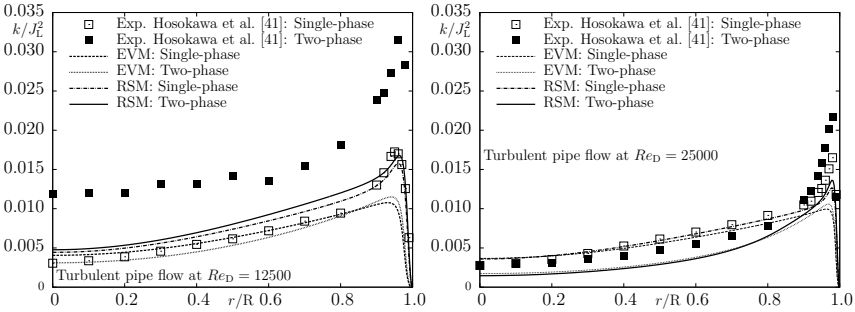

(a) $Re_{\mathrm{D}} = 12500$ (b) $Re_{\mathrm{D}} = 25000$

Figure 5.10: Computation of the normalized turbulent kinetic energy by using both baseline RANS models for the single-phase flow and the bubbly flow in a vertical pipe at two different Reynolds numbers

Fig. 5.11 compares $\overline{U}_z^{\mathrm{L}}/J_{\mathrm{L}}$ for both single- and two-phase flow computations. It can be seen that both models are capable of computing the velocities in the correct range, whereby several qualitative and quantitative differences to the reference data occur, which is more distinct for $Re_{\mathrm{D}} = 12500$. Here, the models falsely predict a small velocity increase between the single- and two-phase flow in the center of the pipe, while being qualitatively capable of capturing the increase of $\overline{U}_z^{\mathrm{L}}$ in the areas close to the solid wall. These small changes in the liquid velocity and therefore of its gradient between the single- and the two-phase flow are one cause for the modified k values shown in Fig. 5.10 through the modified production terms. An essential difference between both RANS models for the present flow cases cannot be determined at this stage. The same statement can be made for the relative velocity $\overline{U}_z^{r}$ in m/s (as usual not normalized), whereby the qualitative decrease close to the wall is captured by both models, without reproducing the quantitative distribution. Responsible for this decrease is the swarm correlation defined by Legendre and Magnaudet [62] (Eq. (4.13)). Without

this, a nearly uniform value of $\overline{U}_z^r$ over r would be achieved resulting in an overestimation of the lift force in the near-wall area.

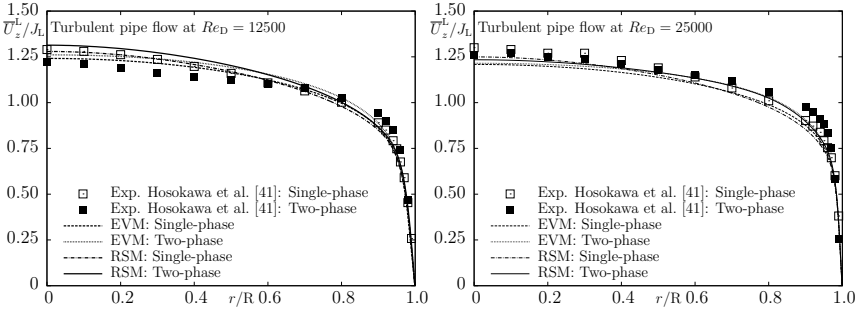

(a) $Re_D = 12500$ (b) $Re_D = 25000$

Figure 5.11: Computation of the normalized axial liquid velocity by using both baseline RANS models for the single-phase flow and the bubbly flow in a vertical pipe at two different Reynolds numbers

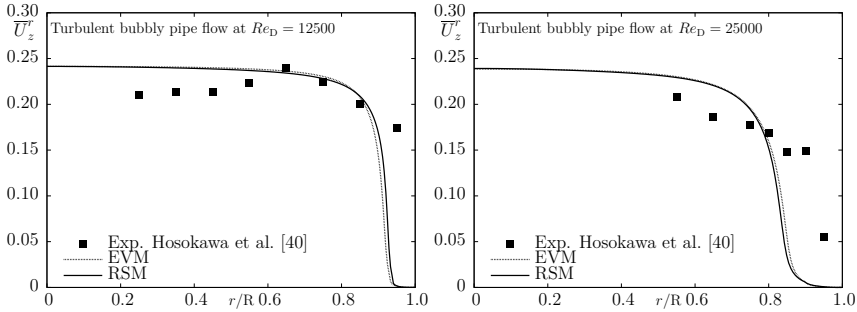

(a) $Re_D = 12500$ (b) $Re_D = 25000$

Figure 5.12: Computation of the axial relative velocity (in m/s) by using both baseline RANS models for the bubbly flow in a vertical pipe at two different Reynolds numbers

The resulting turbulent intensities $u_i' = \sqrt{\overline{u_i'^2}}$ for the baseline RSM shown in Fig. 5.13 give mixed impressions. For the lower Reynolds number, the model does not modify the outcome in comparison to the corresponding single-phase flow at all. Since the turbulent intensities are considerably increased for the two-phase flow, the obtained results exhibit a strong deviation. On the other hand, u_r' and u_φ' for $Re_\mathrm{D} = 25000$ are both calculated in a good agreement with the reference data. It is important to notice that in the experimental data nearly no difference occurs between the single- and two-phase flow and the RSM now captures both distributions with its two-phase flow result. The strongly increased peak values of u_z' close to the wall are not captured for both cases. Fig. 5.10 and Fig. 5.13 are consistent to one another. In Fig. 5.14 the turbulent shear stress is compared. Both models are capable of capturing the modulation between the single- and two-phase flow in a very good agreement for $Re_\mathrm{D} = 25000$. For $Re_\mathrm{D} = 12500$ the EVM (using $\overline{u_r' u_z'} = -\nu_t \frac{\partial \overline{U}_z^\mathrm{L}}{\partial r}$) is giving quantitatively and qualitatively false results by predicting a decrease instead of an increase, while the RSM at least captures the distribution up to a position of $r/\mathrm{R} = 0.8$.

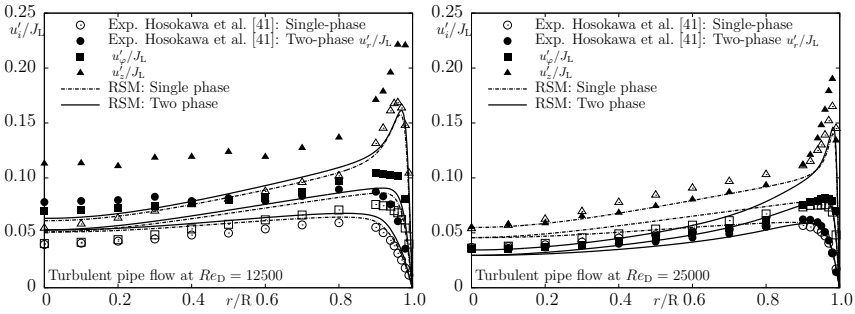

(a) $Re_\mathrm{D} = 12500$ (b) $Re_\mathrm{D} = 25000$

Figure 5.13: Computation of the normalized turbulent intensities by using the RSM for the single-phase flow and the bubbly flow in a vertical pipe at two different Reynolds numbers

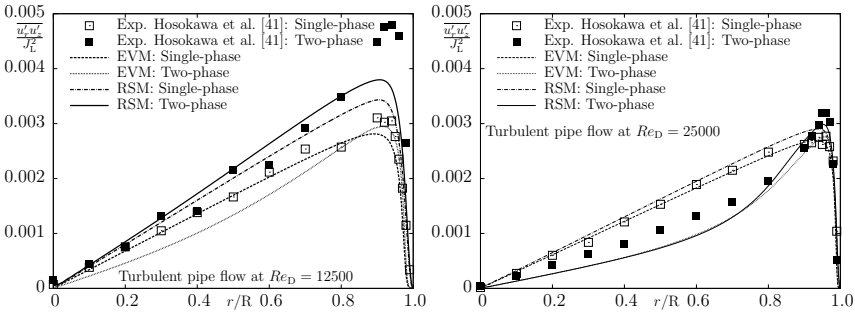

(a) $Re_D = 12500$ (b) $Re_D = 25000$

Figure 5.14: Computation of the normalized turbulent shear-stress by using both baseline RANS models for the single-phase flow and the bubbly flow in a vertical pipe at two different Reynolds numbers

The present results demonstrate that low Reynolds number turbulence models can be used for bubbly flow computations. Even a complex second-moment closure model such as the here utilized RSM is capable of giving reasonable results. While the qualitative agreement between the experimental data and the obtained results is overall conclusive, the results could still be improved to also achieve a quantitative agreement.

Performance of the additionally utilized BIT models

The previously presented results show the deficiency of both baseline models to capture the modulation between the single-phase flow turbulence towards the one in a two-phase flow. As a next step, it is analyzed if these shortcomings can be corrected by using the BIT models presented in Chapter 4.2. Below, the extended baseline models will be labeled with +T for the model of Troshko and Hassan [105] and with +R for the one of Rzehak and Krepper [89]. The description of the latter one includes some unspecified or uncertain modeling parameters, which are analyzed in the following investigations. One of these is the value of $C_{\varepsilon \mathrm{B}}$, which varies in Rzehak and Krepper [89] between one and two. Another uncertainty is concerning the transformation rule (Eq. (4.29) or Eq. (3.34)) to obtain S_ω from S_ε as discussed in Chapter 4.2. Of course, this problem does not occur for the EVM computations. Since the turbulent quantities are mod-

ified through the BIT models, C_{l} is re-calibrated to obtain comparable α_{G} distributions for all investigated modeling formulations. This is only necessary for $Re_{\mathrm{D}} = 25000$, since for $Re_{\mathrm{D}} = 12500$ this value is already set to zero to ensure the accumulation of gas in the center of the pipe. Figs. 5.15 and 5.16 show these gas volume fraction distributions.

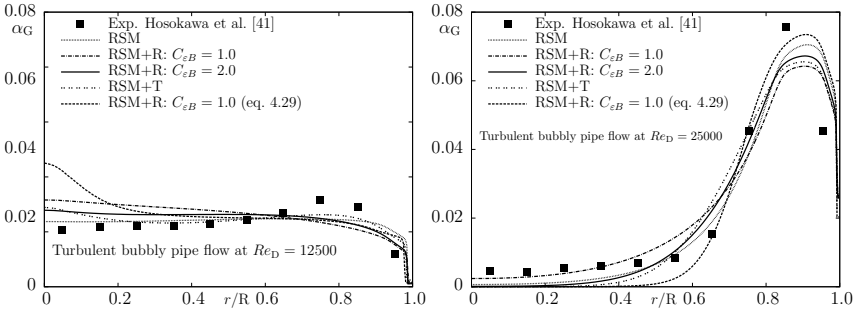

(a) $Re_{\mathrm{D}} = 12500$ (b) $Re_{\mathrm{D}} = 25000$

Figure 5.15: Computation of the gas volume fraction by using the RSM with additionally utilized BIT models for the bubbly flow in a vertical pipe at two different Reynolds numbers

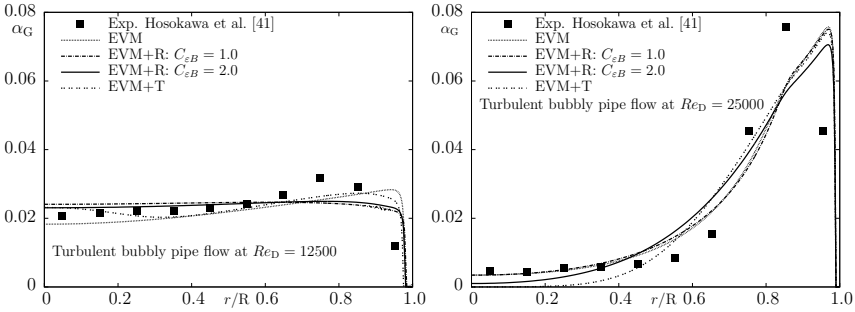

(a) $Re_{\mathrm{D}} = 12500$ (b) $Re_{\mathrm{D}} = 25000$

Figure 5.16: Computation of the gas volume fraction by using the EVM with additionally utilized BIT models for the bubbly flow in a vertical pipe at two different Reynolds numbers

For the case with the lower Reynolds number, the behavior of the RSM+R in combination with the transformation rule Eq. (4.29) leads to an undesired increase of α_G in the center of the pipe, which could not be altered by modifying C_l or C_{td}. All the other tested model combinations give results in a comparable range to the experimental data.

Further insights can be obtained by analyzing the computed values for k shown in Figs. 5.17 and 5.18. Obviously, utilizing a BIT model can lead to questionable results which is most pronounced for $Re_D = 12500$ in Figs. 5.17a and 5.18a. On the one hand, the model by Rzehak and Krepper [89] with $C_{\varepsilon B}$ set to one leads to a strong overestimation of k for both RANS models, but on the other hand yields an enormous (and false) reduction of k when using Eq. (4.29) instead of the default transformation by Eq. (3.34) for the RSM computations. Both behaviors are less pronounced at $Re_D = 25000$. The model by Troshko and Hassan [105] leads to a decrease of k in comparison to the respective baseline models at both Reynolds numbers, with occasional exceptions in the center of the pipe. All models have only a comparatively small impact on the results at $Re_D = 25000$, which confirms that the influence of the bubble-induced turbulence, in comparison to the shear induced one is much weaker here than for the lower Reynolds number.

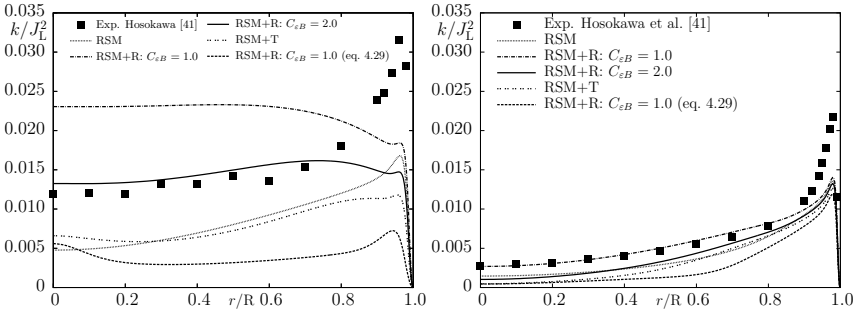

(a) $Re_D = 12500$ (b) $Re_D = 25000$

Figure 5.17: Computation of the normalized turbulent kinetic energy by using the RSM with additionally utilized BIT models for the bubbly flow in a vertical pipe at two different Reynolds numbers

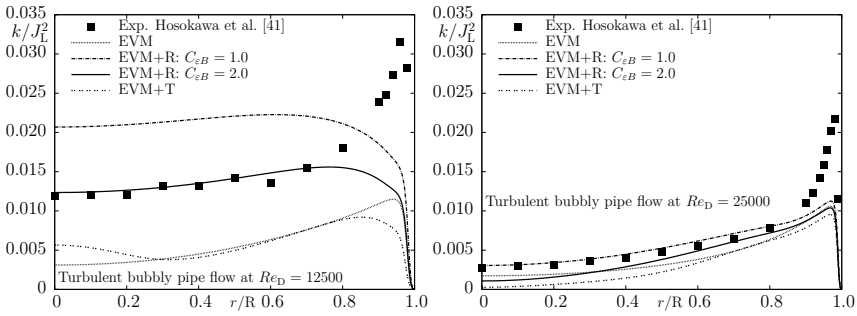

(a) $Re_D = 12500$ (b) $Re_D = 25000$

Figure 5.18: Computation of the normalized turbulent kinetic energy by using the EVM with additionally utilized BIT models for the bubbly flow in a vertical pipe at two different Reynolds numbers

An overall good assessment is achieved with the model by Rzehak and Krepper [89] with $C_{\varepsilon B} = 2$ for both Reynolds numbers. As an outcome, the RSM+R combined with the transformation through Eq. (4.29) is not further analyzed, since the negative impact on k indicates that this transformation rule can be regarded as questionable. For both models, the value of $C_{\varepsilon B} = 1.0$ is omitted in the succeeding investigations, since the strong overprediction of k at $Re_D = 12500$ clearly disqualifies this one. It should be mentioned that considering the swarm effects in the drag force coefficient in Eq. (4.26), leads to negligible changes of the results, which are therefore not shown here. The normalized turbulent intensities obtained with the different RSM computations are shown in Fig. 5.19, confirming the outcome of the turbulent kinetic energy distribution. Again, the model by Troshko and Hassan [105] leads to an essential decrease of the turbulent intensities in comparison to the baseline model, with an exception in the center area of the pipe at $Re_D = 12500$. For the RSM+R with $C_{\varepsilon B} = 2.0$, the intensities differ considerably to the experimental ones at $Re_D = 12500$. Disregarding the behavior close to the wall, u'_φ and u'_r are overestimated while the opposite occurs for u'_z, which in sum still leads to the very good agreement of k shown in Fig. 5.17a. This indicates that Eq. (4.28), used to split S_k among the normal components of $\overline{u'_i u'_j}$, is actually an insufficient approach for determine the relationship between S_k and $S_{R,ij}$. A possible solution would be to increase the amount of bubble-induced turbulence in

the streamwise direction, as been done by Colombo and Fairweather [16]. Again, the influences are more distinct for the lower Reynolds number.

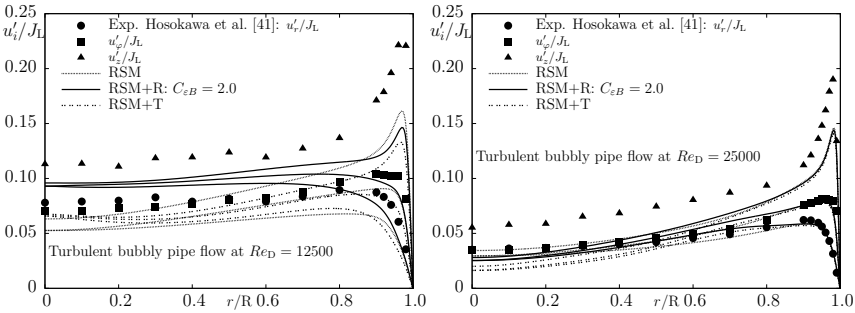

(a) $Re_D = 12500$ (b) $Re_D = 25000$

Figure 5.19: Computation of the normalized turbulent intensities by using the RSM with additionally utilized BIT models for the bubbly flow in a vertical pipe at two different Reynolds numbers

While for the turbulent quantities the BIT models lead to ambivalent results, it influences the results for the normalized axial mean velocity $\overline{U}_z^L/J_L$ in a manner that is not acceptable as it is shown in Fig. 5.20 (note the different y-axis scaling in Fig. 5.20a). For both Reynolds numbers the BIT models lead to an inacceptable increase of the velocity in the core region of the flow and a strong decrease in the areas close to the solid wall, which is both more pronounced for $Re_D = 12500$. The model by Troshko and Hassan [105] is thereby leading to a stronger deviation than the model by Rzehak and Krepper [89]. For $Re_D = 25000$ the latter produces the only acceptable results with a BIT model here. Clearly, a slightly better reproduction of the turbulent quantities does not balance the overall bad results concerning the velocity field. The influence of the particular BIT model seems to stronger for the EVM than for the RSM, because the modified k values are directly fed into ν_t which has a major impact on the results for eddy-viscosity models through the turbulent shear stress. Fig. 5.21 shows these stresses. While the results are only slightly altered for the higher Reynolds number, the impact of the models for $Re_D = 12500$ is distinct. Unfortunately, the results are not improved but have become worse especially for EVM+T. Only the computations with RSM+R can at least assure the performance of the baseline RSM. It remains unclear for both models

which amount of the modified k respectively $\overline{u_i' u_j'}$ values are actually directly caused from the BIT models or by a modulated P_k respectively P_{ij} caused by the altered velocity gradient.

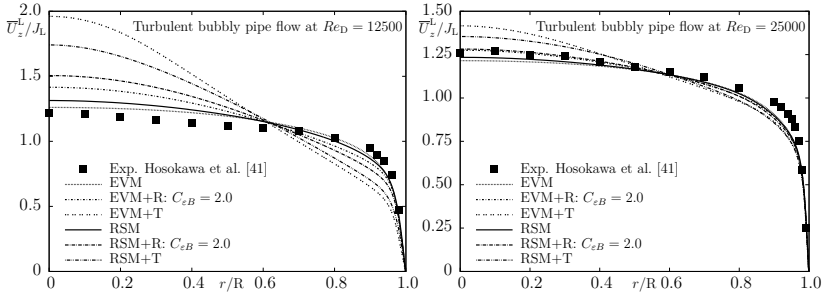

(a) $Re_D = 12500$ (b) $Re_D = 25000$

Figure 5.20: Computation of the normalized axial liquid velocity by using both baseline RANS models with additionally utilized BIT models for the bubbly flow in a vertical pipe at two different Reynolds numbers

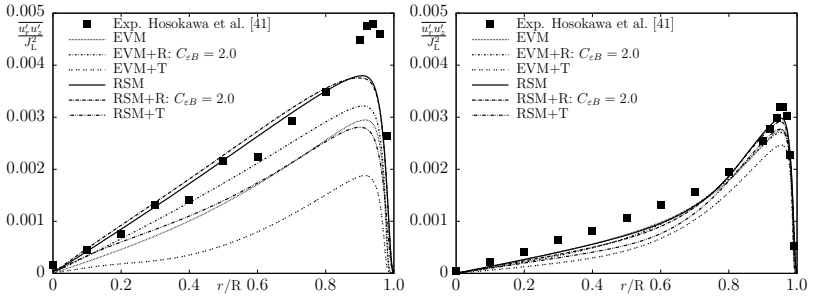

(a) $Re_D = 12500$ (b) $Re_D = 25000$

Figure 5.21: Computation of the normalized turbulent shear stress by using both baseline RANS models with additionally utilized BIT models for the bubbly flow in a vertical pipe at two different Reynolds numbers

The resulting relative velocities between both phases under the influence of BIT models are shown in Fig. 5.22. It can not be determined which of the obtained solution represents an improvement and which not. As it is the case for the previous results, the model by Troshko and Hassan [105] exhibits the strongest deviation from the baseline expression. The different behavior can be explained by the deviating distributions of α_{G}, shown in Figs. 5.15 and 5.16 for the different models, influencing the drag force. A possible explanation why none of the BIT models determine the increased peak value of u_z' represents the excessive lowering of the relative velocity close to the wall. This leads to an underestimation of S_k in these areas.

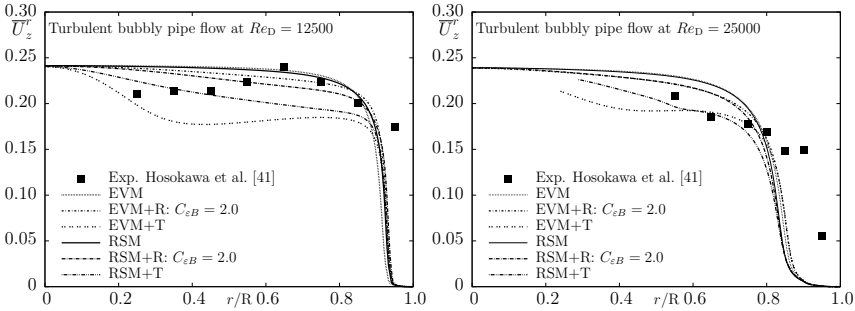

(a) $Re_{\mathrm{D}} = 12500$ (b) $Re_{\mathrm{D}} = 25000$

Figure 5.22: Computation of the axial relative velocity (in m/s) by using both baseline RANS models with additionally utilized BIT models for the bubbly flow in a vertical pipe at two different Reynolds numbers

As a conclusion, it can be stated that the usage of BIT models leave an ambivalent impression. It is evident that for bubbly flow computations within the RANS modeling framework, such models are actually the only available choice of capturing the modulation of the single-phase shear induced turbulence towards the turbulence in a corresponding two-phase flow. But on the other hand these models possess the ability to influence certain flow fields in a non-acceptable manner as it is especially the case for $\overline{U}_z^{\mathrm{L}}$. Concerning the present investigated turbulence models, the proposal by Rzehak and Krepper [89] seems to be a promising choice and should be tested against other bubbly pipe flows. It seems that the RSM is slightly more accurate when adapting a BIT model.

Performance of the scale-resolving method

In a next step, the eddy-resolving simulations are performed on the numerical meshes listed in tab. 5.2. These computations have been done with the IIS-RSM, since using the originally proposed IS-RSM leads to diverging simulations in any case, even for comparatively small amounts of CDS such as $\gamma = 0.95$. By using the IIS-RSM, the usage of CDS is feasible for this scale-resolving method within the TFM and numerical robustness is guaranteed. Again, the scale-resolving simulations are started from uniform initial conditions and as it is the case for the corresponding single-phase flow simulations, the time discretization is done with the second order BDF (Eq. (2.15)) and an adaptive time stepping method assuring that $Co < 0.8$.

Special attention needs to be paid to the utilization of the interfacial forces. Here M_i^{L} is incorporated into the momentum equations via Eq. (4.19) instead of Eq. (4.18) since phase inversions and high gradients of α_{G} can occur in the present simulations. As mentioned in Chapter 4.1, the turbulent dispersion force is thereby neglected since these gradients introduce numerical instabilities for $M_{\mathrm{td},i}^{\mathrm{L}}$. Fortunately, the modeled amount of k is significantly reduced for the IIS-RSM simulations in comparison to the RANS computations, whereby k in the modeled expression for $M_{\mathrm{td},i}^{\mathrm{L}}$ would anyway decrease considerably. The swarm effect by Legendre and Magnaudet [62] is only respected for the drag force content in Eq. (4.19) that assumes air as the dispersed phase. For $Re_{\mathrm{D}} = 12500$ the lift force is set to zero as it is the case for the RANS computations and for $Re_{\mathrm{D}} = 25000$ the value of $C_{\mathrm{l}} = 0.1$ is chosen.

While the above approach allows to perform the present simulations, it is linked to some uncertainties. The validity of the utilized interfacial force models over the whole range of α_{G} from zero to one is of course questionable and for the drag force only insufficiently captured by Eq. (4.13). For the lift and virtual mass force no swarm effects are respected, which is mainly due to the small amount of available models, with the model by Rusche [88] being the only known for the lift force. An example for such an area where the present modeling approach for M_i^{L} is questionable can be seen in the center of the pipe as shown in Fig. 5.23a, where the value of α_{G} reaches 0.6. It could even be discussed if such areas of the flow field should be better captured by VOF with the surface tension included. But besides all these questionable aspects, a realistic time averaged $\langle \alpha_{\mathrm{G}} \rangle$ field is achieved as it can be seen in Fig. 5.23.

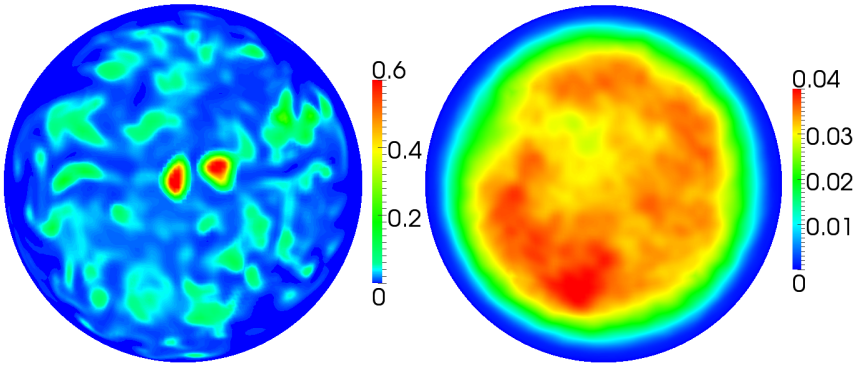

(a) Instantaneous α_G field (b) Time averaged $\langle \alpha_G \rangle$ field

Figure 5.23: Snapshots of the instantaneous and time averaged volume fraction of the gas phase with the IIS-RSM at $Re_D = 12500$

Unfortunately, the usage of the virtual mass force introduced undesired features into the simulations, which are velocity scatterings in the areas of the coupled in- and outlet. The reason for this behavior could not be determined. One the other hand, it is clear that in an eddy-resolving simulation the virtual mass force has to play a certain role. This is because of the turbulent fluctuations which are strongly increasing the material derivative of the velocity fields in Eq. (4.16). The influence of the virtual mass force does thereby not depend so much on the value for C_{vm} as it can be seen in Fig. 5.24, but more on simply being considered. Since the previously mentioned scattering of the velocity field is surely an unwanted numerical aspect and it is unclear how much of the influence of the virtual mass force actually stems from this issue, it is decided to neglect this force in the following presented results. These adjustments finally lead to the resulting $\langle \alpha_G \rangle$ distributions shown in Fig. 5.25. The qualitative trend is captured by the IIS-RSM for both cases, by accumulating the gas phase in the center of the pipe in Fig. 5.25a and forming a wall peak in Fig. 5.25b. But clearly, the resulting fields differ considerably to the ones obtained with the baseline RANS models. For $Re_D = 12500$ the accumulation of gas in the center of the pipe is slightly overestimated, which would suggest to respect the lift force with a comparable small value for C_l. Unfortunately, a simulation with $C_l = 0.1$ immediately leads to a wall peak behavior with an maximum value of around $\langle \alpha_G \rangle = 0.11$. The same behavior occurs if the lift force coefficient for the simulation with the higher Reynolds number

is raised from $C_\mathrm{l} = 0.1$ towards 0.2, which would immediately result in a significant overestimation of the $\langle \alpha_\mathrm{G} \rangle$ peak value. Possible improvements of the results could be achieved by a consideration of the virtual mass force without introducing the mentioned numerical problems and the possible consideration of swarm effects for the lift force.

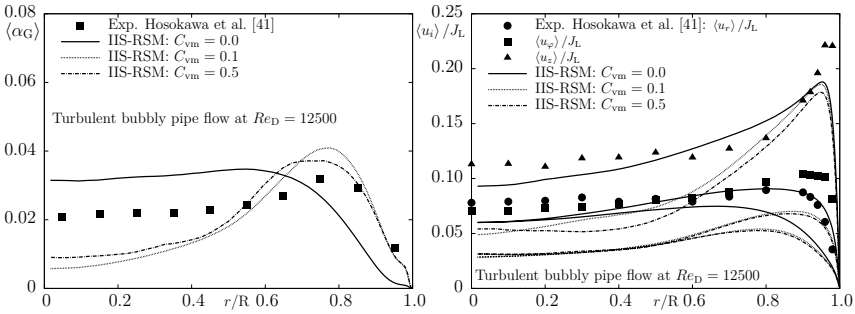

(a) $\langle \alpha_\mathrm{G} \rangle$ at $Re_\mathrm{D} = 12500$ (b) $\langle u_i \rangle$ at $Re_\mathrm{D} = 12500$

Figure 5.24: Influence of the virtual mass force coefficient on the IIS-RSM results in a bubbly pipe flow at $Re_\mathrm{D} = 12500$

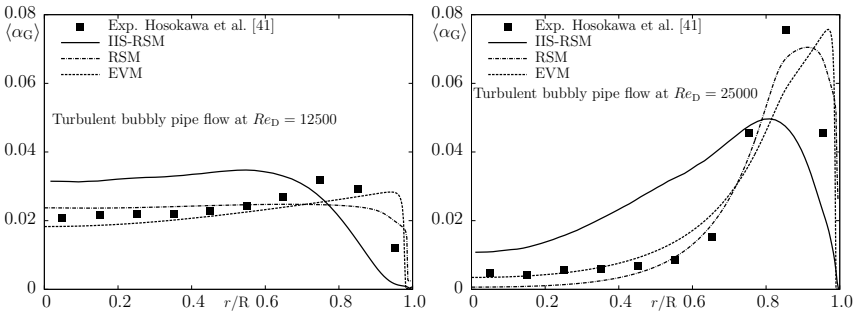

(a) $Re_\mathrm{D} = 12500$ (b) $Re_\mathrm{D} = 25000$

Figure 5.25: Computation of the gas volume fraction by using both baseline RANS models and the IIS-RSM for the bubbly flow in a vertical pipe at two different Reynolds numbers

The resulting averaged axial liquid velocity in Fig. 5.26 shows that the IIS-RSM predicts comparable results to the baseline RSM, while giving considerably different results for $\left\langle \overline{U}_z^r \right\rangle$, as seen in Fig. 5.27.

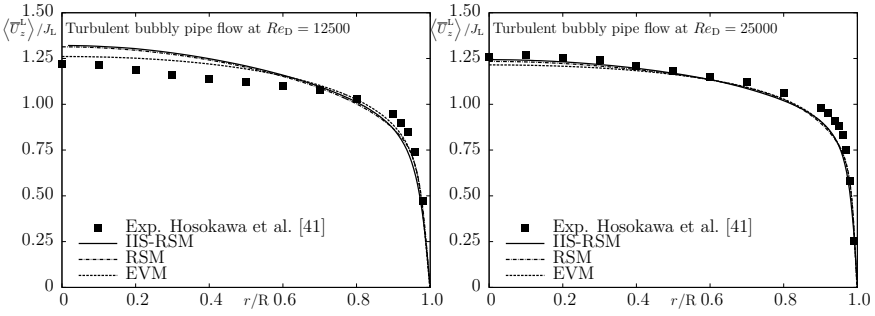

(a) $Re_D = 12500$ (b) $Re_D = 25000$

Figure 5.26: Computation of the normalized axial liquid velocity by using both baseline RANS models and the IIS-RSM for the bubbly flow in a vertical pipe at two different Reynolds numbers

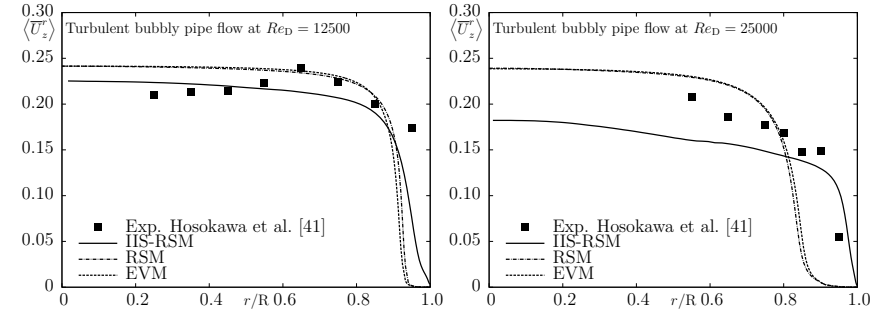

(a) $Re_D = 12500$ (b) $Re_D = 25000$

Figure 5.27: Computation of the axial relative velocity (in m/s) by using both baseline RANS models and the IIS-RSM for the bubbly flow in a vertical pipe at two different Reynolds numbers

This represents an improvement in some areas of the flow, as in the center of the pipe and close to the wall for $Re_\mathrm{D} = 12500$, as well as close to the wall for $Re_\mathrm{D} = 25000$. Unfortunately, there is no experimental data for the latter one concerning $\left\langle \overline{U}_z^r \right\rangle$ in the center of the pipe. The difference between the IIS-RSM simulations and the RANS computations can be mainly explained with the deviating α_G which leads to different resulting values for the drag force. Hence, a higher value of α_G results in a higher drag force leading to a reduced $\left\langle \overline{U}_z^r \right\rangle$.

Fig. 5.28 shows that the IIS-RSM is in general capable of reproducing the turbulent intensities $\langle u_i \rangle = \sqrt{\langle u_i^2 \rangle}$ in a qualitatively good agreement. Especially the prediction of $\langle u_z \rangle$ is considerably improved in comparison to the baseline RSM without the correct determination of its peak value for both Reynolds numbers. The scale-resolving method fails to predict the correct near-wall behavior for $\langle u_r \rangle$ and $\langle u_\varphi \rangle$. This is on the other hand not surprising, since the IIS-RSM on the present numerical grids has these weaknesses already in the corresponding single-phase flows, as shown in Fig. 5.5. In the center of the pipe the IIS-RSM underestimates the reference data for both cases, with an overall improvement for the lower Reynolds number in comparison to the baseline RSM. Almost the same statements can be made for the resulting $\langle k \rangle$ distribution in Fig. 5.29. The IIS-RSM gives superior results for both the turbulent intensities and k compared to the baseline RANS models. Unfortunately, this only partly applies for the turbulent shear stress $\langle u_r u_z \rangle$ shown in Fig. 5.30 for $Re_\mathrm{D} = 12500$, whereby the peak value is actually increased towards a more realistic value, but unfortunately not close enough to the wall. For the higher Reynolds number, the IIS-RSM leads to a slightly better agreement in the center areas of the pipe.

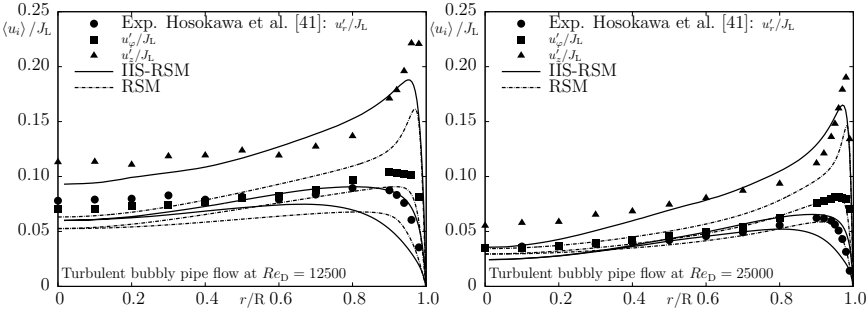

(a) $Re_D = 12500$ (b) $Re_D = 25000$

Figure 5.28: Computation of the normalized turbulent intensities by using the RSM and the IIS-RSM for the bubbly flow in a vertical pipe at two different Reynolds numbers

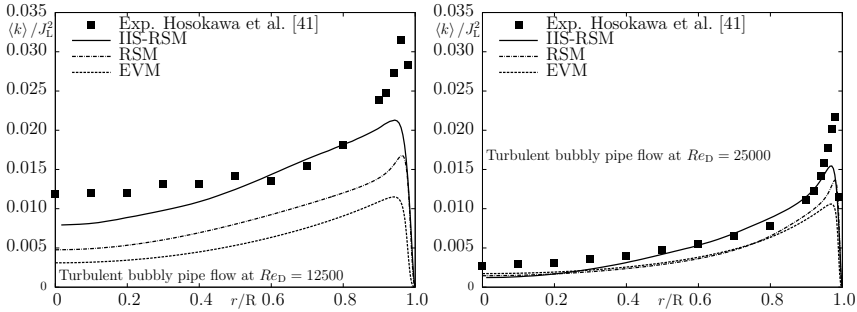

(a) $Re_D = 12500$ (b) $Re_D = 25000$

Figure 5.29: Computation of the normalized turbulent kinetic energy by using both baseline RANS models and the IIS-RSM for the bubbly flow in a vertical pipe at two different Reynolds numbers

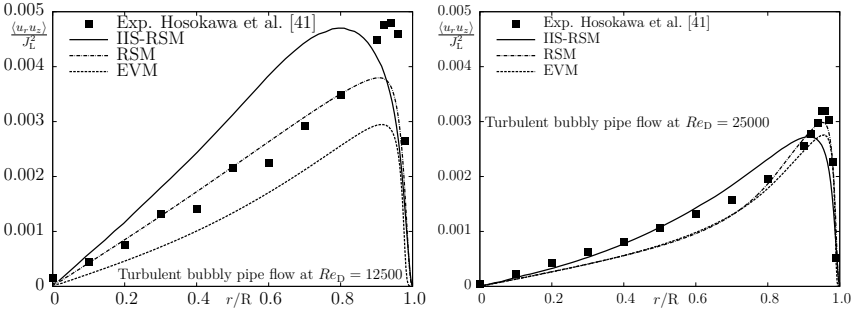

(a) $Re_D = 12500$ (b) $Re_D = 25000$

Figure 5.30: Computation of the normalized turbulent shear stress by using both baseline RANS models and the IIS-RSM for the bubbly flow in a vertical pipe at two different Reynolds numbers

Besides the existing uncertainties with regard to the utilized interfacial forces, promising results can be obtained by applying the IIS-RSM. Even without deriving major modifications of the interfacial force models, it is possible to obtain reasonable results which are not including major drawbacks as it is the case for of the presented RANS computations with BIT models. At least, since the turbulent dispersion force is not respected here, these uncertainties are now mainly dealing with the realization of possible swarm effects for the lift force and the numerical stabilization of the virtual mass force. But still, the influence of the interfacial force modeling represents a major uncertainty factor which should be further investigated in future studies.

6 Flow configuration II: Flow through a sudden expansion in a vertical pipe

The present chapter deals with the simulation of a flow through a sudden expansion in a vertical pipe with water as the continuous liquid phase and finely dispersed air bubbles. This test case represents a logical complement to the previously presented fully developed pipe flow computations, which actually describe the flow conditions before the expansion, towards a more complex problem including large separation zones. One set of a corresponding single- and two-phase flow is analyzed here, based on the experimental reference data by Bel Fdhila [9], given in cylindrical coordinates, who investigated varying flow rates for both phases. Statistically averaged data was thereby measured for α_{G}, $\overline{U}_z^{\mathrm{L}}$, $\overline{U}_r^{\mathrm{L}}$, u_z', u_r' and $\overline{u_r' u_z'}$. Unfortunately, no data for the velocity of the dispersed gas-phase is reported, whereby the relative velocity cannot be compared as it is done for the pipe flows in the previous chapter. The presently encountered experimental conditions are listed in tab. 6.1.

Table 6.1: Sudden Expansion test case by Bel Fdhila ([9] and [10])

J_{L}	J_{G}	$\alpha_{\mathrm{G}}^{\mathrm{ave}}$	d_{G}
1.57 m/s	0.3 m/s	12 %	2 mm

The superficial velocities and $\alpha_{\mathrm{G}}^{\mathrm{ave}}$ are specified in the pipe before the sudden expansion with an inner diameter of $\mathrm{D}_1 = 0.05$ m, which expands to $\mathrm{D}_2 = 0.1$ m resulting in an expansion ratio of $1:2$. To define the material properties, it is assumed that the experiments have been done at atmospheric pressure conditions and a room temperature of 20 °C resulting in a bulk Reynolds number before the expansion of $Re_{\mathrm{D}_1} = J_{\mathrm{L}}\mathrm{D}_1/\nu_{\mathrm{L}} = 78500$. Again, the axial component of the gravitational vector is set to $g_z = -9.81$ m/s. It seems that the diameter of the air bubbles is not given by Bel Fdhila [9], but set to the value shown in tab 6.1 by Bel Fdhila and Simonin [10]. Rusche [88] also adopted this value. Clearly, the here investigated Reynolds number as well as $\alpha_{\mathrm{G}}^{\mathrm{ave}}$ in the pipe before the expansion are considerably

higher than their equivalents in Chapter 5 and it has to be analyzed how the present models will be capable in handling these significantly different two-phase flow conditions.

This particular two-phase flow has been used by several authors for the validation of their computations within the TFM framework. As it is for the bubbly pipe flows, the majority of these investigations utilized the standard high Reynolds number $k-\varepsilon$ model by Launder and Spalding [61] to capture the turbulence in the continuous liquid phase (e.g. done by Rusche [88], Behzadi et al. [8] and Oliveira and Issa [77]). On the other hand, the only known investigation with a SMC model is the work by Cokljat et al. [15], whereby a BIT model was additionally utilized.

As an additional reference for the single-phase flow computations serve the experimental investigations of a sudden expansion by Dellenback et al. [23], enhancing the validation. Thereby, three different cases are investigated at $Re_{\mathrm{D}_1} = 30000, 60000$ and 100000 with an expansion ratio of $1 : 1.94$, which is in a comparable range to the one investigated by Bel Fdhila [9]. The experimental data is not directly taken from Dellenback et al. [23], but from the data provided by Dellenback for [31], containing statistically averaged data for $\overline{U}_z^{\mathrm{L}}$, u_z' and u_φ'. Unfortunately, the respective J_{L} are not reported, whereby a normalization with the bulk velocity cannot be made.

A schematic description of the test case geometry is shown in Fig. 6.1. Measured data exists at different axial positions in the geometry with $z = 0$ being the position of the sudden expansion. The experimental data is given over the radial coordinate and is homogeneous in the circumferential direction. For the test case by Bel Fdhila [9], measurements are available at $z/\mathrm{D}_1 = 1.4$, 2.6, 3.6, 5, 6.4 and at one position before the expansion at $z/\mathrm{D}_1 = -0.4$. According to Bel Fdhila [9] fully developed flow conditions are achieved at that point. Slightly different axial measurement positions have been investigated by Dellenback et al. [23]. The ones considered here are located at $z/\mathrm{D}_1 = 0.5$, 1, 2, 3, 4 and 6 with one position before the expansion at $z/\mathrm{D}_1 = -0.5$. Unfortunately, because of the slightly different axial measurement positions, both data sets cannot be included into the same figures. Concerning the Bel Fdhila [9] data set the results for $\overline{U}_z^{\mathrm{L}}$, $\overline{u_z' u_r'}$ u_z' and u_r' are presented. Each of the resulting flow fields is normalized with its respective centerline velocity $U_c = \overline{U}_z^{\mathrm{L}}\,(r = 0, z < 0)$ before the expansion. Such a test case has not been investigated via DNS so far, meaning

that the present investigations cannot be as analyzed in such detail as the previously presented pipe flows, especially concerning the near-wall areas.

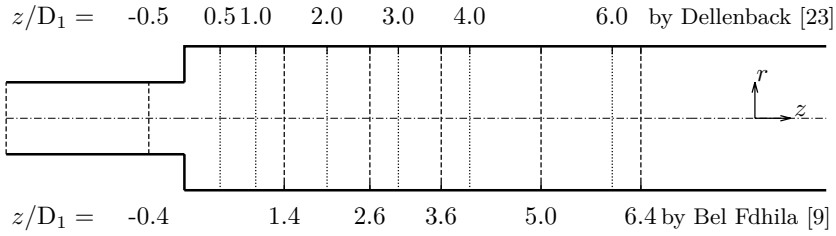

Figure 6.1: Geometry of the sudden expansion test case with the axial measurement planes by Bel Fdhila [9] and Dellenback et al. [23]

As it is done in Chapter 5, the incompressible single-phase flow investigations are presented first and followed by the two-phase flow ones. The present RANS computations lead directly to steady state solutions meaning that $\langle \Phi \rangle = \overline{\Phi}$ is achieved and the turbulent quantities consist completely of the modeled part. The RANS models by Jakirlić and Maduta and by Launder and Sharma are again denoted by RSM and EVM. For the latter one, the turbulent stresses are computed by using Eq. (3.8).

6.1 Single-phase flow computations

The present single-phase flow investigations represent the first computations of a sudden expansion in a pipe with the RSM and the IIS-RSM so far. Here, the IIS-RSM is directly used instead of the IS-RSM because of the superior results shown in Chapter 5 in comparison to the originally proposed scale-resolving formulation. Hereby is the CDS used for the discretization of the convective term in the momentum equation of the liquid phase. The time discretization and the time stepping method are done by using the same numerical setup as presented in Chapter 5.1.

These RANS computations are performed on a two dimensional axis-symmetric solution domain, with orthogonal hexaeder cells. The symmetry axis is located at $r = 0$, the outlet of the domain at $z/\mathrm{D}_1 = 12.5$ and the inlet at $z/\mathrm{D}_1 = -0.5$. In radial direction, this mesh consists of 40 cells over R_1 and 100 cells over R_2 with refined cells towards the solid walls to resolve the viscous sub-layer. For the discretization in axial direction, 40 respectively 200 cells are used before and after the expansion. This results in an overall cell number of 25500. An intensive grid study, including doubling the number of cells after the expansion, showed that the present mesh leads to a grid independent solution. Prior to the evaluation of the entire expansion, fully developed pipe flow computations (equivalent to the ones in Chapter 5) at every particular Re_{D_1} number are carried out for both RANS models. The resulting flow fields are then prescribed as fixed inlet conditions at $z/\mathrm{D}_1 = -0.4$ respectively -0.5. For the RSM an additional source term introduced by Hanjalić and Jakirlić [34] has to be incorporated into the length scale supplying ω^h-equation to avoid the so-called back-bending behavior of the mean dividing streamline in the areas around the reattachment point, representing a well-known deficiency of SMC models. This term reads

$$S_l = \max\left\{\left[\left(\frac{1}{2.5}\frac{\partial l}{\partial x_n}\right)^2 - 1\right]\left(\frac{1}{2.5}\frac{\partial l}{\partial x_n}\right)^2, 0\right\} A\omega^h\omega^h \qquad (6.1)$$

with $\partial/\partial x_n$ representing the normal wall gradient and l the turbulent length scale defined by Eq. (3.14).

In order to perform the scale-resolving simulations, a fully three dimensional grid has to be used. To obtain the statistically averaged flow quantities of interest, the homogeneity of the time averaged results in circumferential direction is used for a spatial averaging in every investigated measurement plane. For all investigated Re_{D_1} numbers, the one by Bel Fdhila [9] and the three by Dellenback et al. [23], the same numerical mesh is utilized ranging from the inlet at $z/\mathrm{D}_1 = -2.5$ until the outlet at $z/\mathrm{D}_1 = 12.5$. A different inlet boundary condition in comparison to the RANS computations is utilized for the scale-resolving simulations. An artificial correction to maintain a constant volume flow rate, corresponding to the respective Re_{D_1} number, is imposed in the periodic area between $z/\mathrm{D}_1 = -2.5$ and $z/\mathrm{D}_1 = -0.5$. This approach is based on the work of Baba-Ahmadi and Tabor [4] assuring a fully developed instantaneous turbulent flow field before the expansion, as it is also achieved by so-called precursor simulations.

As it is for the pipe flow simulations, no artificially imposed turbulent fluctuations are therefore needed. For the design of the mesh, an o-grid arrangement in the center area of the pipe is utilized with refined cells in radial direction towards the solid walls to resolve the viscous sub-layer. The same statements about the influence of the cell numbers in a scale-resolving simulation stated in Chapter 5.1 are valid here and therefore not repeated. The selected fully three dimensional mesh consists of $110 \times 160 \times 110$ and $250 \times 160 \times 180$ cells before and after the expansion, with $N_z \times N_\varphi \times N_r$ being the respective numbers in streamwise and circumferential direction and over the pipe diameter. This results in an overall cell number of approximately four million cells. For the simulation at $Re_{\mathrm{D}_1} = 30000$, the first grid points are everywhere below $(\mathrm{R} - r)^+ < 1$. For the higher Reynolds numbers this value can rise up to 5 in some areas after the expansion, which should be considered as a limiting value for the IIS-RSM in terms of numerical robustness and modeling accuracy. A snapshot of the instantaneous streamwise velocity field for the simulation at $Re_{\mathrm{D}_1} = 30000$ can been seen in Fig. 6.2. It is clearly visible that the IIS-RSM is resolving the turbulent structures before and after the expansion.

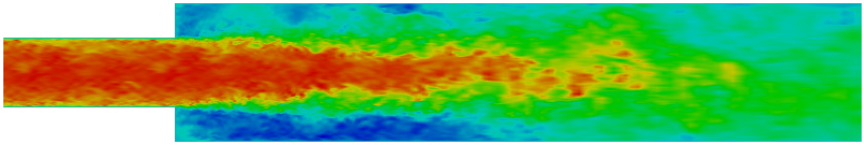

Figure 6.2: Snapshot of the instantaneous streamwise velocity field $\overline{U}_z$ at $Re_{\mathrm{D}_1} = 30000$

While comparable scale-resolving simulations for pipe flows are already quite hard to find, only two numerical investigations with LES could be found for the present sudden expansion test case. Those have been done by Baba-Ahmadi and Tabor [4] and Schlüter et al. [94] for the experimental investigations by Dellenback et al. [23] at $Re_{\mathrm{D}_1} = 30000$. In both simulations distinct coarser numerical grids were utilized, which can be on the one hand explained by the fact that those grids were constructed to give convincing results only for $Re_{\mathrm{D}_1} = 30000$ and not for the higher Reynolds numbers also investigated here. On the other hand, these scale-resolving

simulations are not resolving the viscous sub-layer, leading to strong reduction of the resulting cell numbers in comparison to the present low Reynolds number simulation. Nevertheless, the present mesh is not excessively increasing the cell numbers compared to the former mentioned references and appropriate for the intended numerical investigations.

By comparing the cell numbers before the expansion ($110 \times 160 \times 110$) with the ones stated in tab. 5.2 for considerably lower Reynolds numbers, it is obvious that the normalized cell sizes will not be in the same order as for the pipe flow simulations. Clearly, a numerical mesh providing such small Δx_i^+ values as in tab. 5.2 for the case with $Re_{\mathrm{D}_1} = 100000$ would easily exceed every justifyable numerical effort for the present investigations. This also means that the statistically averaged results obtained with the IIS-RSM for the fully developed pipe flow before the expansion will not be as accurate as in Chapter 5, which have shown a perfectly reproduced log-law. It should be analyzed if these circumstances are influencing the simulations of the sudden expansion in an undesired manner.

The results for the single-phase flow simulations at $Re_{\mathrm{D}_1} = 78500$ in comparison to the experimental reference data by Bel Fdhila [9] are shown in Figs. 6.3 and 6.4. Therefore, the axial velocity, the turbulent intensities in the axial and the radial direction and the turbulent shear stress are chosen. A comparison between the computational results and experimental data for the normalized axial velocity in Fig. 6.3 exhibit an overall good agreement, with the resulting velocity fields for all three models ranging within the same order. However, there are a few non-negligible differences which are mostly located in the area around the centerline downstream from $z/\mathrm{D}_1 = 3.6$ on. It can be clearly seen that all three models considerably overestimate the normalized axial velocity $\left\langle \overline{U}_z^{\mathrm{L}} \right\rangle$ in these areas. Especially for the RSM as well as for the IIS-RSM these discrepancies are surprising, since both models are supposed to be capable of giving a good agreement in such a flow configuration with a fixed separation point. For the IIS-RSM a possible explanations would be an insufficient mesh resolution after the expansion or the previously discussed deficiencies in the pipe before the expansion.

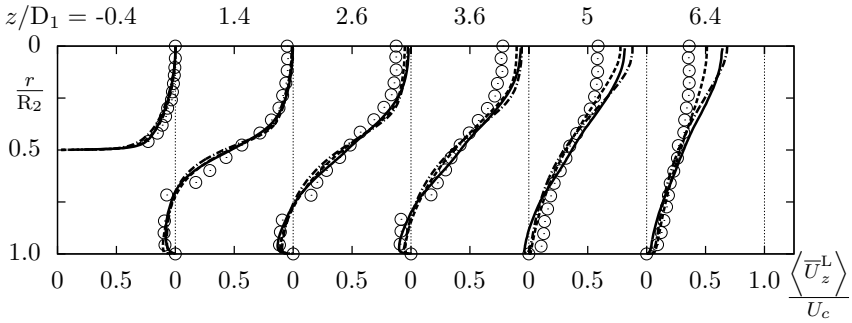

Figure 6.3: Computation of the normalized axial velocity by using the IIS-RSM (———), RSM (–·–·–) and EVM (-------) for the single-phase flow through the sudden expansion by Bel Fdhila [9] at $Re_{D_1} = 78500$ (exp. ∘)

However, a comparison between the calculated and the experimental turbulent quantities shows further unexpected differences. The axial intensities $\langle u_z \rangle = \sqrt{\langle u_z^2 \rangle}$ in Fig. 6.4b exhibit evident deviations, especially around the centerline. All three models considerably underestimate the increasing values in this area until $z/D_1 = 5.0$. Also, the resulting intensities in the near-wall region of the re-circulation zone are not in a qualitative agreement with the reference data. A slightly superior agreement between the numerical results and the experimental data is achieved for $\langle u_r \rangle = \sqrt{\langle u_r^2 \rangle}$ as shown in Fig. 6.4c. The RSM and the IIS-RSM are hereby giving a slightly improved agreement with the experiment than the EVM. For the turbulent shear stress the most pronounced deviations for all three models occur right after the expansion, while being in an overall better agreement with the experimental data further downstream. Overall, the weak performance of the utilized models for the present flow configuration is an unpleasant surprise, since Maduta [70] achieved very good results for the comparable flow over a backward facing step with both the RSM and the scale-resolving method. Of course, this case is not entirely comparable with the present sudden expansion in terms of Reynolds number and geometry.

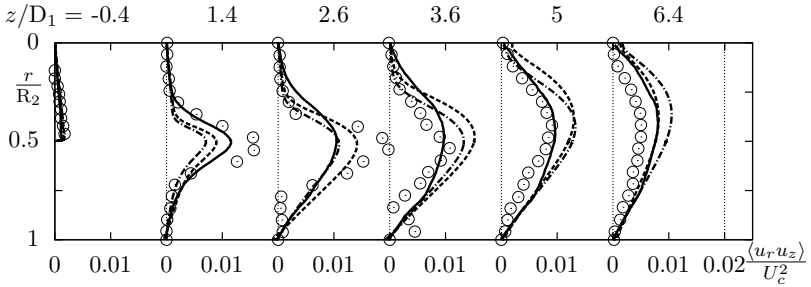

(a) Normalized averaged turbulent shear stress at $Re_{D_1} = 78500$

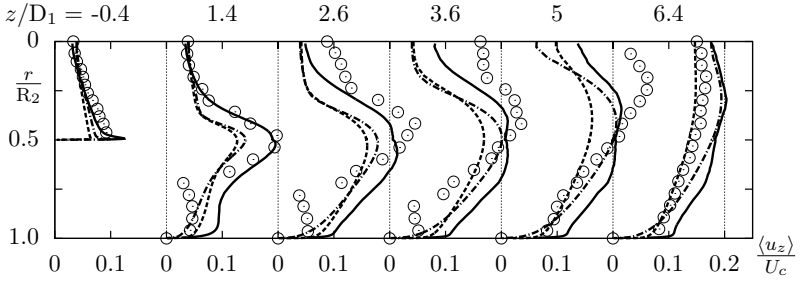

(b) Normalized averaged axial turbulent intensity at $Re_{D_1} = 78500$

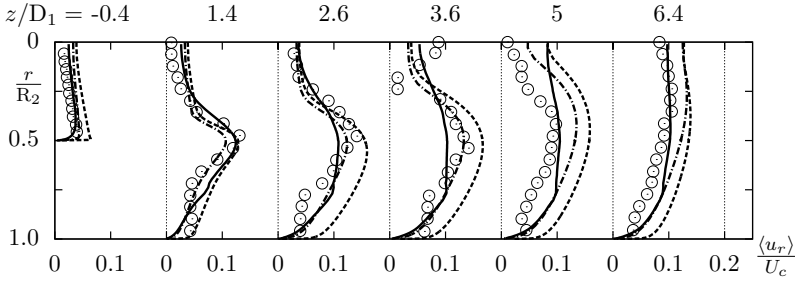

(c) Normalized averaged radial turbulent intensity at $Re_{D_1} = 78500$

Figure 6.4: Computation of the normalized turbulent quantities by using the IIS-RSM (———), RSM (–·–·–) and EVM (- - - - - - -) for the single-phase flow through the sudden expansion by Bel Fdhila [9] at $Re_{D_1} = 78500$ (exp. ∘)

Fortunately, these circumstances can be further analyzed through the available experimental data by Dellenback et al. [23] at three different Reynolds numbers. As it is shown in Figs. 6.5-6.7 an overall significantly better agreement with the experimental reference data is achieved for all three models in comparison to the previously presented results. This statement is valid for all three considered Reynolds numbers. Concerning $\left\langle \overline{U}_z^{\mathrm{L}} \right\rangle / U_c$, all three models give an almost perfect agreement with the experimental data at every position. The normalized experimental data for these three cases are virtually collapsing to one line and so do the numerical results. Only the RSM slightly differs from the experimental data at $z/\mathrm{D}_1 = 6$. Strongly improved are the resulting $\langle u_z \rangle$ distributions shown in Fig. 6.6 in comparison to Fig. 6.4b. This is actually not due to essentially different numerical results, but due to the fact that the experimental data does not indicate the increased values in the areas around the centerline as it is the case for the data by Bel Fdhila [9]. But not only this area is well captured by all three models, also $\langle u_z \rangle$ in the recirculation zone close to the solid wall is in a very good agreement with the experiment. The IIS-RSM is thereby even capable of capturing the steep turbulent intensity increase in the near-wall region. Nearly the same findings are valid for the circumferential turbulent intensity $\langle u_\varphi \rangle = \sqrt{\langle u_\varphi^2 \rangle}$ in Fig. 6.7, whereby all three models show an overall very good performance at all investigated Reynolds numbers. For the IIS-RSM the present results indicate that the chosen grid resolution is fine enough for all three cases, implying that for the lowest Reynolds number considerably less cells numbers would also lead to sufficiently accurate results. It is also clear that the spatial resolution before the expansion is fine enough to give accurate inflow conditions before the expansion, even if the local results in these areas are not as accurate as for the pipe flows in Chapter 5. These results lead to the question why there is such a discrepancy between the Bel Fdhila [9] experiment and the one by Dellenback et al. [23]. Since the measured data is not available at the same axial positions, a direct comparison to illustrate the occurring deviations cannot be made. By taking $\langle u_z' \rangle$ as an example, it cannot be excluded that the high values measured by Bel Fdhila [9] at $z/\mathrm{D}_1 = 5$ are actually reached, since this position is not covered by Dellenback et al. [23] at $z/\mathrm{D}_1 = 4$ and $z/\mathrm{D}_1 = 6$. Other features like the discrepancies between the centerline values of $\left\langle \overline{U}_z^{\mathrm{L}} \right\rangle / U_c$ are even more questionable. Hence, the substantial uncertainties are not concerning the performance of the present turbulence models, but the validity of the experimental data by Bel Fdhila [9].

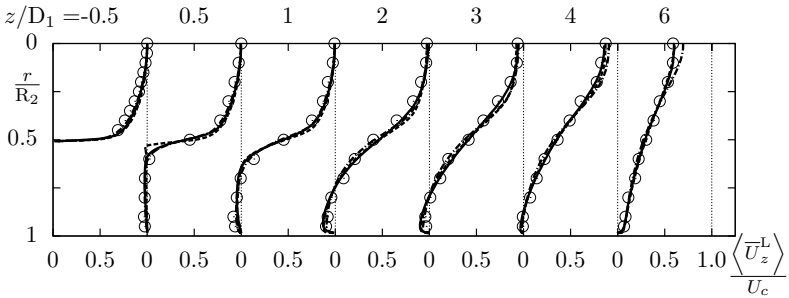

(a) $Re_{\mathrm{D}_1} = 30000$

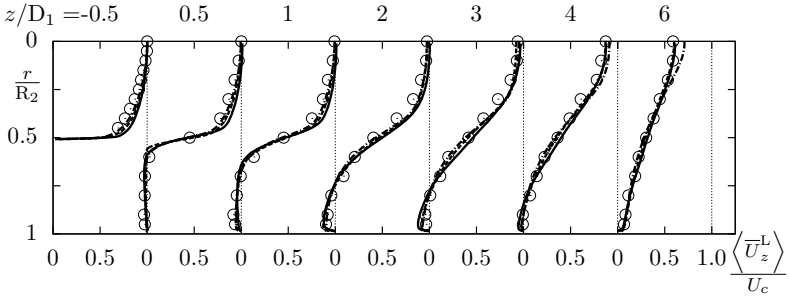

(b) $Re_{\mathrm{D}_1} = 60000$

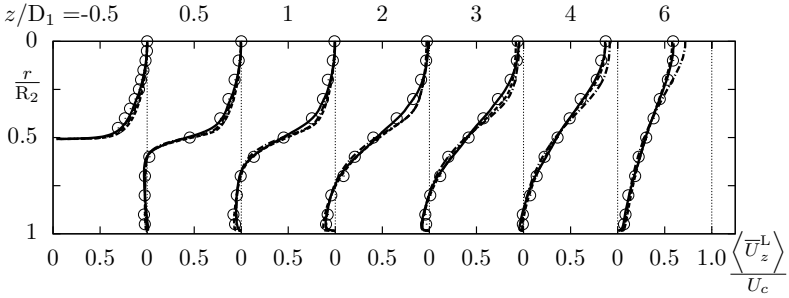

(c) $Re_{\mathrm{D}_1} = 100000$

Figure 6.5: Computation of the normalized axial velocity over a range of Reynolds numbers by using the IIS-RSM (———), RSM (–·–·–·) and EVM (-------) for the single-phase flow through the sudden expansion by Dellenback et al. [23] (exp. ∘)

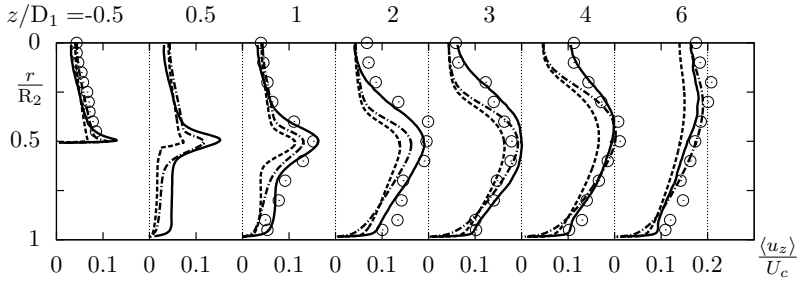

(a) $Re_{D_1} = 30000$ (no exp. data available at $z/D_1 = 0.5$)

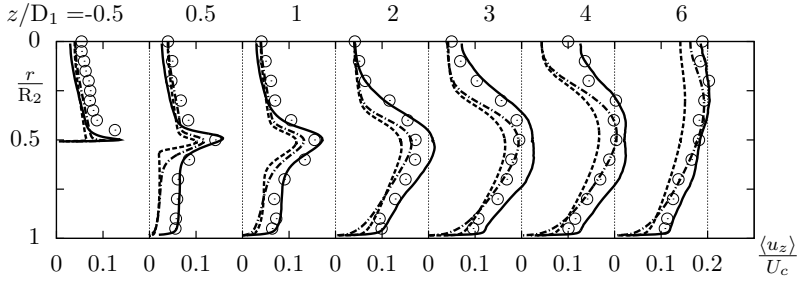

(b) $Re_{D_1} = 60000$

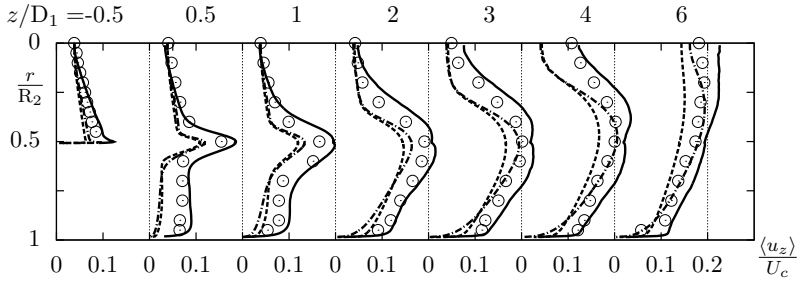

(c) $Re_{D_1} = 100000$

Figure 6.6: Computation of the normalized axial turbulent intensities over a range of Reynolds numbers by using the IIS-RSM (———), RSM (–·–·–) and EVM (-------) for the single-phase flow through the sudden expansion by Dellenback et al. [23] (exp. ○)

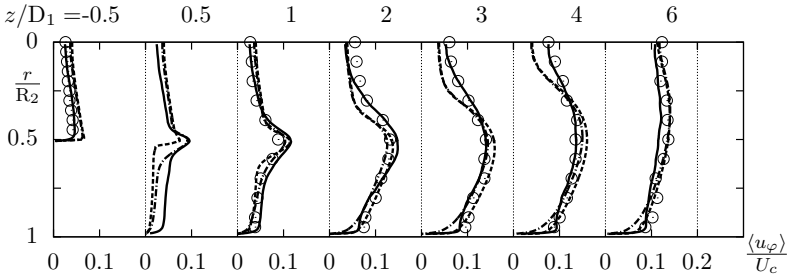

(a) $Re_{D_1} = 30000$ (no exp. data available at $z/D_1 = 0.5$)

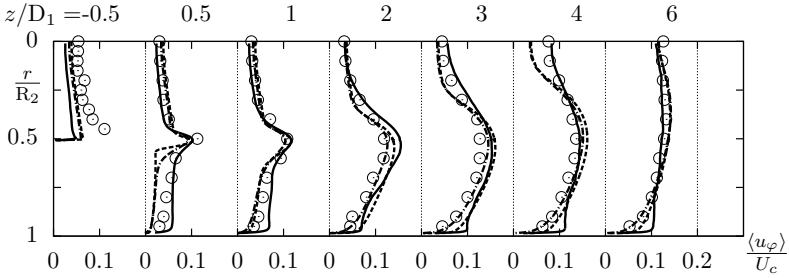

(b) $Re_{D_1} = 60000$

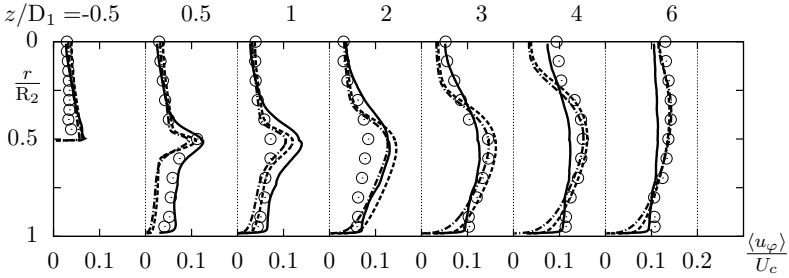

(c) $Re_{D_1} = 100000$

Figure 6.7: Computation of the normalized circumferential turbulent intensities over a range of Reynolds numbers by using the IIS-RSM (———), RSM (–·–·–) and EVM (- - - - - - -) for the single-phase flow through the sudden expansion by Dellenback et al. [23](exp. ○)

6.2 Two-phase flow computations

This section presents the corresponding two-phase flow computations for the case by Bel Fdhila [9] shown in tab. 6.1. Clearly, the previously discussed uncertainties in the measured reference data lead to the question how useful these two-phase flow investigations actually are. But since the experimental data by Bel Fdhila [9] represents a unique series of investigations for bubbly flows and the only chance to validate the present turbulence models within the TFM for a complex two-phase flow with large separation zones, these investigations are still carried out. Nevertheless, the uncertainties concerning the validity of the reference data have to be kept in mind. The results for the realized RANS computations are shown and discussed first, while a critical comment about the attempted eddy-resolving simulations with the IIS-RSM follows afterwards.

To perform these RANS computations, the same axis-symmetric grid is used as for the previously presented single-phase flow computations. As it is the case for the investigated pipe flows in Chapter 5, the TFM is capable of dealing with the occurring grid refinements towards the solid walls. To incorporate the interfacial momentum transfer term, Eq. (4.18) is utilized since no phase inversion occurs here. Previously to the computation of the sudden expansion, a fully developed two-phase flow in the pipe before the expansion has to be created to serve as the inflow conditions. Adopting the procedure by Rusche [88] who interpolated the experimental data at the inlet onto the numerical mesh failed for the present investigations because of occurring numerical instabilities. This is caused by the fact that low Reynolds number models are reacting very sensitive if non consistent turbulent quantities are present in the sensible areas close to the wall. Hence, fully developed two-phase pipe flow computations have to be done in a preliminary step, which should as accurately as possible represent the experimental conditions before the expansion with the main focus on the radial distribution of α_{G}. In a first step this is done with both baseline RANS models.

The essential aspects of these pipe flow computations, especially concerning the difference between the RSM and the EVM, have already been discussed in Chapter 5 and are therefore not repeated here. For the present pipe flow before the expansion, fully developed flow conditions could only be achieved with the RSM. No combination of values for C_{l} and C_{td} led to a stable solution for the EVM. Most of these realized calculations lead to an oscillating

complete accumulation of α_G in the first two cells close to the wall. It is assumed that the systematical error of an eddy-viscosity model by capturing the radial pressure distribution in Eq. (5.5) is responsible for this. The higher Reynolds number as well as the increased α_G seem to increase this error towards a level that allows no stable solutions. Since it is interesting to see how the EVM will perform in the two-phase flow computations of the sudden expansion, the inflow values obtained with the baseline RSM are also used for the EVM.

To carry out the pipe flow computations, the same setup as in Chapter 5 is used with the coefficients of the interfacial forces set to $C_{td} = 1.0$ and $C_l = 0.075$. These values assure the present wall peak behavior of α_G with its correct peak value in the pipe before the expansion as can be seen by means of the first line on the left in Fig. 6.9a. The comparison between the liquid velocity and the available turbulent intensities from the experiment are shown in Fig. 6.8 and normalized by the superficial liquid velocity J_L instead of U_c to keep the known normalizing procedure from Chapter 5. Single- and two-phase flow results are directly compared to each other.

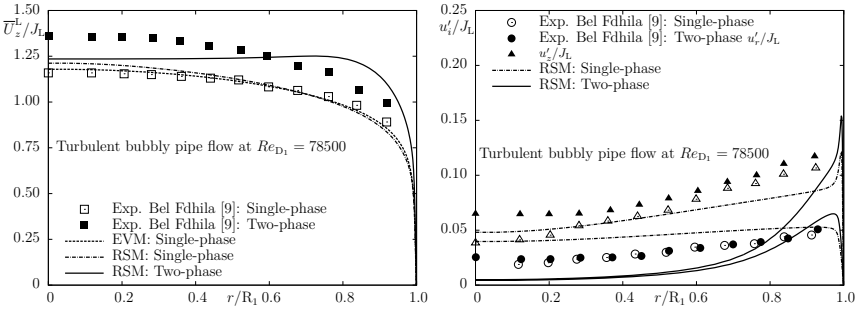

(a) $\overline{U}_z^L$ - r/R_1 distribution

(b) u_i' - r/R_1 distribution

Figure 6.8: Computation of the normalized axial liquid velocity and the turbulent intensities by using both baseline RANS models for the single-phase flow and the bubbly flow in the pipe before the expansion

It can be seen that the RSM is capable of capturing the modulation of the liquid velocity in a qualitative manner resulting in increased values over the whole pipe radius. Unfortunately, this increase is quantitatively

overestimated in the areas around $r/\mathrm{R}_1 = 0.8$ and underestimated in the center area of the pipe. An increased flattening of the velocity profile towards the symmetry axis occurs, which is not present in the experimental data. The resulting turbulent intensities shown in Fig. 6.8b (only u'_z and u'_r are available in Bel Fdhila [9]) are unfortunately not convincing, since the RSM actually predicts a decrease of the turbulent intensities within most of the pipe cross section. Instead of this, nearly the same normalized values as for the single-phase flow are expected. An explanation for this could be the falsely flattened velocity profile in the center of the pipe, whereby the turbulent production P_{ij} is heavily decreased through the reduced liquid velocity gradient. This behavior was already visible in Fig. 5.13b even tough being less pronounced. It has to be analyzed how far these shortcomings of the pipe flow computations influence the resulting flow fields after the expansion. A comparison of the wall peak behavior for u'_z cannot be done, since there is no experimental data available in the interesting areas close to the wall.

Performance of the baseline models

For the initial computations of the sudden expansion with both baseline RANS models, the lift force is neglected by following the initial procedure by Rusche [88] and the coefficient of the turbulent dispersion force is set to $C_{\mathrm{td}} = 1.0$. With these values, stable solutions for both models can be easily assured. The wall peak behavior of α_{G} and its correct determination by the baseline RSM in the pipe before the expansion can be clearly seen in Fig. 6.9a. For the resulting distributions of α_{G} after the expansion, both baseline models give comparable results with the pronounced deviation between them being located at $z/\mathrm{D}_1 = 2.6$. The agreement with the experimental data is thereby in an overall acceptable range justifying the choice of the interfacial force coefficients. Both models are underestimating α_{G} around the centerline with increasing distance from the expansion. In Fig. 6.9b both results for the axial liquid velocity in the single- and the two-phase flow are shown. First of all it is clearly visible that by normalizing the experimental $\overline{U}_z^{\mathrm{L}}$ with its respective U_c value, the influence of the dispersed gas phase on the continuous liquid phase is not considerably pronounced. The most distinguished difference in the experimental data occurs around $z/\mathrm{D}_1 = 5$, whereby the two-phase flow is still not reattached. As already discussed for the single-phase flow, the velocities around the centerline downstream of $z/\mathrm{D}_1 = 3.6$ are also overestimated by the two-phase flow RANS computations.

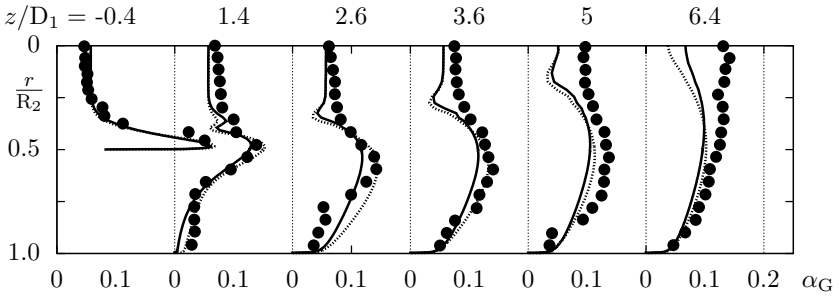

(a) Gas volume fraction α_G

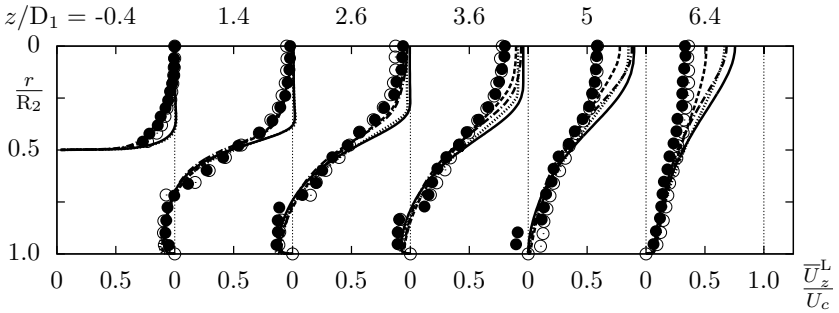

(b) Normalized averaged axial velocity

Figure 6.9: Computation of the gas volume fraction and the normalized axial liquid velocity for the single- and two-phase flow through the sudden expansion by Bel Fdhila [9] at $Re_{D_1} = 78500$ (single-phase flow exp. ∘ and two-phase flow exp. •) by using the RSM: Single-phase (–·–·–·–), RSM: Two-phase (———), EVM: Single-phase (--------) and EVM: Two-phase (·····)

Concerning the turbulent intensities $u_i' = \sqrt{\overline{u_i'}^2}$ shown in Fig. 6.10 several characteristic features can be discussed. As it is the case for the normalized axial velocities, the experimental data for the normalized turbulent intensities differs only slightly between the single- and the two-phase flow. Both baseline models show an early drop of the intensities along the centerline for the bubbly flow results in comparison to the ones in the single-phase flow.

This behavior is supposed to be stemming from the underestimated intensities at the inlet shown in Fig. 6.8b. For the axial intensities, the strongly increasing values around the centerline at $z/\mathrm{D}_1 = 3.6$ and 5 are again not captured, which has been already discussed for the single-phase flow under the consideration of the additional experimental data by Dellenback et al. [23]. For the resulting two-phase flow values, the RSM always lead to higher values of u'_z, while the EVM gives higher values for u'_r. Both trends are also observed for the corresponding single-phase flow computations.

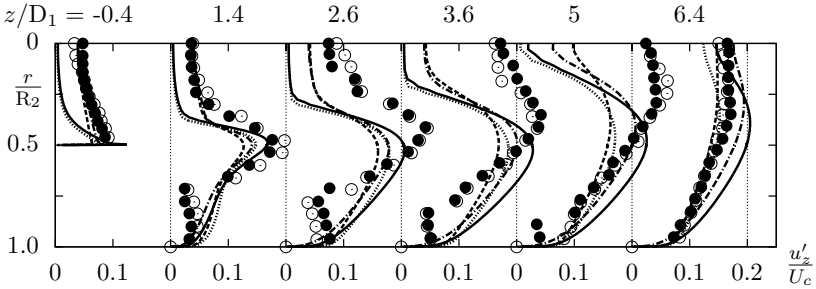

(a) Normalized axial turbulent intensities

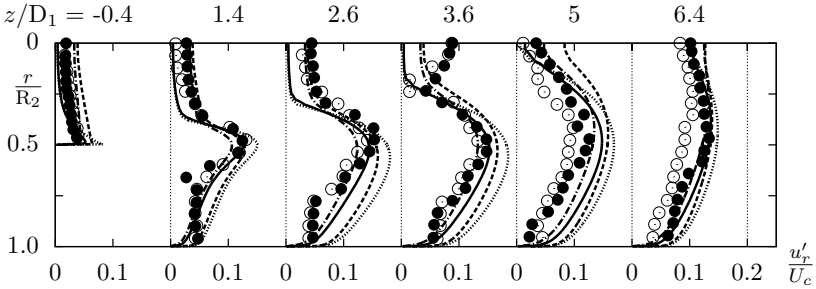

(b) Normalized radial turbulent intensities

Figure 6.10: Computation of the normalized turbulent intensities for the single- and two-phase flow through the sudden expansion by Bel Fdhila [9] at $Re_{\mathrm{D}_1} = 78500$ (single-phase flow exp. ∘ and two-phase flow exp. •) by using the RSM: Single-phase (−·−·−), RSM: Two-phase (———), EVM: Single-phase (-------) and EVM: Two-phase (·····)

In summary, it can be stated that the obtained numerical results and the experimental data are within the same order of magnitude. The occurring deviations are especially concerning the distinguished discrepancies for u_z' and the overestimated values for $\overline{U}_z^{\mathrm{L}}$ around the centerline, while the best agreement between the experimental and the numerical results can be achieved for u_r'. This shows that a complex low Reynolds number second moment closure model like the RSM by Jakirlić and Maduta can be used for the computation of two-phase flows with large separation zones and thereby yielding an overall good prediction. The complex modeling formulation within the RSM, especially the low Reynolds number modifications in the areas close to the solid wall, are not affected in a negative manner. Furthermore, the presence of the dispersed gas phase is not causing numerical instabilities or entirely different results due to disturbed fields. These statements are of course also valid for the EVM in case inlet profiles obtained with the RSM are taken as boundary conditions. The present results illustrate the major importance of a coherent investigation of a two-phase flow and its corresponding single-phase counterpart. Otherwise, the pronounced differences between the computational and experimental data for u_z' and $\overline{U}_z^{\mathrm{L}}$ would surely not be addressed as questionable reference data but most likely as failed modeling predictions because of the presence of the dispersed gas phase. In reality, these discrepancies are already present in the single-phase flow.
An important difference to the two-phase pipe flow computations is the fact that similar distributions for α_{G} are achieved by both models when using the exact same values for C_{l} and C_{td}. A reasonable explanation therefore is that the distribution of local phase fractions can be directly determined by the continuity Eq. (4.5) for the present test case. In these equations the interfacial forces are not directly present. Instead, only the velocity fields and thereby the convective transport directly determine the α_{G} respectively α_{L} distribution. Hence, while the influence of the interfacial forces on the radial α_{G} distribution can be summarized in Eq. (5.4) for classical fully developed steady RANS pipe flow computations, this is by far not as easy to determine for the sudden expansion. An equation like Eq. (5.4) cannot be set up straightforward with a clear identification of the role of the single interfacial forces. This is mainly due to the non-fully developed flow conditions downstream of the expansion, whereby the convective transport terms are present in the equations and play an important role. To analyze how the lift and turbulent dispersion force effect the distribution of α_{G}, both are simply varied over a specific range.

For the variety of $C_{\mathrm{l}} = 0$, 0.1 and 0.2 the coefficient C_{td} is set to one. The results shown in Fig. 6.11 are clearly demonstrating the weak influence of the lift force on the resulting α_{G} distributions. For the previously presented pipe flows, such a variation would lead to entirely different results. It is interesting to see that the accordance between the experiment and the numerical results is getting slightly worse by increasing C_{l}. Increased C_{l} values are also leading to a worse convergence behavior for both models, whereby $C_{\mathrm{l}} = 0.2$ is actually the maximum value by which stable solutions can be achieved.

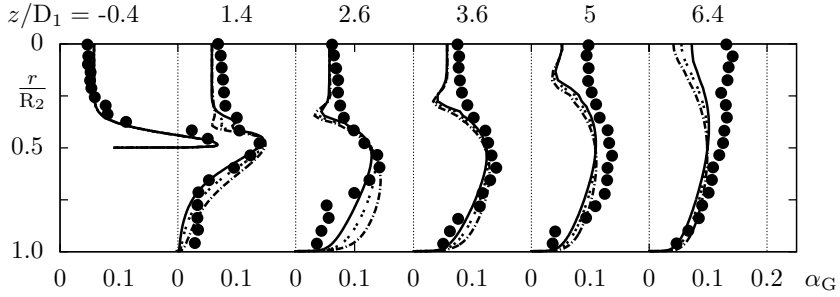

(a) Influence of C_{l} on α_{G} for the RSM

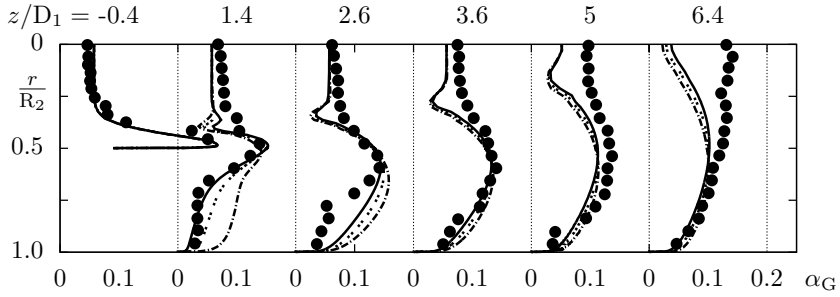

(b) Influence of C_{l} on α_{G} for the EVM

Figure 6.11: Influence of C_{l} on the gas volume fraction through the two-phase flow over the sudden expansion by Bel Fdhila [9] at $Re_{\mathrm{D_1}} = 78500$ (exp. •) for the baseline RANS models with $C_{\mathrm{l}} = 0$ (———), $C_{\mathrm{l}} = 0.1$ (·····) and $C_{\mathrm{l}} = 0.2$ (–·–·–)

As an outcome of this, it is decided to neglect the lift force for analyzing the influence varying C_{td} between $C_{\mathrm{td}} = 0.5$, 1.0 and 2.0 values. The resulting α_{G} distributions are shown in Fig. 6.12. For both additionally evaluated values of C_{td} the influence on α_{G} is most distinct at $z/\mathrm{D}_1 = 1.4$, whereby both values are not leading to an overall better prediction than the originally used value of 1.0. As it is the case for C_{l} the originally proposed value for $C_{\mathrm{td}} = 1$ exhibits the best convergence behavior.

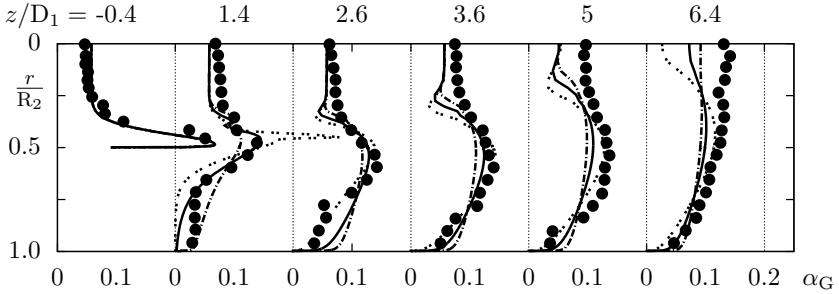

(a) Influence of C_{td} on α_{G} for the RSM

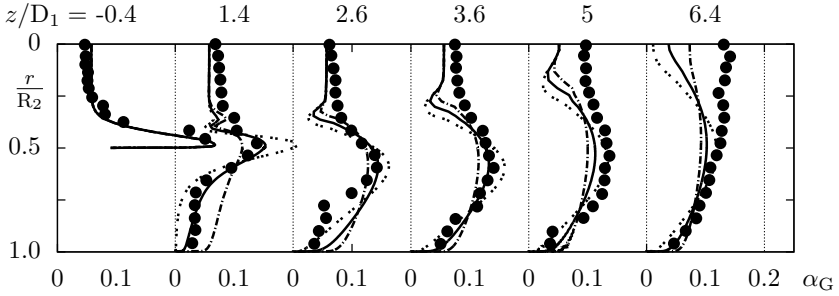

(b) Influence of C_{td} on α_{G} for the EVM

Figure 6.12: Influence of C_{td} on the gas volume fraction for the two-phase flow through the sudden expansion by Bel Fdhila [9] at $Re_{\mathrm{D}_1} = 78500$ (exp. •) for the baseline RANS models with $C_{\mathrm{td}} = 0.5$ (·····), $C_{\mathrm{td}} = 1.0$ (———) and $C_{\mathrm{td}} = 2.0$ (–·–·–)

Both variations have an insignificant influence on $\overline{U}_z^{\mathrm{L}}$ as well as on the turbulent stresses and are therefore not shown here. Hence, the major part of the convective transport in the continuity equation for α_{L} is not altered since $\overline{U}_z^{\mathrm{L}}$ stays the same, which explains the only slightly altered $\alpha_{\mathrm{G}} = 1 - \alpha_{\mathrm{L}}$ distributions.

Performance of the additionally utilized BIT models

In a next step, it is analyzed how the previously obtained results can be enhanced by the usage of BIT models, keeping the known nomenclature from Chapter 5. For the investigations with the model by Rzehak and Krepper [89] only the standard transformation rule Eq. (3.34) is utilized, since Eq. (4.29) already showed its deficiency in Chapter 5. Also, no stable solution could be achieved by using Eq. (4.29). To compare the results obtained with the considered BIT models against the baseline results, the previously utilized baseline inlet values are utilized and no re-calibration of C_{td} and C_{l} has been done. The latter decision is justified by the previously presented investigations, showing that the variation of both interfacial force coefficients has no improving effects on the flow conditions and is in particular worsening the convergence behavior.

Fig. 6.13 shows the newly obtained α_{G} field in comparison to the baseline results. It is evident that the usage of a BIT model in the present test case does not lead to improved results. For both baseline models, the BIT model by Troshko and Hassan [105] has the smallest effect on α_{G}, while the proposed model by Rzehak and Krepper [89] has an essential influence. These results could not be improved by any additionally investigated variation of the interfacial force coefficients. The deviations between the resulting α_{G} distribution are of course representing an uncertainty for the evaluations of the assessment concerning the modulation of turbulent intensities through Eq. (4.26).

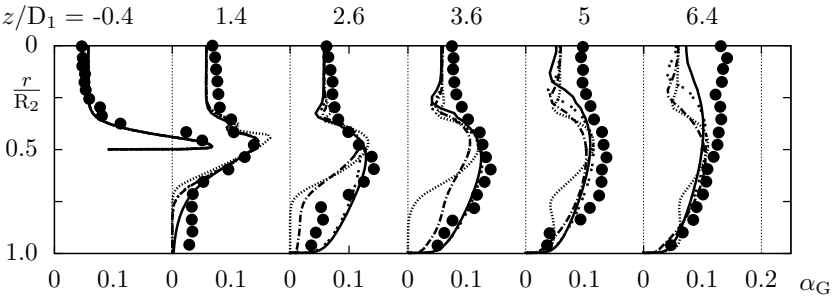

(a) Influence of the BIT models on α_G for the RSM computations

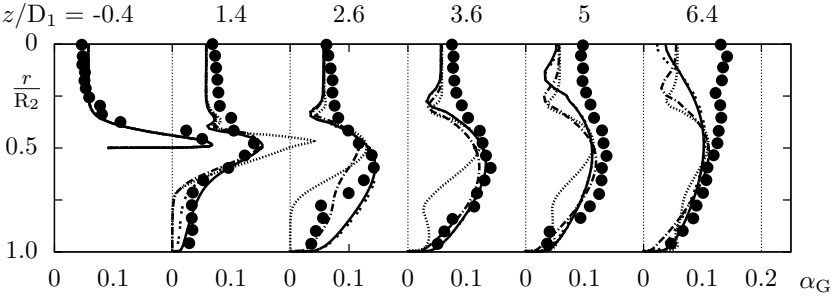

(b) Influence of the BIT models on α_G for the EVM computations

Figure 6.13: Influence of the additionally utilized BIT models on the gas volume fraction for the two-phase flow through the sudden expansion by Bel Fdhila [9] at $Re_{D_1} = 78500$ (exp. •) for both baseline RANS models (———), with +T (·· ··), with +R: $C_{\varepsilon B} = 1.0$ (–·–·) and with +R: $C_{\varepsilon B} = 2.0$ (·····)

While for the pipe flow computations the present BIT models can in general improve k respectively the turbulent intensities, such a statement cannot be made for the sudden expansion test case as seen in Figs. 6.14 and 6.15. In the areas around the centerline, the BIT models are causing a partially drastic decrease of both intensities with an increasing distance from the expansion. Again, the model by Troshko and Hassan [105] has thereby less impact than the model by Rzehak and Krepper [89] irrespective of the utilized baseline model. A similar behavior could already be seen in the pipe flow computations shown in Figs. 5.17, 5.18 and 5.19. In the

recirculation zone close to the solid wall, the resulting intensities obtained with the model by Rzehak and Krepper [89] (especially for $C_{\varepsilon \mathrm{B}} = 1.0$) are partially improved in comparison to the baseline results, by showing less increase for both intensities in the vicinity of the wall. However, the ones obtained with the baseline models are in an overall better agreement with the experimental data. It seems that the influence of the BIT models is less pronounced for the EVM than for the RSM. This might be an indication for the fact, that Eq. (4.28) is not an appropriate link between S_k and $S_{R,ij}$.

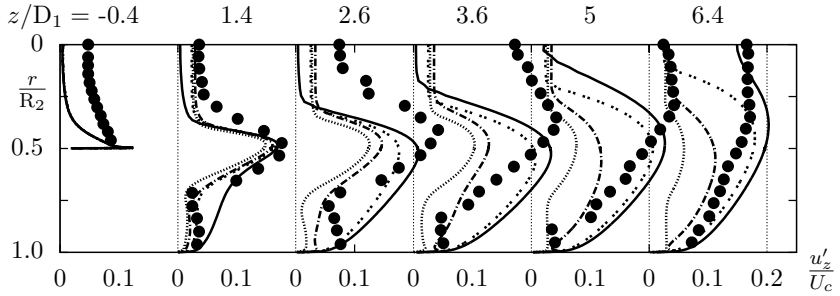

(a) Influence of the BIT models on u_z' for the RSM computations

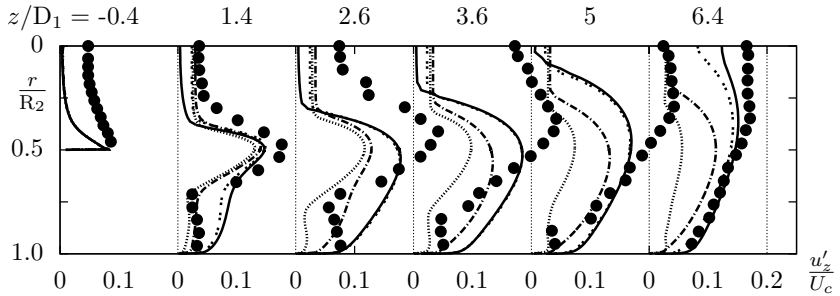

(b) Influence of the BIT models on u_z' for the EVM computations

Figure 6.14: Influence of the additionally utilized BIT models on the normalized axial intensities for the two-phase flow through the sudden expansion by Bel Fdhila [9] at $Re_{\mathrm{D}_1} = 78500$ (exp. •) for both baseline RANS models (———), with +T (·····), with +R: $C_{\varepsilon \mathrm{B}} = 1.0$ (-·-·-·) and with +R:$C_{\varepsilon \mathrm{B}} = 2.0$(·····)

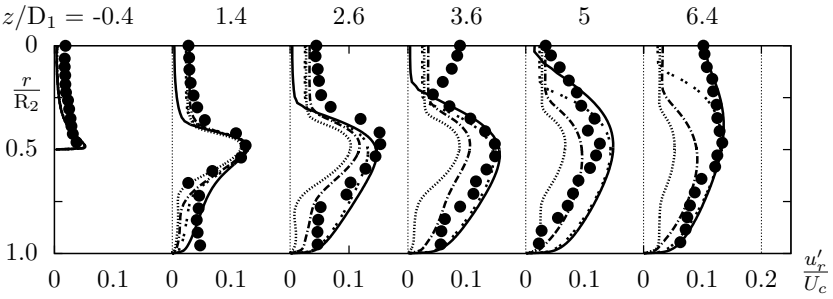

(a) Influence of the BIT models on u_r' for the RSM computations

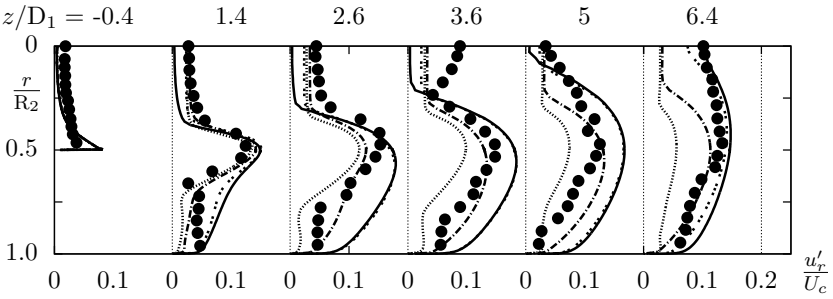

(b) Influence of the BIT models on u_r' for the EVM computations

Figure 6.15: Influence of the additionally utilized BIT models on the normalized radial intensities for the two-phase flow through the sudden expansion by Bel Fdhila [9] at $Re_{\mathrm{D}_1} = 78500$ (exp. •) for both baseline RANS models (———), with +T (·· ·· ··), with +R: $C_{\varepsilon\mathrm{B}} = 1.0$ (–·–·–·) and with +R:$C_{\varepsilon\mathrm{B}} = 2.0$(·····)

By analyzing the resulting axial liquid velocities in Fig. 6.16, it is evident that similar effects to the one observed in the pipe flow computations shown in Fig. 5.20 are also present here. An undesired modulation of the velocity fields is visible for both RANS models, whereby the model by Rzehak and Krepper [89] has a stronger impact, while the usage of the model by Troshko and Hassan [105] is resulting in rather similar results to the ones obtained with the respective baseline models. This is contrary to the results for the pipe flows shown in Fig. 5.20. The strongest negative impact is thereby located around the centerline, with the axial liquid velocity

showing no significant decrease further downstream of the expansion. In addition, the length of the separation zone is strongly overestimated. The virtually complete absence of a liquid velocity gradient in the area around the centerline can at least partly explain the strongly reduced turbulent intensities in these areas, since the production terms P_k respectively P_{ij} are thereby of course strongly underestimated. It cannot be clarified if the BIT model directly causes the negative development of the liquid velocity and thereby the modulated turbulent values or vice versa.

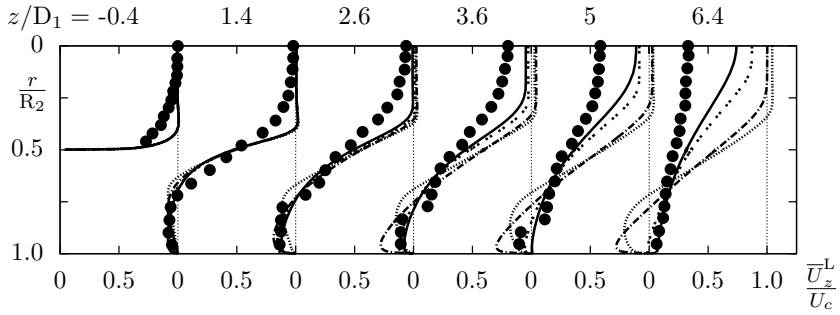

(a) Influence of the BIT models on $\overline{U}_z^{\mathrm{L}}$ for the RSM computations

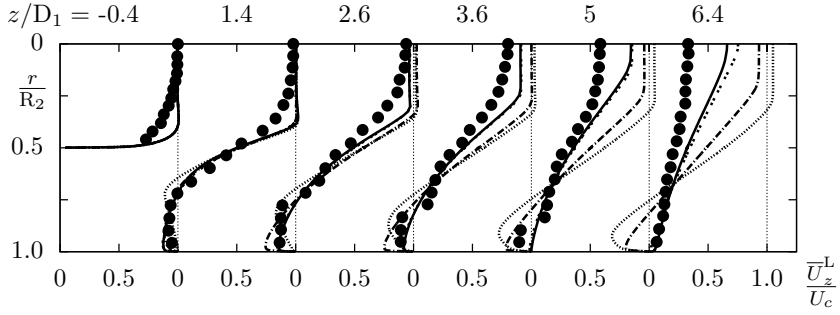

(b) Influence of the BIT models on $\overline{U}_z^{\mathrm{L}}$ for the EVM computations

Figure 6.16: Influence of the additionally utilized BIT models on the normalized axial liquid velocity for the two-phase flow through the sudden expansion by Bel Fdhila [9] at $Re_{\mathrm{D}_1} = 78500$ (exp. •) for both baseline RANS models (———), with +T (·····), with +R: $C_{\varepsilon\mathrm{B}} = 1.0$ (-·-·-·) and with +R:$C_{\varepsilon\mathrm{B}} = 2.0$(·····)

Since all these characteristics are both present for the RSM and for the EVM, it is clear that this behavior does not have its origin in the choice between Eq. (4.29) and Eq. (3.34) for the transformation between S_ε and S_ω.

Finally, nearly the same conclusion for the assessment of a BIT model as for the pipe flow computations can be made in the present flow configuration. While such additional terms for the baseline models can enhance the results at a few positions, most of the modulations are causing entirely false results, especially when looking at the axial liquid velocity in Fig. 6.16. The latter behavior is by far more obvious for the present test case compared to the ones presented in Chapter 5. A major uncertainty still is the fact that the relative velocity cannot be compared against a experimental reference. It is not possible to eliminate the eventuality that $\overline{U}_i^r$ is predicted entirely wrong and thereby influencing the BIT models in an inadequate manner yielding the present unsatisfactory results.

Performance of the scale-resolving method

Two separate major problems occurred while trying to simulate the present flow configuration with a scale-resolving method. The first of these problems deals with the performance of the IIS-RSM in the pipe before the expansion. Several pipe flow simulations were separately carried out therefore. All simulations, no matter which values for C_l have been used or which numerical grid has been applied, led to a complete accumulation of $\langle\alpha_\mathrm{G}\rangle$ in the first cell next to the wall. No possible solution to avoid this behavior could be developed. The second problem is represented by the fact, that no stable two-phase flow simulations could be established for the whole sudden expansion test case with the IIS-RSM. It is unclear if both problematic aspects are linked to each other. In both cases it is assumed that the higher average value of α_G in comparison to the pipe flow simulation as well as for the bubble column test case in the next chapter is responsible for this. These conditions could increase the necessary use of a VOF like method, since in more areas the values for α_G are exceeding a level that can be captured with the TFM framework. Similar discussions have been made concerning the results shown in Fig. 5.23. The two-phase flow simulation of the sudden expansion with the IIS-RSM represent the only aspect of the present work which has to still be finalized in future research.

7 Flow configuration III: Flow in a square cross-sectioned bubble column

The third flow configuration concerns the numerical simulation of a dispersed bubbly flow in a square cross-sectioned bubble column. Such configurations facilitate the opportunity to develop models for the different aspects within the TFM and their respective validation. A review regarding the broad range of experimental investigated bubble columns can be found in Joshi et al. [52]. Most of the time rectangular cross sections with high aspect ratios are utilized, resulting in nearly two-dimensional flow conditions. In contrast, a square cross-sectioned configuration is investigated here, assuring complex three-dimensional flow conditions, which are by far of more practical interest than the purely academical two-dimensional cases. The specific reference experiment chosen for the validation of the present simulations is the one by Deen et al. [20], [21] and [22]. These experimental investigations have been accompanied by the numerical investigations by Zhang et al. [114] and [113]. A major difference to Chapter 5 and 6 is that for the bubble column no corresponding incompressible single-phase flow exists. Therefore, the previously established procedure by analyzing the behavior of the turbulence models in single-phase flows first and then assess their performance in the corresponding bubbly flow cannot be applied here. Instead, the two-phase flow has to be directly analyzed.

The computational domain of the investigated bubble column is shown in Fig. 7.1 and described in Cartesian coordinates, with the z-direction representing the vertical direction. The square base area in in the $x-y$ plain has a side length of W= 0.15 m with the square inlet of the gas phase being located at the center of the base area at $z = 0$ with a side length of 0.03 m. Prior to the air injection, the column is filled with water up to a position of z =H= 0.45 m, numerically realized by initializing $\alpha_{\mathrm{L}} = 1$ up to H. The outlet is located at $z = 0.6$ m and defined by atmospheric boundary conditions. Hence, the volume between the water surface and the outlet of the domain is initially filled with air. This allows the free water surface to move without interfering with the outlet. Thus simple at-

mospheric pressure boundary conditions can be set here. Otherwise if the free surface could interfere with the outlet, complex boundary conditions would be needed to assure numerical stability.

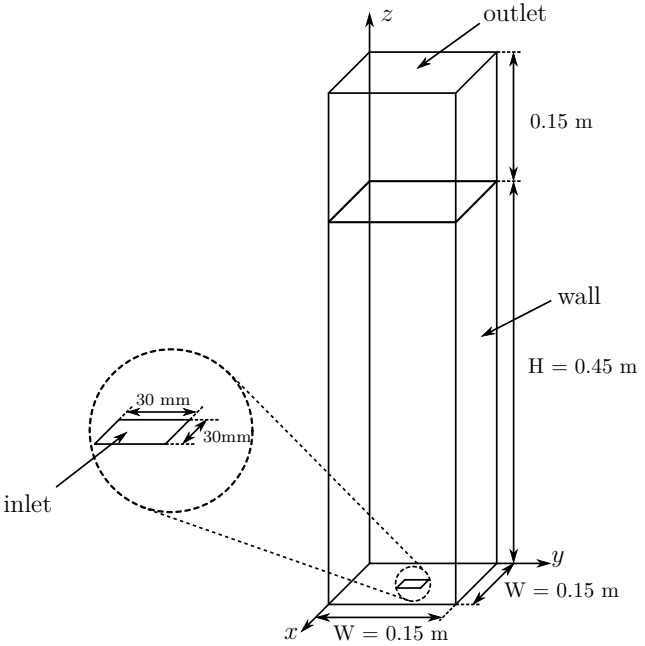

Figure 7.1: Computational domain of the square cross-sectioned bubble column according to Deen et al. [20], [21]

To define the material properties, atmospheric pressure conditions and a room temperature of 20 °C are assumed as it was for instance done by Zhang et al. [114]. During the experiment, a nearly homogeneous bubble size distribution has been measured with a constant diameter of $d_{\mathrm{G}} = 0.004$ m. This justifies the present mono-dispersed approach within the TFM. A superficial gas velocity of $J_{\mathrm{G}} = 0.0049$ m/s (defined over the entire cross section) has been used during the experimental investigations. Based on the inlet cross section, a fixed inlet velocity of $\overline{U}_z^{\mathrm{G}} = 0.1225$ m/s is set.

The statistically averaged flow quantities were measured at different vertical positions. For the averaged vertical velocities of both phases, measured data is available at three different positions z/H=0.57, 0.63 and 0.72 along the centerline of the column at x/W=0.5. For the turbulent intensities in vertical z- and lateral x-direction, measured data only exists at $z/\mathrm{H} = 0.63$ and 0.72. A downside of the chosen reference experiments is that measured data for α_G has not been published. Therefore no comparable statistical reference values for the most interesting physical quantity exists. This represents a major deficiency for the present validation.

The bubble column exhibits a few distinguished differences to the previously presented flow configurations in terms of the utilized boundary conditions. One of these is the necessity to estimate the turbulent values at the inlet. It is required to use several assumptions for defining the turbulent quantities, since only the inlet velocities and α_G are clearly defined by the experimental conditions. Therefore a procedure given by Wilcox [110] is slightly altered to estimate the turbulent kinetic energy

$$k = \frac{3}{2}\left(\overline{U}_z^\mathrm{G} I\right)^2 \tag{7.1}$$

and the dissipation rate

$$\varepsilon = C_\mu^{3/4} \frac{k^{3/2}}{0.07\, d_h} \tag{7.2}$$

at the inlet. These equations include an estimated turbulent intensity I, which is here set to 5%, and a hydraulic diameter d_h set to the side length of the square inlet $d_h = 0.3$ m. It is further assumed that the turbulence at the inlet is isotropic yielding $\overline{u_i' u_j'} = 2/3 k \delta_{ij}$. For both versions of the Reynolds-stress model by Jakirlić and Maduta, $\omega^h = \varepsilon^h / k$ is also estimated by Eqs. (7.1) and (7.2). It is obvious that these estimations are questionable, since turbulent values for the continuous liquid phase are set at the inlet, where actually no water inflow exists which results in a zero liquid velocity. Applying considerably smaller turbulent values or even setting them to zero leads in most cases to diverging simulations. Higher values of the turbulent intensity at the inlet showed no further influences on the results. Therefore the estimated inflow conditions are regarded as justified for carrying out the present simulations.

A more severe difference to the previously presented investigations in Chapter 5 and 6 is that for the bubble column no attempt is made to resolve

the viscous sub-layer close to the solid walls. The actual processes in these near-wall areas are of minor interests for an overall assessment of the model performance for the present flow configuration. Furthermore, the experimental reference does not provide any data in the close vicinity of the walls which could be used for a detailed validation of the near-wall results. Trying to resolve the viscous sub-layer in the present bubble column comes along with severe numerical difficulties allowing no successful simulations. These difficulties are especially concerning the required cell refinements at the bottom wall, causing problems at the inlet due to the resulting high aspect ratios in mean flow direction, and in the wall adjacent cells including the free surface at $z = \mathrm{H}$.

Avoiding the resolution of the viscous sub-layer is accompanied by some modeling simplifications, resulting in an improvemed numerical robustness for the present turbulence models. One of these modifications is to completely neglect the purely near-wall relevant $P_{\omega,3}$ respectively $P_{\tilde{\varepsilon},3}$ term in the scale-supplying equations. To bridge the low Reynolds number areas, the classical wall-functions by Launder and Spalding [61] are utilized to define the wall boundary conditions. For the eddy-viscosity model by Launder-Sharma, then actually behaving as the classical high Reynolds number $k-\varepsilon$ by Launder and Spalding [61], these adjustments are sufficient to guaranty an adequate numerical robustness. For the Reynolds-stress models by Jakirlić and Maduta, the modeling expression of the pressure redistribution Φ_{ij} is simplified towards the high Reynolds number expression by Gibson and Launder [30]. This simply reverses the low Reynolds number modifications firstly introduced by Jakirlić [46]. Of course, the high Reynolds number baseline RSM still differs considerably from the original model by Gibson and Launder [30], for example through the usage of the improved formulation of ν_t by Basara and Jakirlić [6].

The presence of the free surface and the consequential sharp gradient the phase fraction from water to air at $z = \mathrm{H}$, allows no usage of the turbulent dispersion force and it is further necessary to utilize Eq. (4.19) to employ M_i^{ψ} because of the present phase inversion. This requires a definition of d_{L}, which only influences the area above the gas-liquid surface. For the present gas velocity only an insufficiently small amount of water is carried into the area above the surface and the resulting flow fields are actually independent of d_{L}. Therefore d_{L} is arbitrarily set to 0.001 m. The drag force is employed without considering the swarm effect by Legendre and

Magnaudet [62] defined in Eq. (4.13), since the air volume fraction is seldom exceeding a value of $\alpha_G = 0.1$. Also are effects of the liquid velocity gradient by far not as distinct here as for the low Reynolds number computations in the previous chapters due to the non resolved viscous sub-layer. Both the lift force and virtual mass force coefficients are set to 0.5, which was for example also applied by Deen et al. [22].

While the RANS computations in the previous chapters yield steady state solutions, as it was expected due to the globally stable flow configurations, this is not the case for the present bubble column. In a globally unstable configuration as the present configuration both classical formulated RANS models by Jakirlić and Maduta and Launder and Sharma are operating in a URANS mode resolving certain amounts of the unsteady three-dimensional flow structures. Hence, the total amount of turbulent quantities consists of a resolved and a modeled part. It has to be analyzed which amount stems from the modeled quantities and which from the already resolved ones. The time depending computations with all investigated models are done by utilizing the second order BDF (Eq. (2.15)) for the temporal discretization. An adaptive time stepping method ensures that the maximum Co number is always below 0.4. The simulations are carried out for 1000 s with the first 150 s serving as an initial period before the temporal averaging of the interested quantities is started. To allow an appropriate resolution of the present flow structures, the convective term in the momentum equation of the liquid phase is discretized by using the hybrid scheme presented in Eq. (2.12) with the blending factor set to $\gamma = 0.95$ (hence 95% CDS and 5% UDS). This also applies for both baseline RANS models. For the simulations with the IIS-RSM, which is used as the scale-resolving modeling formulation, a higher amount of CDS could not be realized, without introducing certain undesired numerical instabilities.

The bubble column is discretized by three different homogeneous numerical meshes each of them with a particular uniform cell side length Δx_i. These three meshes are a coarse mesh with $\Delta x_i = 10$ mm resulting in 13500 cells, a medium mesh with $\Delta x_i = 6$ mm resulting in 62500 cells and a fine mesh with $\Delta x_i = 5$ mm resulting in 108000 cells. These cell numbers are not arbitrarily chosen since Deen et al. [22] and Zhang et al. [114] used the coarse resolution for an LES of the present column and Ma et al. [69] used the fine resolution for an investigation with the original proposed SAS method by Menter and Egorov [76]. The medium mesh is used by default, since it

provides a good compromise between mesh resolution and computational effort.

Since all simulations are carried out in an unsteady manner, the results of the baseline models as well as the ones obtained with the scale-resolving method are presented at once. The results obtained with the models by Jakirlić and Maduta and Launder and Sharma are again denoted by RSM and EVM, keeping in mind that these models differ from the ones used in Chapter 5 and 6 through the presently employed high Reynolds number modifications. For the bubble column configuration no spatial homogeneity of the averaged results exists, so the shown results are simply time averaged. The presented results are actually not normalized as it was done in the previous chapters, since those are seldom normalized in comparable investigations of the present flow case available in the scientific literature.

Performance of the baseline models and the scale-resolving method

The instantaneous behavior of the present flow simulations are clearly recognized by the iso-surface snapshots of $\alpha_{\mathrm{G}} = 0.02$ shown in Fig. 7.2 colored by the magnitude of the instantaneous gas velocity field. Compared to the fluctuating turbulence captured by the IIS-RSM model, the conventional formulated RSM is capable of returning only the weak mean flow unsteadiness. The averaged vertical velocities obtained with both baseline RANS models and the IIS-RSM are shown in Fig. 7.3 (note the different y-axis scaling between both velocities). An overall good agreement with the experimental data for $\left\langle \overline{U}_z^{\mathrm{L}} \right\rangle$ can be achieved with both Reynolds-stress models. The peak values in the center of the domain as well as the down flow close to the walls of the column are quantitatively predicted. Especially the peak values in the center of the domain are captured. The liquid velocity obtained with the RSM shows an unreasonable increase shortly before the wall, whose origin remains unclear. For the $\left\langle \overline{U}_z^{\mathrm{G}} \right\rangle$ distribution both RSMs slightly overestimate the experimental data. This is most likely linked to an underestimated C_{d} value predicted by the utilized drag force correlation by Tomiyama et al. [103]. In further investigations, several drag force correlations should be employed to analyze if the predicted $\left\langle \overline{U}_z^{\mathrm{G}} \right\rangle$ distributions can be improved. In contrast to the RSM and the IIS-RSM, the velocity distributions obtained with the EVM are in an unsatisfactory agreement

with the reference data, since both phases exhibit a pronounced asymmetric distribution. This behavior has also been identified by Deen et al. [22] for the present case. A reasonable explanation cannot be determined at first sight.

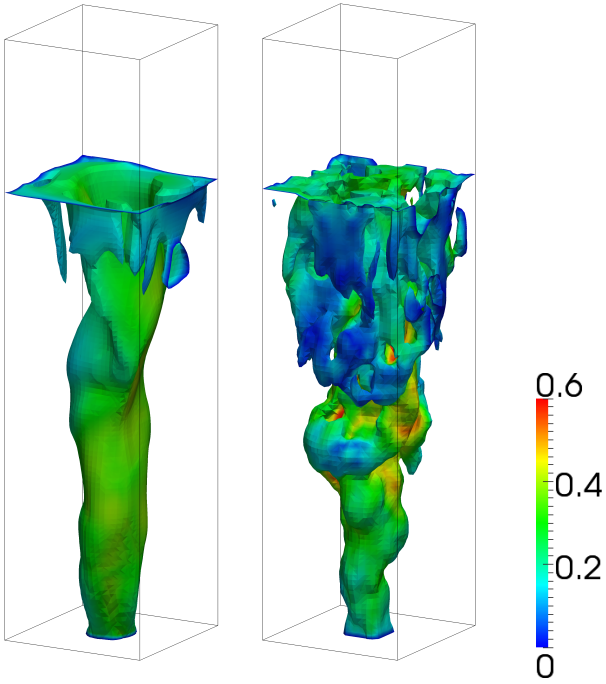

(a) RSM (b) IIS-RSM

Figure 7.2: Snapshots of the iso-surface with $\alpha_G = 0.02$ colored with the magnitude of the instantaneous gas velocity field in m/s obtained with both Reynolds-stress models

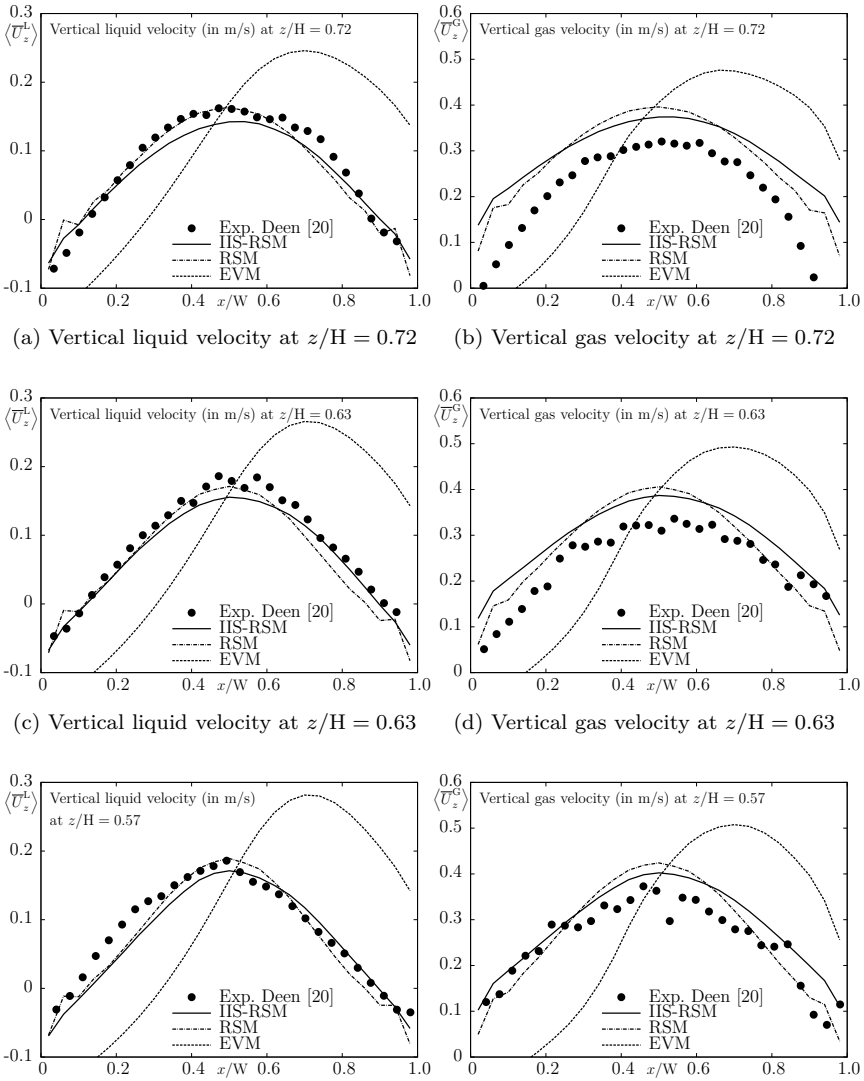

(a) Vertical liquid velocity at $z/\mathrm{H} = 0.72$ (b) Vertical gas velocity at $z/\mathrm{H} = 0.72$

(c) Vertical liquid velocity at $z/\mathrm{H} = 0.63$ (d) Vertical gas velocity at $z/\mathrm{H} = 0.63$

(e) Vertical liquid velocity at $z/\mathrm{H} = 0.57$ (f) Vertical gas velocity at $z/\mathrm{H} = 0.57$

Figure 7.3: Computation of the vertical velocity fields (in m/s) by using the baseline RANS models and the IIS-RSM

The averaged resulting turbulent intensities $\langle u_i \rangle = \sqrt{\langle u_i^2 \rangle}$ obtained with the present models exhibit an overall good agreement with the experimental reference as shown in Fig. 7.4. Surprisingly, this also accounts for the EVM, whereby the modeled part of the turbulent intensities are calculated through Eq. (4.20). These very good results are achieved despite the present asymmetric velocity distribution shown in Fig. 7.3, even if the resulting distribution for $\langle u_z \rangle$ also shows a slightly asymmetric behavior. Nevertheless, the intensities simulated with the EVM and the IIS-RSM are here almost the same. On the other hand, the RSM leads to slightly higher values for the vertical intensities than the other two models. But still, these results are also within the same order of magnitude.

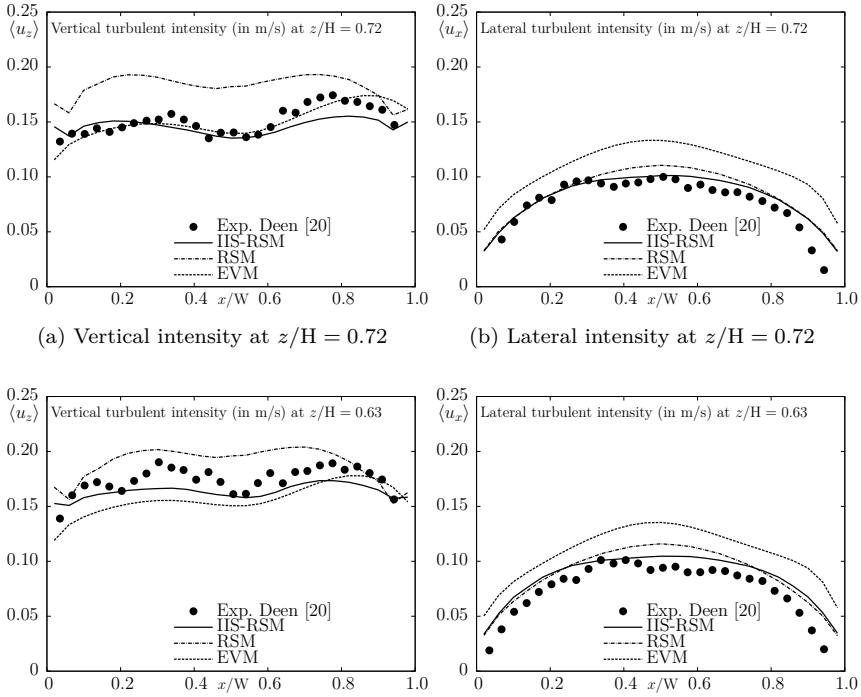

(a) Vertical intensity at z/H = 0.72

(b) Lateral intensity at z/H = 0.72

(c) Vertical intensity at z/H = 0.63

(d) Lateral intensity at z/H = 0.63

Figure 7.4: Computation of the turbulent intensities (in m/s) by using the baseline RANS models and the IIS-RSM

As already stated, the RSM as well as the EVM are acting in a URANS mode here instead of the classical steady state RANS behavior. This occurs without applying any structural changes within the models. In such URANS computations, both models resolve a certain amount of the turbulent fluctuating motions. It is of special interest to analyze which amount of the total turbulent intensities $\langle u_i \rangle$ actually stems from the resolved part $\langle u_i \rangle_{\mathrm{res}} = \sqrt{\langle u_i''^2 \rangle}$. This comparison is exemplary done at $z/\mathrm{H} = 0.63$ in Fig. 7.5, whereby the resolved part of the turbulent intensities is compared against $\langle u_i \rangle$ for the RSM and the EVM. For both models, the amount of resolved turbulence reaches a significant level, whereby the resolved part is considerably lower for the EVM than for the RSM. This can be partially explained for $\langle u_z \rangle$ by the predicted absolute value, which is lower for the EVM than for the RSM. The lower amount of resolved turbulence by the EVM could be an explanation for the asymmetric velocity distributions shown in Fig. 7.3. A significant remaining amount of modeled turbulence could falsely damp out essential turbulent structures which are actually required to obtain a realistic instationary flow field for achieving convincing statistical results. Another possible explanation would be that eddy-viscosity models are quite simply not capable of computing such inherently non isotropic flow configurations. Since only a minor part of the turbulence actually stems from the modeled quantities, the disregard of the turbulent dispersion force, being proportional to k, is further justified.

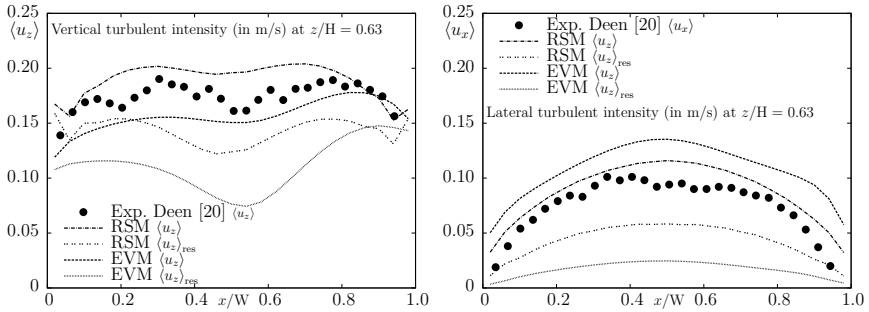

(a) Vertical intensity (b) Lateral intensity

Figure 7.5: Comparison between the resolved part and total amount of the turbulent intensities (in m/s) at $z/\mathrm{H} = 0.63$ obtained with both RANS models

Regardless of the quantitative amount, both the RSM and the EVM are clearly resolving an essential part of the turbulent structures in the bubble column. It is further analyzed how far $\langle u_i \rangle_{\mathrm{res}}$ is increased by using the IIS-RSM on the bassis of Fig. 7.6 at $z/\mathrm{H} = 0.63$. These results demonstrate that almost all significant turbulent structures have been resolved and the modeled contribution to $\langle u_i \rangle$ takes an almost negligible value for both intensities. Since the overall assessment of the IIS-RSM represents the best for all three investigated models, as seen in Figs. 7.3 and 7.4, such a modeling formulation specifically developed for eddy-resolving simulations clearly represents an appropriate approach for such globally unstable flow configurations as the present bubble column.

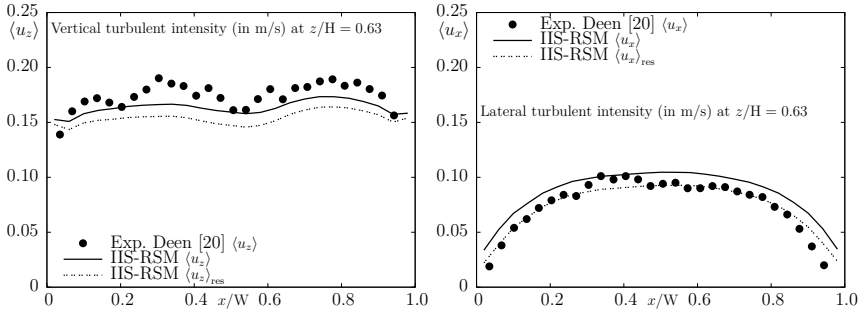

(a) Vertical intensity (b) Lateral intensity

Figure 7.6: Comparison between the resolved part and total amount of the turbulent intensities (in m/s) at $z/\mathrm{H} = 0.63$ obtained with the IIS-RSM

Especially in eddy-resolving simulations, the grid resolution has an essential influence on the resulting flow fields. This influence is exemplary investigated for the IIS-RSM by comparing the results computed with the coarse, the medium and the fine mesh at $z/\mathrm{H} = 0.63$. Fig. 7.7 (note the different y-axis scaling) shows the averaged vertical velocity for both phases. It is obvious that the differences between the medium and fine grid are sufficiently small. Nearly no influence of the mesh resolution on the turbulent intensities is visible as seen in Fig. 7.8. This justifies the usage of the medium grid as an appropriate choice for the present investigations in terms of accuracy and computational effort. Especially concerning the fact that a grid refinement from $\Delta x_i = 6$ mm to $\Delta x_i = 5$ mm already nearly

doubles the number of utilized cells. Even the coarse mesh, while exhibiting a more pronounced deviation, surprisingly still gives results ranging within the same order of magnitude.

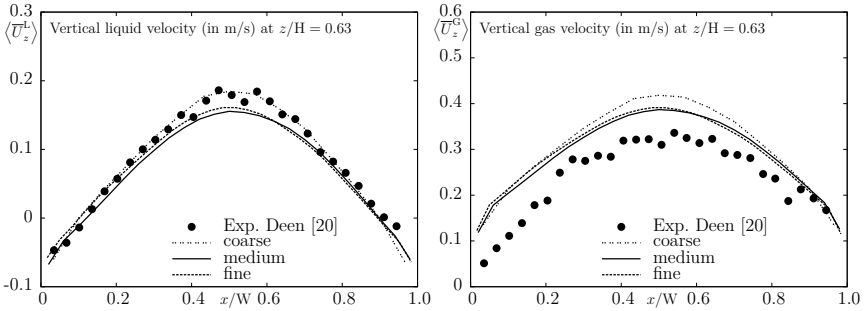

(a) Vertical liquid velocity (b) Vertical air velocity

Figure 7.7: Influence of the grid resolution on the velocity fields (in m/s) at $z/H = 0.63$ obtained with the IIS-RSM

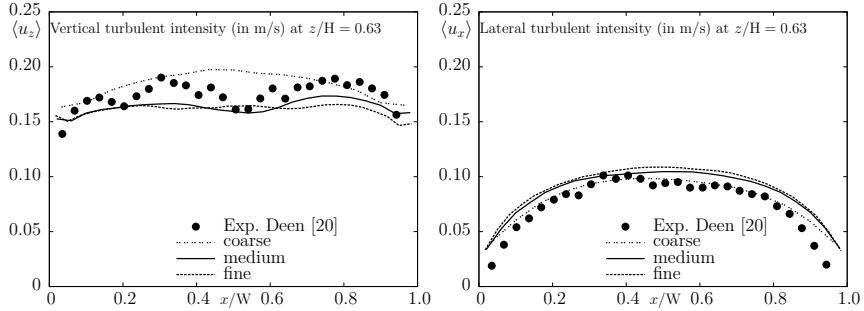

(a) Vertical intensity (b) Lateral intensity

Figure 7.8: Influence of the grid resolution on the turbulent intensities (in m/s) at $z/H = 0.63$ obtained with the IIS-RSM

These results show the overall superior behavior of the IIS-RSM in comparison to both RANS models. Although the results with the RSM are not decisively worse, especially concerning the resulting velocity fields. Both

RSMs perform well with the presently adopted modifications towards the usage in high Reynolds number flows and it is clearly visible that there is no need to resolve the viscous sub-layer in the present configuration to determine good results for the flow quantities of interest. Of course, comparable statistical values for the gas volume fraction could enhance the present validation. Inferior results are achieved with the present EVM, which exhibits a pronounced asymmetric behavior in the resulting velocity fields. This clearly disqualifies the baseline EVM for being utilized for such flow configurations. It is further investigated if the performance of both baseline RANS models can be improved by utilizing additional BIT models.

Performance of the additionally utilized BIT models

The present investigations in conjunction with the BIT models keep the known nomenclature from the previous chapters, hence denoting the usage of the model by Rzehak and Krepper [89] with +R, using again both $C_{\varepsilon B} = 1.0$ and 2.0, and the model by Troshko and Hassan [105] with +T. For the present flow configuration, the usage of BIT models exhibit a few arguable modeling aspects. The first one is concerning the usage in such URANS simulations, whereby the modeled part of the turbulent intensities represents the smaller part of $\langle u_i \rangle$. It has to be analyzed if the BIT models are only affecting the modeled part, the resolved part or both. On the other hand, the baseline models for the present flow configuration are already achieving a convincing overall agreement with the experimental data. For example the intensities shown in Fig. 5.13 or in Fig. 6.14 for the previous investigations showed distinct deviations to the experimental references. Nevertheless, the influence of the BIT models on the present flow configuration is analyzed below.

Fig. 7.9 shows the resulting intensities for the RSM in conjunction with the utilized BIT models. Clearly, the newly computed values are within the same range as the baseline RSM. A general distinct tendency of the BIT models influence cannot be determined. The model by Troshko and Hassan [105] leads to slightly reduced values in the center of the column, while applying the model by Rzehak and Krepper [89] with $C_{\varepsilon B} = 1.0$ mostly results in higher values.

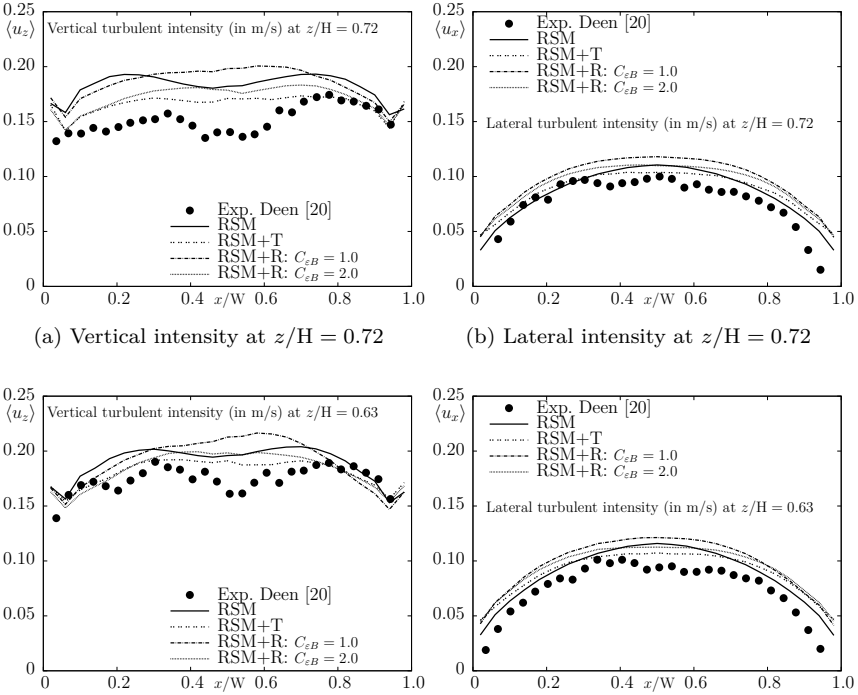

(a) Vertical intensity at z/H = 0.72

(b) Lateral intensity at z/H = 0.72

(c) Vertical intensities at z/H = 0.63

(d) Lateral intensity at z/H = 0.63

Figure 7.9: Computation of the turbulent intensities (in m/s) by using the RSM with additionally utilized BIT models

The usage of BIT models in combination with the EVM, leads to more distinct trends for the turbulent intensities as seen in Fig. 7.10. On the one hand is the slightly visible asymmetry for $\langle u_z \rangle$ disappearing by employing a BIT model, coming along with increased $\langle u_z \rangle$ values for all BIT models. On the other hand are all BIT models decreasing the values for $\langle u_x \rangle$, whereby the match between the resulting intensities and the experimental values is improved.

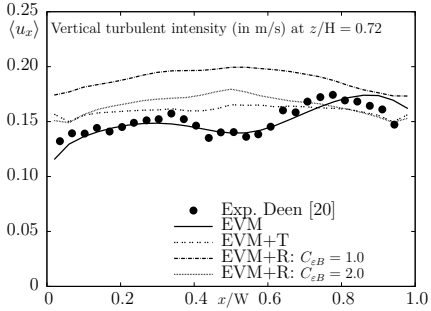

(a) Vertical intensity at $z/\mathrm{H} = 0.72$

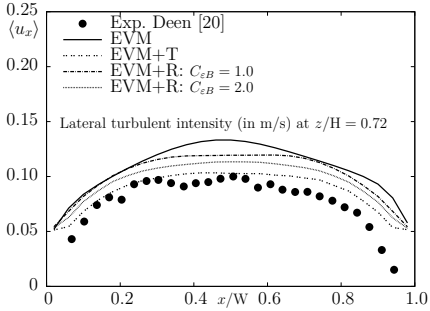

(b) Lateral intensity at $z/\mathrm{H} = 0.72$

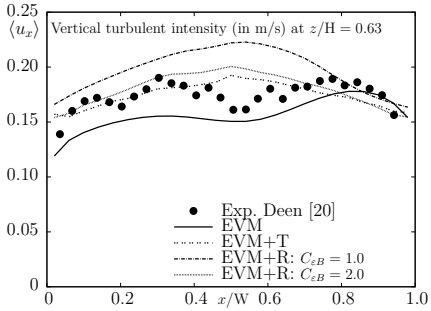

(c) Vertical intensity at $z/\mathrm{H} = 0.63$

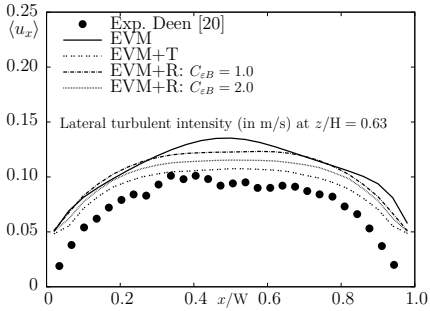

(d) Lateral intensity at $z/\mathrm{H} = 0.63$

Figure 7.10: Computation of the turbulent intensities (in m/s) by using EVM with additionally utilized BIT models

While the effects of the BIT models on the resulting turbulent intensities are more or less distinct, these models have a key influence on the ratio between the modeled and resolved part of $\langle u_i \rangle$. Figs. 7.11 and 7.12 show $\langle u_i \rangle_{\mathrm{res}}$ for the RSM and the EVM obtained in conjunction with the respective BIT models at $z/\mathrm{H} = 0.63$. Clearly the amount of resolved turbulent intensities is increased towards a level nearly covering the whole amount of $\langle u_i \rangle$ by simply comparing these distribution with the total intensities shown in Figs. 7.9 and 7.10. The BIT models are actually decaying the modeled quantities towards an almost negligible level. Because of the decaying modeled quantities, the baseline RANS models lose the remaining amount of their dissipative nature and allow a reasonable development of the present turbulent structures. The computations with both classical

formulated RANS models in conjunction with the BIT models the actually behave simlar to the IIS-RSM.

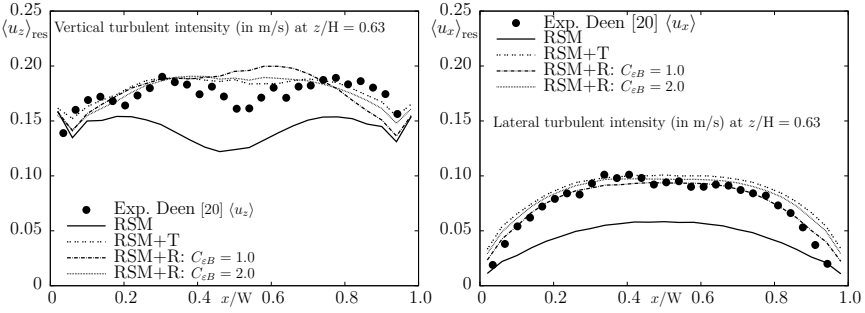

(a) Vertical turbulent intensity (b) Lateral turbulent intensity

Figure 7.11: Comparison between the resolved turbulent intensities $\langle u_i \rangle_{\text{res}}$ (in m/s) at z/H = 0.63 by using the RSM with additionally utilized BIT models and experimental obtained values for $\langle u_i \rangle$

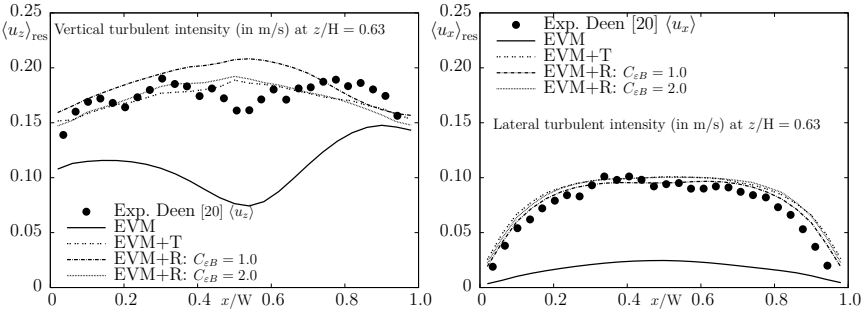

(a) Vertical turbulent intensity (b) Lateral turbulent intensity

Figure 7.12: Comparison between the resolved turbulent intensities $\langle u_i \rangle_{\text{res}}$ (in m/s) at z/H = 0.63 by using the EVM with additionally utilized BIT models and the experimental obtained values for $\langle u_i \rangle$

In the previous chapters, the utilization of BIT models always lead to inferior predicted axial liquid velocity fields as seen in Figs. 5.20 and 6.16. For the present flow configuration, a similar behavior can be seen for the results calculated in conjunction with the RSM shown in Fig. 7.13. Thereby the strongest deviations occur in the center of the column and are most pronounced for the model by Rzehak and Krepper [89] with $C_{\varepsilon B} = 1.0$. An essentially improved velocity distribution is obtained with the EVM in conjunction with the chosen BIT models. As seen in Fig. 7.14, the newly calculated results are exhibiting a qualitatively agreement with the experimental data for both velocities. The asymmetric behavior being present in the baseline results is avoided. For the liquid velocity an very good quantitative agreement is achieved as well. Summarizing these results for the computations of the present bubble column, an ambivalent conclusion regarding the assessment of the additionally utilized BIT models can be made. For example, the substantially improved velocity fields in conjunction with the EVM are in contrast to the same results in combination with the RSM. The behavior of the latter, shown in Fig. 7.13, has already been identified in the previously investigated flow cases. Mentionable is the behavior of the BIT models regarding the nearly complete reduction of the modeled turbulent quantities, even if this yields good results in the case for the EVM.

Since all computations of such a bubble column have to be unsteady and three-dimensional to correctly capture the flow behavior, the use of the IIS-RSM is suggested, keeping in mind that its application does not increase the computational costs in comparison to the baseline models. It is also an obviously more rational approach to resolve the turbulent structures and suppress the modeled turbulent quantities towards a negligible level than achieving this behavior by utilizing the BIT models.

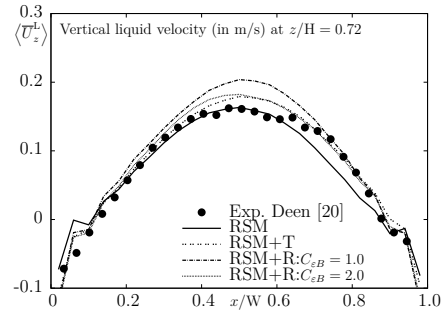

(a) Vertical liquid velocity at $z/\mathrm{H} = 0.72$

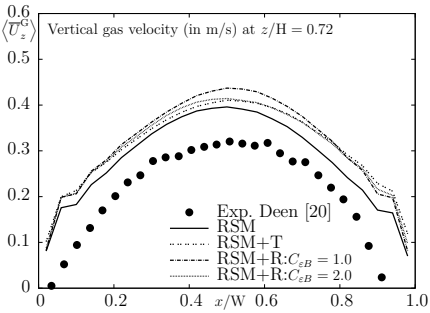

(b) Vertical gas velocity at $z/\mathrm{H} = 0.72$

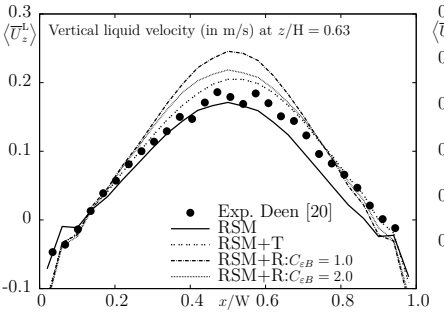

(c) Vertical liquid velocity at $z/\mathrm{H} = 0.63$

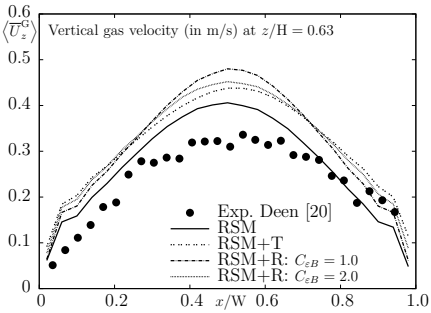

(d) Vertical gas velocity at $z/\mathrm{H} = 0.63$

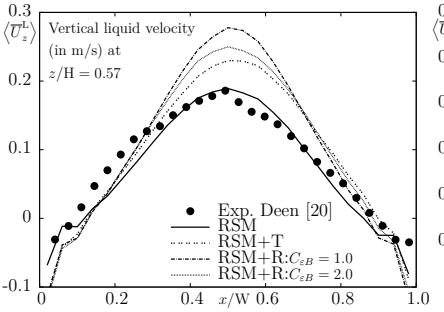

(e) Vertical liquid velocity at $z/\mathrm{H} = 0.57$

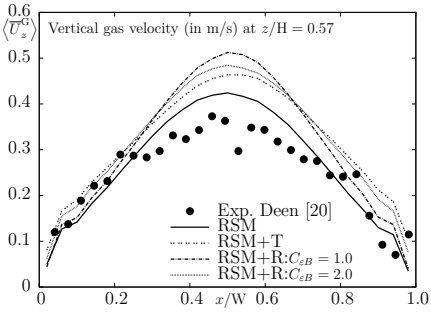

(f) Vertical gas velocity at $z/\mathrm{H} = 0.57$

Figure 7.13: Computation of the vertical velocity fields (in m/s) by using the RSM with additionally utilized BIT models

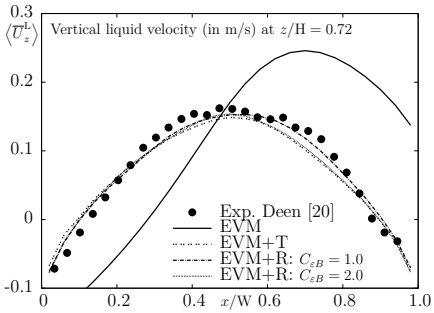

(a) Vertical liquid velocity at $z/\mathrm{H} = 0.72$

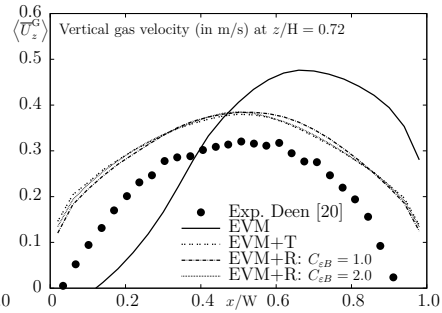

(b) Vertical gas velocity at $z/\mathrm{H} = 0.72$

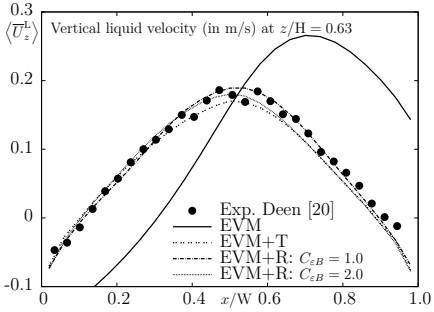

(c) Vertical liquid velocity at $z/\mathrm{H} = 0.63$

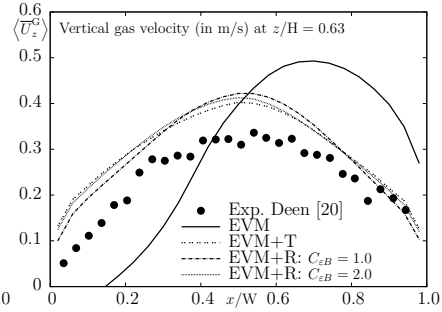

(d) Vertical gas velocity at $z/\mathrm{H} = 0.63$

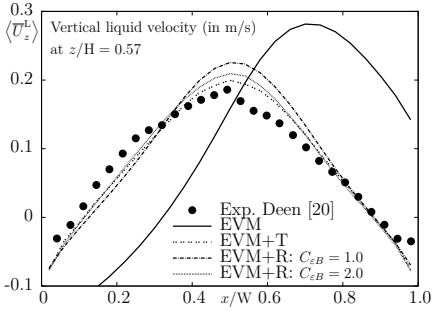

(e) Vertical liquid velocity at $z/\mathrm{H} = 0.57$

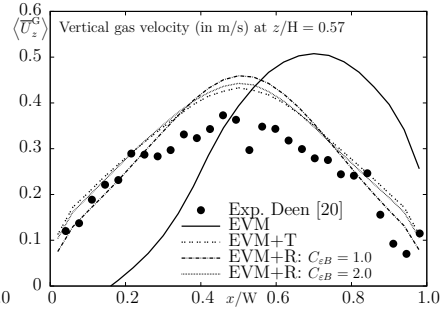

(f) Vertical gas velocity at $z/\mathrm{H} = 0.57$

Figure 7.14: Computation of the vertical velocity fields (in m/s) by using the EVM with additionally utilized BIT models

8 Conclusions and outlook

In the present work several inherently different turbulent bubbly flow configurations have been computationally investigated within the two-fluid model (TFM) framework by utilizing two essentially different versions of an advanced near-wall Reynolds-stress model (RSM). Successful capturing of the turbulent quantities associated with the continuous liquid phase, by employing such a high-order modeling approach, demonstrates its high potential compared to the widely used high Reynolds number eddy-viscosity models. Indeed, the second-moment closure models relying on the solutions of transport equations for individual Reynolds-stress components, which have been rarely employed in computing two-phase flow systems, represent a promising approach for future investigations within the TFM framework.

The present computations are enabled by an appropriate combination between the RSM and some specific model proposals for the interfacial momentum transfer term M_i^{ψ}, adopted from the open literature. A key element in the modeling of the latter process in the present computational campaign. accounting for the near-wall areas, represents the utilization of the model proposed by Legendre and Magnaudet [62] for the drag force (Eq. (4.13)) and the lift damping in the immediate wall vicinity. These model are capable of capturing the increasing liquid velocity gradient in the low Reynolds number areas of the flow. Admittedly, not all aspects could be solved by employing an advanced formulation of the turbulent stress components, like for instance the strong dependency of the resulting flow fields on the specifically selected models for M_i^{ψ}. To clarify this challenge, more comprehensive reference data from experiments or direct numerical simulations should be available. The main conclusive statements arising from the results obtained with conventional RANS, i.e. the conventional Unsteady RANS modeling framework, can be summarized as follows:

- The presently adopted Reynolds-stress model by Jakirlić and Maduta results in a very good qualitative agreement with available reference data in terms of capturing important flow physics details in all investigated configurations. Also, a good quantitative agreement could be achieved for most of the flow and turbulence properties considered

throughout the numerical investigation. Herewith, one of the main tasks of the present study is fulfilled: a suitable coupling between the TFM methodology, especially with respect to the model expressions for M_i^{ψ}, and the afore mentioned near-wall Reynolds-stress model describing the turbulence dynamics of the continuous liquid phase.

- The eddy-viscosity model by Launder and Sharma is in general capable of adequately computing the present two-phase flow configurations, with an qualitative agreement corresponding to industrial standards. But, its comparative assessment with the RSM by Jakirlić and Maduta, reveals some non-physical results. This is especially visible at an asymmetrically predicted velocity field in the bubble column (Chapter 7) and within the pipe flow prior to the sudden expansion (Chapter 6). Some of those anomalies can be attributed to the fact that several key aspects for bubbly flow computations, as for instance the correct determination of the radial pressure distribution in pipe flows (discussed in Chapter 5), can indeed only be captured by Reynolds-stress models, and not by the standard eddy-viscosity models.

- The attempt to improve the baseline RANS results by utilizing in addition the BIT (Bubble-induced Turbulence) models, based on the proposals by Rzehak and Krepper [89] and Troshko and Hassan [105], leave a somewhat conflicting impression. It is evident that for bubbly flow computations within the conventional RANS modeling framework, such models are the only available choice of capturing to some extent the modulation of the single-phase shear-induced turbulence due to the presence of the discrete bubbly phase in a two-phase flow system. On the one hand, the addition of this model term led to an improved prediction of the k (kinetic energy of turbulence) distributions in the pipe flow geometry, but its employment, on the other hand, caused an inferior prediction of the liquid velocity fields in several other computations. To summarize, while the baseline Reynolds-stress model, not specifically developed for bubbly flow computations, predicts reasonable results for all investigated flow cases, the consideration of the BIT model terms, which are specifically developed for bubbly flow computations, bears the risk of the results worsening.

The novel scale-resolving version of the above-mentioned Reynolds-stress model (denoted also as an Instability-Sensitized RSM – IS-RSM) has shown its increased potential for the simulation of turbulent bubbly flows within

the TFM framework. An essential factor therefore is the use of the improved modeling treatment proposed by Maduta et al. [71], providing an enhanced numerical robustness without any further structural changes of the model. This improved formulation (denoted by IIS-RSM) allows in addition a reliable and stable use of the second-order accurate central-differencing schemes for the discretization of convective terms.

Promising results for bubbly flow simulations are obtained by using this IIS-RSM. The employment in the bubble column demonstrates its superiority in comparison with its conventional RSM counterpart and especially in comparison with the utilized eddy-viscosity model. Since all computations for this flow case have to be carried out three-dimensionally and in the unsteady manner, the scale-resolving formulation is indeed the best choice to obtain results at affordable computational costs. Furthermore, the capability of the IIS-RSM in capturing the fluctuating turbulence in the inherently steady flow in a vertical straight pipe contributes decisively to the superior results in comparison to those obtained by the baseline RANS model computations by even neglecting the virtual mass force as well as turbulent dispersion force. Clearly, a key aspect associated with the further usage of the IIS-RSM in bubbly flows is the development of a 'generalized' model for the interfacial forces momentum transfer (M_i^{ψ}) with respect to the capability of capturing the locally increased values of the gas volume fraction α_{G}, as seen in Fig. 5.23. Unfortunately, such a 'generalized' modeling formulation for M_i^{ψ} has not been developed so far. Thus, the currently established modeling approach for M_i^{ψ} represents the major uncertainty in the scale-resolving simulations.

Several suggestions for further investigations with the achieved model expressions can be proposed. The obvious objective should focus on the development of a combined formulation between the conventionally formulated Reynolds-stress model and a corresponding BIT model. The aim is to preserve the improved prediction of turbulent quantities, such as of the turbulent kinetic energy (see Fig. 5.17), by simultaneously avoiding a worsened prediction of other essential flow aspects, relating primarily to the axial velocity (see e.g., Fig. 5.20). This could be achieved by focusing on a re-formulated connection between S_k and $S_{R,ij}$, as for example done by Colombo and Fairweather [16], or by a new calibration of the coefficient $C_{\varepsilon\mathrm{B}}$ in the model by Rzehak and Krepper [89]. Suitable additional reference values would be desired and can be provided by further experimental

investigations of turbulent bubbly pipe flows, e.g. [64], [107] and [95], a turbulent bubbly mixing layer investigated by Roig et al. [86] or the decay of turbulence in homogeneous bubbly flows by Lance and Bataille [59]. This proposed further development can of course not be an adequate substitute for the required fundamental investigations by experiment or by DNS about the "true" formulation of the required bubble time-scale τ_B and therefore keeps the theoretical weaknesses and restrictions of the bubble-induced turbulence concept. While these proposed investigations could be conveniently carried out, long-term enhancements should focus on a generalization of the underlying two-phase flow modeling methodology itself. A primary objective should be the implementation of the present highly-accurate turbulence models into a hybrid numerical method combining advantages of both the volume of fluid (VOF) methodology and the TFM framework. Such methodologies have been developed in the past by for example Cerne [13]. So far, no advanced hybrid RANS/LES modeling formulations, such as the here utilized eddy-resolving Reynolds-stress model, have been applied in conjunction with these approaches. Unfortunately, a well-defined hybrid VOF/TFM methodology is presently not available in the official OpenFOAM® computational code. Hence, the development and implementation of such a hybrid VOF/TFM would be required before using the present high order turbulence models.

Bibliography

[1] A. Alajbegovic, D. A. Drew, and R. T. Lahey. An analysis of phase distribution and turbulence in dispersed particle/liquid flows. *Chemical Engineering Communications*, 174:85–133, 1999.

[2] S. P. Antal, R. T. Lahey, and J. E. Flaherty. Analysis of phase distribution in fully developed laminar bubbly two-phase flow. *International Journal of Multiphase Flow*, 17:635–652, 1991.

[3] T. R. Auton. The lift force on a spherical body in a rotational flow. *Journal of Fluid Mechanics*, 183:199–218, 1987.

[4] M. H. Baba-Ahmadi and G. R. Tabor. Inlet conditions for les using mapping and feedback control. *Computers and Fluids*, 38:1299–1311, 2009.

[5] B. Basara. Employment of the second-moment turbulence closure on arbitrary unstructured grids. *International Journal for Numerical Methods in Fluids*, 44:377–407, 2004.

[6] B. Basara and S. Jakirlić. A new, hybrid turbulence modelling strategy for industrial CFD. *International Journal for Numerical Methods in Fluids*, 42:89–116, 2003.

[7] H. M. Bücker, B. Pollul, and A. Rasch. On CFL evolution strategies for implicit upwind methods in linearized Euler equations. *International Journal for Numerical Methods in Fluids*, 59:1–18, 2009.

[8] A. Behzadi, R. Issa, and H. Rusche. Modelling of dispersed bubble and droplet flow at high phase fractions. *Chemical Engineering Science*, 59:759–770, 2004.

[9] R. Bel Fdhila. *Analyse expérimentale et modélisation d'un écoulement vertical à bulles dans un élargissement brusque*. PhD Thesis, Institut de Mécanique des Fluides de Toulouse, 1991.

[10] R. Bel Fdhila and O. Simonin. Eulerian prediction of a turbulent bubbly flow downstream of a sudden pipe expansion. In *6th Workshop on Two-Phase Flow Predictions*, march/april 1992.

[11] J. Boussinesq. Théorie de l'écoulement tourbillant. *Mem. Présentés par Divers Savants Acad. Sci. Inst. Fr.*, 23:46–50, 1877.

[12] A. Burns, T. Frank, I. Hamill, and J.-M. Shi. The favre averaged drag model for turbulence dispersion in eulerian multi-phase flows. In *5th Int. Conf. on Multiphase Flow*, 2004.

[13] G. Cerne, S. Petelin, and I. Tiselj. Coupling of the interface tracking and the two-fluid models for the simulation of incompressible two-phase flow. *Journal of Computational Physics*, 171:776–804, 2001.

[14] J. Chahed, V. Roig, and L. Masbernat. Eulerian-eulerian two-fluid model for turbulent gas-liquid bubbly flows. *International Journal of Multiphase Flow*, 29:23–49, 2003.

[15] D. Cokljat, M. Slack, and S. A. Vasquez. Reynolds-stress model for eulerian multiphase. *Progress in Computational Fluid Dynamics*, 6, 2006.

[16] M. Colombo and M. Fairweather. Multiphase turbulence in bubbly flows: Rans simulations. *International Journal of Multiphase Flow*, 77:222–243, 2015.

[17] B. Daly and F. H. Harlow. Transport equation in turbulence. *Physics of Fluids*, 13:2634–2649, 1970.

[18] L. Davidson. Evaluation of the SST-SAS model: Channel flow, asymmetric diffuser and axi-symmetric hill. 13, 2006.

[19] E. de Villiers. *The potential of large eddy simulations for the modeling of wall bounded flows.* PhD Thesis, Imperial College of Science, Technology and Medicine, 2006.

[20] N. Deen. *An experimental and computational study of fluid dynamics in gas-liquid chemical reactors.* PhD Thesis, Aalborg University, 2001.

[21] N. G. Deen, B. H. Hjertager, and T. Solberg. Comparison of PIV and LDA measurement methods applied to the gas-liquid flow in a bubble column. In *10th Int. Symp. on Appl. of Laser Techniques to Fluid Mech., Lisbon, Portugal, July 10-13*, 2000.

[22] N. G. Deen, T. Solberg, and B. H. Hjertager. Numerical simulation of the gas-liquid flow in a square cross-sectioned bubble column. In *CHISA 14th Int. Congress of Chemical and Process Engineering, Praha, Czech Republic, August 27-31*, 2000.

[23] P. Dellenback, D. Metzger, and G. Neitzel. Measurements in turbulent swirling flow through an abrupt axisymmetric expansion. *AIAA Journal*, 26:669–681, 1998.

[24] D. Drew and R. Lahey. Phase-distribution mechanisms in turbulent low-quality two-phase flow in a circular pipe. *Journal of Fluid Mechanics*, 117:91–106, 1982.

[25] J. Eggels. *Direct and large eddy simulation of turbulent flow in a cylindrical pipe geometry.* PhD Thesis, Delft University of Technology, 1994.

[26] Y. Egorov, F. R. Menter, R. Lechner, and D. Cokljat. The scale-adaptive simulation method for unsteady turbulent flow predictions. part 2: Application to complex flows. *Flow Turbulence Combust.*, 85:139–165, 2010.

[27] M. Ferziger, Joel H. und Perić. *Numerische Strömungsmechanik.* Springer Verlag Berlin Heidelberg New-York, 2008.

[28] J. Fröhlich. *Large Eddy Simulation turbulenter Strömungen.* B.G. Teubner Verlag, 2006.

[29] J. Fröhlich and D. von Terzi. Hybrid LES/RANS methods for the simulation of turbulent flows. *Progress in Aerospace Sciences*, 44:349–377, 2008.

[30] M. M. Gibson and B. E. Launder. Ground effects on pressure fluctuations in the atmospheric boundary layer. *Journal of Fluid Mechanics*, 86:491–511, 1978.

[31] O. T. W. Group. Sig turbulence / dellenback abrupt expansion, 2014.

[32] K. Hanjalić. *Two-dimensional asymmetric turbulent flow in ducts.* PhD thesis, Imperial College London, UK, 1970.

[33] K. Hanjalić. Advanced turbulence closure models: a view of current status and future prospects. *International Journal of Heat and Fluid Flow*, 15(3), 1994.

[34] K. Hanjalić and S. Jakirlić. Contribution towards the Second-Moment Closure modelling if separating turbulent flows. *Comput. Fluids*, 27 (2):137–156, 1998.

[35] K. Hanjalić and B. E. Launder. Contribution towards a Reynolds-stress closure for low Reynolds number turbulence. *Journal of Fluid Mechanics*, 74:593–610, 1976.

[36] K. Hanjalić and B. E. Launder. *Modelling turbulence in engineering and the environment: Second-moment routes to closure.* Cambridge University Press, first edition, 2011.

[37] T. Hibiki and M. Ishii. Lift force in bubbly flow systems. *Chemical Engineering Science*, 62:6457–6474, 2007.

[38] D. Hill. *The computer simulation of dispersed two-phase flows.* PhD Thesis, Imperial College of Science, Technology and Medicine, Exhibition Road, London SW7 2BX, 1998.

[39] C. W. Hirt and B. D. Nichols. Volume of fluid (VOF) method for the dynamics of free boundaries. *Journal of Computational Physics*, 39:201–225, 1981.

[40] S. Hosokawa and A. Tomiyama. Multi-fluid simulation of turbulent bubbly pipe flows. *Chemical Engineering Science*, 64:5308–5318, 2009.

[41] S. Hosokawa and A. Tomiyama. Effects of bubbles on turbulent flows in vertical channels. In *7th International Conference on Multiphase Flow*, Tampa, May 2010.

[42] S. Hosokawa and A. Tomiyama. Bubble-induced pseudo turbulence in laminar pipe flows. *International Journal of Heat and Fluid Flow*, 40:97–105, 2013.

[43] M. Ilić. *Statistical analysis of liquid phase turbulence based on direct numerical simulations of bubbly flows.* PhD thesis, Forschungszentrum Karlsruhe, 2006.

[44] M. Ishii and Hibiki. *Thermo-Fluid dynamics of two-phase flow.* Springer, 2011.

[45] R. Issa. Solution of implicitly discretized fluid flow equations by operator-splitting. *Journal of Computational Physics*, 62:40–65, 1986.

[46] S. Jakirlić. *Reynolds-Spannungs-Modellierung komplexer turbulenter Strömungen*. PhD thesis, Universität Erlangen-Nürnberg, 1997.

[47] S. Jakirlić and K. Hanjalić. A new approach to modelling near-wall turbulence energy and stress dissipation. *Journal of Fluid Mechanics*, 459:139–166, 2002.

[48] S. Jakirlić and J. Jovanović. On unified boundary conditions for improved predictions of near-wall turbulence. *Journal of Fluid Mechanics*, 656:530–539, 2010.

[49] S. Jakirlić and R. Maduta. Extending the bounds of 'steady' rans closures: Toward an instability-sensitive reynolds stress model. *International Journal of Heat and Fluid Flow*, 51:175–194, 2015.

[50] H. Jasak. *Error Analysis and Estimation for the Finite Volumen Method with Applications to Fluid Flows*. PhD thesis, Imperial College, 1996.

[51] W. Jones and B. E. Launder. Prediction of laminarization with a two-equation model of turbulence. *International Journal of Heat and Mass Transfer*, 15:301–314, 1972.

[52] J. Joshi, V. Vitankar, A. Kulkarni, M. Dhotre, and K. Ekambara. Coherent flow structures in bubble column reactores. *Chemical Engineering Science*, 57:3157–3183, 2002.

[53] I. Kataoka, D. Besnard, and A. Serizawa. Basic equation of turbulence and modeling of interfacial transfer term in gas-liquid two-phase-flow. *Chemical Engineering Communications*, 118:221–236, 1992.

[54] I. Kataoka and A. Serizawa. Basic equations of turbulence in gas-liquid two-phase flow. *International Journal of Multiphase Flow*, 15, No. 5:843–855, 1989.

[55] G. Khoury, P. Schlatter, A. Noorani, P. Fischer, G. Brethouwer, and A. Johansson. Direct numerical simulation of turbulent pipe flow at moderately high reynolds numbers. *Flow Turbulence Combustion*, 91:475–495, 2013.

[56] J. Kim, P. Moin, and R. Moser. Turbulence statistics in fully-developed channel flow at low reynolds number. *Journal of Fluid Mechanics*, 177:133–166, 1987.

[57] R. T. Lahey and D. A. Drew. An analysis of two-phase flow and heat transfer using a multidimensional, multi-field, two-fluid computational fluid dynamics (cfd) model. In *Japan/US Seminar in Two-Phase Flow Dynamics*, 2000.

[58] R. T. Lahey, M. Lopez de Bertodano, and O. C. Jones. Phase distribution in complex geometry conduits. *Nuclear Engineering and Design*, 144:177–201, 1993.

[59] M. Lance, J. L. Marie, and J. Bataille. Homogeneous turbulence in bubbly flows. *Journal of Fluids Engineering*, 113:295–300, 1991.

[60] B. Launder and B. Sharma. Application of the energy-dissipation model of turbulence to the calculation of flow near a spinning disc. *Letters in Heat and Mass Transfer*, 1:131–138, 1974.

[61] B. E. Launder and D. B. Spalding. The numerical computation of turbulent flows. *Comput. Methods Appl. Mech. Eng.*, 3:269–289, 1974.

[62] D. Legendre and J. Magnaudet. The lift force on a spherical bubble in a viscous linear shear flow. *Journal of Fluid Mechanics*, 168:81–126, 1998.

[63] M. Leschziner. *Statistical Turbulence Modelling for Fluid Dynamics - Demystified*. Imperial College Press, 2014.

[64] T. Liu. The role of bubble size on liquid phase turbulent structure in two-phase bubbly flows. In *Proceedings of the Third International Conference on Multiphase Flow*, Lyon, June 1998.

[65] M. Lopez de Bertodano, R. Lahey Jr, and O. Jones. Phase distribution in bubbly two-phase flow in vertical ducts. *International Journal of Multiphase Flow*, 20:805–818, 1994.

[66] M. Lopez de Bertodano, S. Lee, R. Lahey Jr, and D. Drew. The prediction of two-phase turbulence and phase distribution phenomena using a reynolds stress model. *Journal of Fluid Engineering*, 112:107–113, 1990.

[67] M. A. Lopez de Bertodano. *Turbulent bubbly two-phase flow in a triangual duct*. PhD thesis, Rensselaer Polytechnic Institute, 1992.

[68] J. L. Lumley. Computational modeling of turbulent flows. *Advances in Applied Mechanics*, 18:123–176, 1978.

[69] T. Ma, D. Lucas, T. Ziegenhein, J. Fröhlich, and N. Deen. Scale adaptive simulation of a square cross-sectioned bubble column. *Chemical Engineering Science*, 131:101–108, 2015.

[70] R. Maduta. *An eddy-resolving Reynolds stress model for unsteady flow computations: development and application.* PhD thesis, Technische Universität Darmstadt, 2013.

[71] R. Maduta, S. Jakirlić, and M. Ullrich. A numerically upgraded instability sensitized Reynolds stress model for complex turbulent flow applications. In *Turbulence, Heat and Mass Transfer 8*, 2015.

[72] F. Menter. Two equation eddy-viscosity turbulence models for engineering applications. *AIAA Journal*, 32, 1994.

[73] F. Menter and Y. Egorov. Revisiting the turbulent length scale equation. In *IUTAM Symposium: One Hundred Years of Boundary Layer Research*, 2004.

[74] F. Menter and Y. Egorov. A scale-adaptive simulation model using two-equation models. In *43rd AIAA Aerospace Sciences Meeting and Exhibit*, January 2005.

[75] F. Menter and Y. Egorov. Formulation of the scale-adaptive simulation (SAS) model during the desider project. *Notes on Numerical Fluid Mechanics*, 103:51–62, 2009.

[76] F. Menter and Y. Egorov. The Scale-Adaptive Simulation method for unsteady turbulent flow predictions. part 1: Theory and model description. *Flow, Turbulence and Combustion*, 85:113–138, 2010.

[77] P. Oliveira and R. Issa. Numercial aspects of an algorithm for the eulerian simulation of two-phase flows. *International Journal for Numerical Methods in Fluids*, 43:1177–1998, 2003.

[78] OpenCFD. *OpenFOAM User Guide*, 2.2.x edition, August 2013.

[79] M. Perić. *A finite volume method for the prediction of three-dimensional flow in complex ducts.* PhD Thesis, Imperial College, University of London, 1985.

[80] D. Pfleger and S. Becker. Modeling and simulation of the dynamic flow behavior in a bubble column. *Chemical Engineering Science*, 56:1737–1747, 2001.

[81] M. S. Politano, P. M. Carrica, and J. Converti. A model for turbulent polydisperse two-phase flow in vertical channels. *International Journal of Multiphase Flow*, 29:1153–1182, 2003.

[82] S. B. Pope. *Turbulent Flows*. Cambridge University Press, 2000.

[83] M. Popovac and K. Hanjalić. Compound wall treatment for rans computation of complex turbulent flows and heat transfer. *Flow, Turbulence and Combustion*, 78:177–202, 2007.

[84] L. Prandtl. Bericht ü ber die enstehung der turbulenz. *Zeitschrift für angewandte mathematische Mechanik*, 5:136–139, 1925.

[85] O. Reynolds. On the dynamical theory of incompressible viscous fluids and the determination of the criterion. *Philosophical Transactions of the Royal Society of London*, 186:123–164, 1895.

[86] V. Rhie, C. Suzann, and L. Masbernat. Experimental investigation of a turbulent mixing layer. *International Journal of Multiphase Flow*, 24(1):35–54, 1998.

[87] J. Rotta. *Turbulente Strömungen*. BG Teubner Stuttgart, 1972.

[88] H. Rusche. *Computational Fluid Dynamics Of Dispersed Two-Phase Flows at High Phase Fractions*. PhD Thesis, Imperial College of Science, Technology and Medicine, Exhibition Road, London SW7 2BX, 2002.

[89] R. Rzehak and E. Krepper. CFD modeling of bubble-induced turbulence. *International Journal of Multiphase Flow*, 55:138–155, 2013.

[90] R. Rzehak, E. Krepper, and C. Lifante. Comparative study of wall-force models for the simulation of bubbly flows. *Nuclear Engineering and Design*, 253:41–49, 2012.

[91] Y. Sato, M. Sadatomi, and K. Sekoguchi. Momentum and heat transfer in two-phase bubble flow. *International Journal of Multiphase Flow*, 7:167–177, 1981.

[92] M. Schäfer. *Numerik im Maschinenbau*. Springer Verlag Berlin Heidelberg New-York, 1999.

[93] A. Schiller, L. und Naumann. Über die grundlegenden berechnungen bei der schwerkraftaufbereitung. *Z. Vereins deutscher Ing.*, 77(12):318–320, 1933.

[94] J. Schlüter, H. Pitsch, and P. Moin. Large eddy simulation inflow conditions for coupling with reynolds-averaged flow solvers. *AIAA Journal*, 42(3):478–484, 2004.

[95] A. Serizawa, I. Kataoka, and I. Michiyoshi. Turbulence structure of air-water bubbly flow-ii: Local properties. *International Journal of Multiphase Flow*, 2:235–246, 1975.

[96] J. A. Sethian. *Level Set Methods and Fast Marching Methods*. Cambridge University Press, 1999.

[97] C. C. Shir. A preliminary numerical study of atmospheric turbulent flows in the idealized turbulent boundary layer. *Journal of the Atmospheric Science*, 30:1327–1339, 1973.

[98] P. Spalart. Strategies for turbulence modelling and simulation. *International Journal of Heat and Fluid Flow*, 21:252–263, 2000.

[99] B. Spencer. *Statistical investigations of turbulent velocity and pressure fields in a two-dimensional mixing layer*. PhD Thesis, University of Illinois, 1970.

[100] J. H. Spurk and N. Aksel. *Fluid Mechanics*. Springer Verlag Berlin Heidelberg New-York, 2006.

[101] J. L. Tennekes, H. und Lumley. *A first course in turbulence*. The MIT Press, 1972.

[102] A. Tomiyama, I. Kataoka, T. Fukuda, and T. Sakaguchi. Drag coefficients of bubbles: 2nd report, drag coefficient for a swarm of bubbles and its applicability to transient flow. *Transactions of JSME 61*, 588:2810–2817, 1995.

[103] A. Tomiyama, I. Kataoka, and T. Sakaguchi. Drag coefficients of bubbles: 1st report, drag coefficients of a single bubble in a stagnant liquid. *Transactions of JSME 61*, 587:2357–2364, 1995.

[104] A. Tomiyama, H. Tamai, I. Zun, and S. Hosokawa. Transverse migration of single bubbles in simple shear flows. *Chemical Engineering Science*, 57:1849–1858, 2002.

[105] A. A. Troshko and Y. A. Hassan. A two-equation turbulence model of turbulent bubbly flows. *International Journal of Multiphase Flow*, 27:1965–2000, 2001.

[106] H. Versteeg and W. Malalasekera. *An Introduction to Computational Fluid Dynamics*. Pearson Education Limited, second edition, 2007.

[107] S. Wang, S. Lee, O. Jones Jr, and R. Lahey Jr. 3-d turbulence structure and phase distribution measurements in bubbly two-phase flows. *International Journal of Multiphase Flow*, 13:327–343, 1987.

[108] H. Weller. Derivation, modelling and solution of the conditionally averaged two-phase flow equations. *Technical Report TR/HGW/01, Nabla Ltd.*, 2002.

[109] D. C. Wilcox. Reassessment of the scale-determining equation for advanced turbulence models. *AIAA Journal*, 26:1299–1310, 1988.

[110] D. C. Wilcox. *Turbulence Modeling for CFD*. DCW Industries, Inc, second edition, 1994.

[111] D. C. Wilcox. Formulation of the k-ω turbulence model revisited. *AIAA Journal*, 46:2823–2838, 2008.

[112] X. Wu, J. Baltzer, and R. Adrian. Direct numerical simulation of a 30r long turbulent pipe flow at R+ = 685: large- and very large-scale motions. *Journal of Fluid Mechanics*, 698:235–281, 2012.

[113] D. Zhang. *Eulerian Modeling of reactive gas-liquid flow in a bubble column*. PhD Thesis, Universiteit Twente, 2007.

[114] D. Zhang, N. Deen, and J. Kuipers. Numerical simulation of the dynamic flow behavior in a bubble column: A study of closures for turbulence and interface forces. *Chemical Engineering Science*, 61:7593–7608, 2006.

Nomenclature

Latin letters

upper case

symbol	SI unit	description
A	–	two-componentality parameter of the Reynolds-stress anisotropy tensor
B	–	log-law constant
$C_{\varepsilon \mathrm{B}}$	–	Modeling constant in the BIT model by Rzehak and Krepper
C_{d}	–	drag force coefficient
C_{dS}	–	drag force coefficient with swarm effect
C_{l}	–	lift force coefficient
C_{vm}	–	virtual mass force coefficient
C_{td}	–	turbulent dispersion force coefficient
D	m	pipe diameter
D_1	m	pipe diameter before the expansion
D_2	m	pipe diameter after the expansion
D_{ij}^{ν}	$\mathrm{m}^2/\mathrm{s}^3$	viscous turbulent diffusion
D_{ij}^{t}	$\mathrm{m}^2/\mathrm{s}^3$	turbulent diffusion due to velocity fluctuations
D_{ij}^{p}	$\mathrm{m}^2/\mathrm{s}^3$	turbulent diffusion due to pressure fluctuations
E	–	two-componentality parameter of ε_{ij}^{h}
Eo	–	Eötvös number
F_c	m^3/s	volume flux over face c
G	–	indicator for the gas phase /
H	m	height of the water column

H_c	m	half of the channel height
$I_\psi(x_i, t)$	–	indicator function for phase ψ
I	–	turbulent intensity at the bubble column inlet
J_ψ	m/s	superficial bulk velocity of phase ψ
L_t	m	characteristic length scale of the flow / integral length scale of turbulence
L	–	indicator for the liquid phase
L_{vK}	m	von Kármán length-scale
L_{SST}	m	turbulent length-scale from the SST model
M_i^ψ	kg/m^{2}s^2	interfacial momentum transfer term
$M_{\mathrm{d},i}^\psi$	kg/m^{2}s^2	drag force component of M_i^ψ
$M_{\mathrm{l},i}^\psi$	kg/m^{2}s^2	lift force component of M_i^ψ
$M_{\mathrm{vm},i}^\psi$	kg/m^{2}s^2	virtual mass force component of M_i^ψ
$M_{\mathrm{td},i}^\psi$	kg/m^{2}s^2	turbulent dispersion force component of M_i^ψ
N_i	–	cell numbers in i direction
P	–	center of the control volume
P	kg/s^2	instantaneous pressure field
$\overline{P}$	kg/s^2	mean pressure field
$\langle\overline{P}\rangle$	kg/s^2	statistically averaged pressure field
P_{ij}	m^2/s^3	production of turbulence
P_k	m^2/s^3	production of turbulent kinetic energy
$P_{\tilde{\varepsilon},3}$	m^2/s^4	near-wall production of $\tilde{\varepsilon}$
$P_{\tilde{\omega},3}$	1/m^2	near-wall production of ω^h
$P_{kL,II}$	m^3/s^3	production in kL equation
P_{SAS}	1/s^2	scale-adaptive simulation production term in the SST-SAS model
P_{SAS}^*	1/s^2	scale-adaptive simulation production term in the IS-RSM /IIS-RSM
R	m	pipe radius
R_2	m	pipe radius after the expansion
Re	–	Reynolds number
Re_t	–	turbulent Reynolds number

Re_{B}	–	bubble Reynolds number
Re_{D}	–	bulk Reynolds number in pipe flows
$Re_{\mathrm{D_1}}$	–	bulk Reynolds number before the sudden expansion
Re_τ	–	wall-friction Reynolds number
S_V	m^2	surface of the control domain
S	$1/\mathrm{s}$	invariant of the mean strain tensor S_{ij}
S_c	m^2	surface sides of the control volume P
$\overline{S}_{ij}$	$1/\mathrm{s}$	mean rate of strain tensor
Sr	–	non dimensional shear rate
S_k	$\mathrm{m}^2/\mathrm{s}^3$	production of turbulent kinetic energy by bubble-induced turbulence model
S_ε	$\mathrm{m}^2/\mathrm{s}^4$	production of $\tilde{\varepsilon}$ by bubble-induced turbulence model
$S_{R,ij}$	$\mathrm{m}^2/\mathrm{s}^3$	production of turbulence by bubble-induced turbulence model
S_ω	$1/\mathrm{s}^2$	production of ω^h by bubble-induced turbulence model
U_i	$\mathrm{m/s}$	instantaneous velocity field
U_x	$\mathrm{m/s}$	instantaneous velocity in x-direction
U	$\mathrm{m/s}$	characteristic velocity scale
$\overline{U}_i$	$\mathrm{m/s}$	mean velocity field
$\overline{U}_i^{\psi}$	$\mathrm{m/s}$	conditional-averaged velocity field of phase ψ
$\overline{U}_i^{r}$	$\mathrm{m/s}$	mean relative velocity
$\overline{U}_i^{+}$	$\mathrm{m/s}$	statistically averaged velocity field normalized by the wall friction velocity
$\langle \overline{U}_i \rangle$	$\mathrm{m/s}$	statistically averaged velocity field
$\left\langle \overline{U}_i^{\mathrm{L}} \right\rangle$	$\mathrm{m/s}$	statistically averaged liquid velocity field
$\left\langle \overline{U}_i^{r} \right\rangle$	$\mathrm{m/s}$	statistically averaged relative velocity field
U	$\mathrm{m/s}$	characteristic velocity scale
U_c	$\mathrm{m/s}$	centerline velocity
U'	$1/\mathrm{s}$	first derivative of mean velocity field

U''	1/ms	second derivative of mean velocity field
V	m^3	size of the control domain
W	m	side length of the bubble column

lower case

symbol	SI unit	description
d_ψ	m	diameter of the phase ψ
d_h	m	hydraulic diameter
e, w, n, s	–	compass notation for the east, west, north and south face of control volume P
f	–	arbitrary source term
f_P	–	arbitrary source term in control volume P
f_μ	–	wall damping function in k-equation
$f_{\tilde{\varepsilon}}$	–	wall damping function in ε-equation
f_s	–	blending function for the dissipation rate tensor
f_ψ	–	blending function for the interfacial momentum transfer
f_i	kg/m^2s^2	volume-force density
g_i	m/s^2	gravitational vector
g	m/s^2	magnitude of the gravitational vector
i, j, k	–	control variables of the Cartesian coordinates
k	m^2/s^2	turbulent kinetic energy (of the liquid phase)
$\langle k \rangle$	m^2/s^2	statistically averaged turbulent kinetic energy
$\langle k \rangle_{\mathrm{mod}}$	m^2/s^2	statistically averaged modeled part of the turbulent kinetic energy (of the liquid phase)
$\langle k \rangle_{\mathrm{res}}$	m^2/s^2	statistically averaged resolved part of the turbulent kinetic energy (of the liquid phase)
k^ψ	m^2/s^2	turbulent kinetic energy of phase ψ
k^+	m^2/s^2	turbulent kinetic energy (of the liquid phase) normalized by the wall friction velocity
l	m	turbulent length-scale
l_k	m	Komolgorov length-scale

n_j	–	surface normal vector
p'	$\mathrm{kg/s^2}$	fluctuating pressure
r	m	radial component in cylindrical coordinates
t	s	time
u_i'	m/s	fluctuating velocity / turbulent intensity (of the liquid phase)
$\langle u_i \rangle$	m/s	statistically averaged turbulent intensity (of the liquid phase)
$\langle u_i \rangle_{\mathrm{res}}$	m/s	statistically averaged resolved part of the turbulent intensity (of the liquid phase)
$\overline{u_i' u_j'}$	$\mathrm{m^2/s^2}$	Reynolds-stress tensor (of the liquid phase)
$\overline{u_i'^{\psi} u_j'^{\psi}}^{\psi}$	$\mathrm{m^2/s^2}$	Reynolds-stress tensor for phase ψ
$\overline{u_i' u_j' u_k'}$	$\mathrm{m^3/s^3}$	turbulent triple correlation
$\langle u_i u_j \rangle$	$\mathrm{m^2/s^2}$	statistically averaged Reynolds-stress tensor (of the liquid phase)
$\langle u_i'' u_j'' \rangle$	$\mathrm{m^2/s^2}$	statistically averaged resolved part of the Reynolds-stress tensor (of the liquid phase)
$\left\langle \overline{u_i' u_j'} \right\rangle$	$\mathrm{m^2/s^2}$	statistically averaged modeled part of Reynolds-stress tensor (of the liquid phase)
u_τ	m/s	wall friction velocity
u_τ^{DNS}	m/s	wall friction velocity from direct numerical simulation
u_i^+	m/s	statistically averaged turbulent intensity (of the liquid phase) normalized by the wall friction velocity
v	m/s	turbulent velocity scale
x_i	m	Cartesian coordinates
y	m	wall distance / y coordinate
y^+	–	normalized wall distance in Cartesian coordinates
z	m	axial component in cylindrical coordinates / vertical component in Cartesian coordinates

Greek letters

upper case

symbol	SI unit	description
Γ	–	diffusion coefficient
Δt	s	time step size
Δx_i	m	size of the control volume
Δx_i^+	m	Normalized cell size
Φ	–	arbitrary quantity
$\overline{\Phi}$	–	mean part of a arbitrary quantity
$\overline{\Phi}^{\psi}$	–	conditional averaged mean part of a arbitrary quantity of phase ψ
$\langle\Phi\rangle$	–	statistically averaged arbitrary quantity
Φ_c	–	arbitrary quantity at face c
Φ_P	–	arbitrary quantity at center of the control volume
Φ_E	–	arbitrary quantity at center of the eastern control volume
Φ_e^{UDS}	–	arbitrary quantity at the eastern face estimated by UDS
Φ_e^{CDS}	–	arbitrary quantity at the eastern face estimated by CDS
Φ_{ij}	$\mathrm{m}^2/\mathrm{s}^3$	pressure redistribution

lower case

symbol	SI unit	description
α_ψ	–	phase fraction of phase ψ
$\langle\alpha_\psi\rangle$	–	statistically averaged phase fraction of phase ψ
$\alpha_{\mathrm{G}}^{\mathrm{ave}}$	–	cross sectioned averaged phase fraction of dispersed gas phase
ε	$\mathrm{m}^2/\mathrm{s}^3$	dissipation rate of the

		turbulent kinetic energy
ε_{ij}	m^2/s^3	dissipation tensor of the turbulent kinetic energy
ε^h	m^2/s^3	homogeneous part of the dissipation rate of the turbulent kinetic energy
$\varepsilon^h_{\text{wall}}$	m^2/s^3	homogeneous part of the dissipation rate of the turbulent kinetic energy at the wall
ε^h_{ij}	m^2/s^3	homogeneous dissipation tensor of the turbulent kinetic energy
$\tilde{\varepsilon}$	m^2/s^3	"quasi-homogeneous" dissipation rate of the turbulent kinetic energy
κ	–	von Karman constant
κ	$1/m$	wavenumber
γ	–	blending function between CDS and UDS
λ_e	–	interpolation factor at east face
ν	m^2/s	kinematic molecular viscosity
ν_ψ	m^2/s	kinematic molecular viscosity of phase ψ
ν_t	m^2/s	eddy-viscosity (of the liquid phase)
σ_{GL}	kg/s^2	gas-liquid surface tension
τ_{w}	N/m^2	wall-shear stress
τ_{B}	s	bubble time-scale
ρ	kg/m^3	density
ρ_ψ	kg/m^3	density of phase ψ
ϕ'	–	fluctuating part of a general variable
ϕ''	–	resolved fluctuating part of a general variable
ϕ'^ψ	–	fluctuating part of a general variable in phase ψ
φ	–	circumferential component in cylindrical coordinates
ψ	–	indicator for the respective phase. Either L for the liquid phase or G for the gas phase
ω	$1/s$	inverse turbulent timescale (of the liquid phase)
ω^h	$1/s$	homogeneous part of the inverse turbulent timescale (of the liquid phase)

ω^h_{wall}	1/s	homogeneous part of the inverse turbulent timescale (of the liquid phase) at the wall

Mathematical symbols

symbol	description
δ_{ij}	Kronecker delta
ϵ_{ijk}	epsilon tensor, (permutation symbol)

Abbreviations

symbol	description
BDF	backward differencing formula
BIT	bubble-induced turbulence
CDS	central differencing scheme
CFD	computational fluid dynamics
CFL	Courant-Friedrich-Levy
CV	control volume
DNS	direct numerical simulation
EVM	eddy-viscosity model
FVM	finite-volume method
GGDH	general gradient diffusion hypothesis
IS-RSM	instability-sensitized Reynolds-stress model
IIS-RSM	improved instability-sensitized Reynolds-stress model
LES	large eddy simulation
PISO	pressure implicit with splitting operators
RANS	Reynolds-averaged Navier-Stokes
RSM	Reynolds-stress model
SAS	scale-adaptive simulation
SGS	sub-grid-scale
SGDH	simple gradient diffusion hypothesis
SMC	second-moment closure
TFM	two-fluid model
UDS	upwind differencing scheme

URANS	unsteady Reynolds-averaged Navier-Stokes
VOF	Volume of fluid

List of Figures

List of Tables

A Jakirlić-Maduta Reynolds-stress model

I: Modeled transport equation for the Reynolds-stress tensor:

$$\begin{aligned}\frac{\partial\overline{u_i'u_j'}}{\partial t}+\overline{U}_k\frac{\partial\overline{u_i'u_j'}}{\partial x_k} &= -\left(\overline{u_i'u_k'}\frac{\partial\overline{U}_j}{\partial x_k}+\overline{u_j'u_k'}\frac{\partial\overline{U}_i}{\partial x_k}\right)+\Phi_{ij}-\varepsilon_{ij}^h \\ &\quad +\frac{\partial}{\partial x_k}\left[\left(\frac{1}{2}\nu+\frac{\nu_t}{\sigma}\right)\frac{\partial\overline{u_i'u_j'}}{\partial x_k}\right] \end{aligned} \tag{A.1}$$

Pressure redistribution Φ_{ij}:

$$\Phi_{ij}=\Phi_{ij,1}+\Phi_{ij,1}^w+\Phi_{ij,2}+\Phi_{ij,2}^w. \tag{A.2}$$

$$\Phi_{ij,1}=-C_1\varepsilon^h a_{ij}, \tag{A.3}$$

$$\Phi_{ij,2}=-C_2\left(P_{ij}-\frac{2}{3}P_k\delta_{i\,j}\right), \tag{A.4}$$

$$\Phi_{ij,1}^w=C_1^w f_w\frac{\varepsilon^h}{k}\left(\overline{u_ku_m}n_kn_m\delta_{i\,j}-\frac{3}{2}\overline{u_iu_k}n_kn_j-\frac{3}{2}\overline{u_ku_j}n_kn_i\right), \tag{A.5}$$

$$\Phi_{ij,2}^w=C_2^w f_w\left(\Phi_{km,2}n_kn_m\delta_{i\,j}-\frac{3}{2}\Phi_{ik,2}n_kn_j-\frac{3}{2}\Phi_{kj,2}n_kn_i\right) \tag{A.6}$$

with

$$C_1=C+\sqrt{A}E^2,\qquad C_2=0.8A^{1/2},\qquad C=2.5AF^{1/4}f, \tag{A.7}$$

$$f=\min\left[\left(\tfrac{Re_t}{150}\right)^{3/2};1\right],\qquad F=\min\left(0.6;A_2\right), \tag{A.8}$$

$$C_1^w=\max\left(1-0.7C;0.3\right),\qquad C_2^w=\min\left(A;0.3\right), \tag{A.9}$$

$$f_w = \min\left[\frac{k^{3/2}}{2{,}5\varepsilon^h x_n}; 1, 4\right], \qquad Re_t = k^2/(\nu\varepsilon^h), \tag{A.10}$$

$$P_{ij} = -\left(\overline{u_i'u_k'}\frac{\partial\overline{U}_j}{\partial x_k} + \overline{u_j'u_k'}\frac{\partial\overline{U}_i}{\partial x_k}\right), \qquad P_k = -\overline{u_i'u_j'}\frac{\partial\overline{U}_i}{\partial x_j}. \tag{A.11}$$

$$a_{ij} = \overline{u_i'u_j'}/k - 2/3\delta_{ij}, \qquad e_{ij} = \varepsilon_{ij}^h/\varepsilon^h - 2/3\delta_{ij}, \tag{A.12}$$

$$A = 1 - 9/8(A_2 - A_3), \qquad A_2 = a_{ij}a_{ij}, \qquad A_3 = a_{ij}a_{jk}a_{ki}, \tag{A.13}$$

$$E = 1 - 9/8(E_2 - E_3), \qquad E_2 = e_{ij}e_{ij}, \qquad E_3 = e_{ij}e_{jk}e_{ki} \tag{A.14}$$

Turbulent diffusion ν_t:

$$\nu_t = 0.144A\sqrt{k}\max\left[10\left(\frac{\nu^3}{k\omega^h}\right)^{1/4}; \frac{k^{1/2}}{\omega^h}\right]. \tag{A.15}$$

Stress dissipation rate tensor ε_{ij}^h:

$$\varepsilon_{ij}^h = \varepsilon^h\left[(1-f_s)\,\tfrac{2}{3}\delta_{ij} + \frac{\overline{u_i'u_j'}}{k}f_s\right] \quad \text{with } f_s = 1 - \sqrt{A}E^2 \tag{A.16}$$

II: Modeled scale supplying $\omega^h(=\varepsilon^h/k)$ equation:

$$\begin{aligned}\frac{\partial\omega^h}{\partial t} + \overline{U}_k\frac{\partial\omega^h}{\partial x_k} &= \frac{\partial}{\partial x_k}\left[\left(\frac{1}{2}\nu + \frac{\nu_t}{\sigma}\right)\frac{\partial\omega^h}{\partial x_k}\right] - C_{\omega,1}\frac{\omega^h}{k}P_k \\ &\quad -C_{\omega,2}\omega^h\omega^h + \frac{2}{k}\left(C_{cr,1}\frac{1}{2}\nu + C_{cr_2}\frac{\nu_t}{\sigma}\right)\frac{\partial\omega^h}{\partial x_k}\frac{\partial k}{\partial x_k} \\ &\quad +\frac{1}{k}P_{\omega,3}\end{aligned} \tag{A.17}$$

with

$$P_{\omega,3} = 2C_{\omega,3}\nu\nu_t\frac{\partial^2\overline{U}_j}{\partial x_k\partial x_n}\frac{\partial^2\overline{U}_j}{\partial x_k\partial x_n}. \tag{A.18}$$

Table A.1: Coefficients of the Jakirlić-Maduta RSM

$C_{\omega,1}$	$C_{\omega,2}$	$C_{\omega,3}$	σ	$C_{cr,1}$	$C_{cr,2}$
0.44	0.8	1.0	1.1	0.55	0.275

B Eddy-resolving Reynolds-stress model

The model equation for the Reynolds-stress tensor is the one given in Appendix A. The same accounts for the model coefficients.

I: Extended modeled scale supplying $\omega^h(=\varepsilon^h/k)$ equation:

$$\begin{aligned}\frac{\partial \omega^h}{\partial t}+\overline{U}_k\frac{\partial \omega^h}{\partial x_k} &= \frac{\partial}{\partial x_k}\left[\left(\frac{1}{2}\nu+\frac{\nu_t}{\sigma}\right)\frac{\partial \omega^h}{\partial x_k}\right]-C_{\omega,1}\frac{\omega^h}{k}P_k \\ &\quad -C_{\omega,2}\omega^h\omega^h+\frac{2}{k}\left(C_{cr,1}\frac{1}{2}\nu+C_{cr_2}\frac{\nu_t}{\sigma}\right)\frac{\partial \omega^h}{\partial x_k}\frac{\partial k}{\partial x_k} \\ &\quad +\frac{1}{k}P_{\omega,3}+P^*_{\mathrm{SAS}} \end{aligned} \tag{B.1}$$

with:

$$P^*_{\mathrm{SAS}} = C_{\mathrm{RSM},1}\max\left[2.3713\kappa S^2\left(\frac{L_{\mathrm{SST}}}{L_{\mathrm{vK}}}\right)^{\frac{1}{2}}-C_{\mathrm{RSM},2}T_2,0\right], \tag{B.2}$$

$$T_2 = 3k\max\left(\frac{1}{\omega^h\omega^h}\frac{\partial \omega^h}{\partial x_j}\frac{\partial \omega^h}{\partial x_j},\frac{1}{k^2}\frac{\partial k}{\partial x_j}\frac{\partial k}{\partial x_j}\right) \tag{B.3}$$

$$L_{\mathrm{SST}}=\sqrt{k}/(\omega^h C_\mu^{1/4}), \qquad L_{\mathrm{vK}}=\kappa U'/U'', \tag{B.4}$$

$$U'=S=\sqrt{2S_{ij}S_{ij}}, \qquad U''=\sqrt{\frac{\partial^2\overline{U}_i}{\partial x_k\partial x_k}\frac{\partial^2\overline{U}_i}{\partial x_j\partial x_j}}. \tag{B.5}$$

Table B.1: Additional coefficients the scale-resolving formulation

$C_{\mathrm{RSM},1}$	$C_{\mathrm{RSM},2}$
0.004	8

If the improved instability-sensitized RSM (IIS-RSM) formulation is utilized, the Reynolds-stress tensor is included into eq. (3.5) by:

$$\overline{u_i'u_j'}=0.8*\overline{u_i'u_j'}-0.2*\left[\nu_t\left(\frac{\partial\overline{U}_i}{\partial x_j}+\frac{\partial\overline{U}_j}{\partial x_i}\right)-\frac{2}{3}k\delta_{ij}\right] \tag{B.6}$$